



**Università degli Studi di Napoli
“Federico II”**

Dottorato di Ricerca in Fisica Fondamentale ed Applicata
XX Ciclo (2004-2007)

**Electronic and structural properties of
organic-inorganic surfaces and compounds.**

Thesis for Doctor of Philosophy degree
submitted by Ivo Borriello

Supervisors:

Prof. Domenico Ninno

Dr. Giovanni Cantele

Coordinator:

Prof. Gennaro Miele

Contents

Introduction	5
1 First-principles calculations	11
1.1 The quantum many-body problem	12
1.2 Born-Oppenheimer approximation	13
1.3 Density Functional Theory	14
1.3.1 The theorems of Hohenberg and Kohn	14
1.3.2 The Kohn-Sham equations	16
1.3.3 The exchange-correlation energy	18
1.4 Periodic systems and pseudopotentials	19
1.4.1 Plane wave pseudopotentials	20
1.5 Relaxation of the atomic positions	22
1.6 Modelling surfaces	24
2 Physics of surfaces	27
2.1 Surface atomic structure: effects of relaxation and reconstruction . . .	27
2.2 Electronic structure of metal surfaces	28
2.2.1 Jellium surfaces: Surface Dipole and Work Function	29
2.3 Electronic structure of semiconductor surfaces	31
2.3.1 Electron Affinity and Ionization Potential	31
2.3.2 Surface States	32
2.4 Surface states in the Nearly-Free Electron model	33

2.5	Surface states from a chemical point of view: dangling bonds and dimerization	36
2.6	Band Bending and Fermi Level Pinning	38
2.7	Surface functionalization	40
3	An overview of some experimental techniques	41
3.1	Low energy diffraction (LEED): structure determination	41
3.2	Scanning tunnelling microscopy	43
3.3	Kelvin probe method	47
3.4	Bulk analysis of perovskites: X-ray and adsorption measurements . .	51
3.4.1	X-ray analysis	51
3.4.2	Absorption measurements	53
3.5	Conclusions	55
4	Organic coverage of the silicon (001) surface	57
4.1	Details of the method	59
4.1.1	Electron affinity and ionization potential	61
4.1.2	Vacuum level and surface dipole	61
4.2	Results and Discussions	63
4.2.1	The isolated molecules	63
4.2.2	Silicon surfaces	64
4.2.3	Surface dipole analysis	74
4.2.4	Can we correlate EA variation to isolated molecule dipole moment?	78
4.3	Conclusions	82
5	Hybrid organic-inorganic perovskites based on tin-halides	83
5.1	Details of the method	86
5.2	Results and Discussions	87
5.2.1	Phase transitions in CsSnI ₃	88
5.2.2	Phase transitions in CsSnCl ₃	92
5.2.3	CH ₃ NH ₃ SnCl ₃ in the low-temperature phase	95
5.2.4	ASnI ₃ with A=[CH ₃ NH ₃ , NH ₂ CH=NH ₂]	96

5.3	A combined theoretical and experimental investigation of $\text{CH}_3\text{NH}_3\text{SnX}_3$ ($\text{X}=\text{Cl}, \text{Br}$) thin films	101
5.4	Conclusions	105
	Conclusions	107
	Bibliography	111

Introduction

Nanoscience is a field in continuous expansion thanks to promising interdisciplinary applications, whose functionality is not principally determined by pure material properties but by the integration of specially designed nanostructured components. The identification of new classes of materials can also profoundly affect existing products as well as enable new disrupting technologies. Recently, organic materials have received considerable attention as potential replacements for their inorganic counterparts in flat-panel-display driver circuitry and light-emitting elements. Organic materials have the key advantage of simple and low-temperature thin-film processing through inexpensive techniques such as spin coating, ink-jet printing, or stamping. The flexibility of organic chemistry enables the formation of organic molecules with useful luminescent and conducting properties. In addition to emitting light, the semiconducting properties of some organic materials enable promising technologies for organic field-effect transistors (OFETs). The ability to invent new functionalities for nanoscale systems and advanced materials, and of designing new devices for specific applications, depends heavily on our understanding of excitations under irradiation by light, electron beams or modern photon sources. Density-functional theory (DFT) is a powerful tool for ab-initio electronic structure calculations and gives valuable information about the structural arrangement of nanoscale systems. In this thesis we have performed DFT calculations for two different classes of materials, obtained by combining organic molecules with inorganic compounds.

The first class of systems which will be considered concerns silicon surface functionalization through organic molecules. The interest in the functionalization of semiconductor surfaces has grown more and more in the last years [1-5] Interfacing semiconductor systems with biological and chemical species presents many techno-

logical interests. The controlled coverage of surfaces with organic molecules is the challenging route toward the fabrication of new devices, with applications ranging from medicine and biology (sensing devices for drugs, viruses, proteins, etc.) to molecular electronics. In all these fields exciting new opportunities are offered by nanosized semiconductors, which are ideal for biological labelling due to their size-tunable light emission coupled to dimensions comparable to those of the species to be sensed [6]. One of the most investigated surfaces is the silicon (001) surface whose high chemical reactivity is well known [3, 4, 5]. Most of the peculiar characteristics of this surface are related to the formation of Si–Si dimers, as a result of the surface reconstruction. At variance with the analogous diamond surface, such silicon dimers do show geometrical buckling, which results in nonequivalent surface Si atoms, with the consequent charge transfer from the down Si atom to its upper counterpart. Such an asymmetry is responsible for the enhanced chemical reactivity of the surface. Indeed, it has been argued that the chemisorption of an organic molecule containing a C=C double bond can occur via a process known as a [2+2] cycloaddition [7-10]

The effect of organic adsorbates on the silicon (001) surface is investigated using first-principles calculations. Ethylene and a class of cyclopentene derivatives, containing different functional groups, are considered. The structural relaxation induced by the adsorption is discussed, elucidating the effect of both the adsorbate species and coverage. It turns out that different distortions occur in the molecular geometry, depending on both the species and the surface coverage, while molecule-to-surface bonding does show very similar features for all the considered molecules. We show that the presence of the adsorbate can modify the surface charge density, thus giving rise to an induced dipolar layer that modifies the electrostatic potential outside the surface. Such a dipole layer can, in turn, be related to surface electron affinity and work function changes. A careful analysis of the dipole moment and of the electrostatic potential changes is carried out discussing the correlations with the properties of the isolated molecules. All the results indicate how the surface properties can be tuned through a suitable choice of the adsorbate.

The second class of materials that we have investigated in this thesis is represented by hybrid organic-inorganic perovskites based on tin halides. Hybrid organic-inorganic composites are an emerging class of new materials that hold significant

promise. These complex structures, based on a molecular scale composite of organic and inorganic components, represent the possibility of combining properties of organic and inorganic elements in a unique composite material. The fields of application of this branch of materials are as varied as the materials themselves. Hybrid organic-inorganic compounds are considered as innovative advanced materials, and promising applications are expected in many fields, including optics, electronics, mechanics, protective coatings, catalysis, sensors, biology, and others [11-28]. For example, given the possibility of combining charge separation at an organic-inorganic interface with the high electrical mobility of an inorganic framework and the photosensitivity of an organic component, photoconductor and solar cell applications are worth considering [21-28]. Hybrid perovskite compounds based on metal-halides represent a particular class of organic-inorganic materials. Perovskite based hybrids can be synthesized with simple and cheap techniques thanks to their self-assembling character [29]. Moreover, organic-inorganic superlattices can be easily obtained by altering the combination of the organic and inorganic components in the starting solution from which the hybrids are crystallized: the electronic properties of the inorganic compound can be tuned varying of the dimensionality, realizing inorganic layers (2D systems) or multilayers, as well as inorganic chains (1D) and dots (0D) embedded in an organic matrix [18, 30, 31]. The basic building component of the organic-inorganic perovskites is the ABX_3 perovskite structure [32]. This simple structure consists of a network of corner-sharing BX_6 octahedra, where the B atom is a metal cation (typically Sn^{2+} or Pb^{2+}) and X is a monovalent anion (typically Cl^- , Br^- , I^-); the A cation is selected to neutralize the total charge, and it can be even a molecule, which must fit into a rigid and relatively small cuboctahedral hole formed by the 12 nearest X atoms. By an appropriate choice of both inorganic cage (that is the B and X elements forming the BX_6 octahedra) and cation, the structural and electronic properties can be tuned as desired [33]. In this framework, ab-initio investigations can shed light on the correlations between structure, chemical composition and properties. The ability of reproducing the structural and electronic properties and understanding their correlation with each element of the compound, offers the potential for designing new functional structures, with desired characteristics.

Our attention has been addressed to tin-halide based perovskites $ASnX_3$. Struc-

tural studies of Sn halides are interesting because of the existence of s-electron lone pair. According to a VSEPR (Valence Shell Electron Pair Repulsion) scheme, the structures of these molecules or anions are determined by the stereochemical activity of the lone pair. The structure of SnX_3^- (X =halogen) anions can be classified in four models by considering neighbors around tin atom [34]. Among these models, a regular octahedron, a square pyramid, and a trigonal pyramid were found in a series of ASnX_3 compounds. The structural diversity of SnX_3^- anions is due to the presence of two bonding schemes for the trans X-Sn-X bond, i.e. symmetric X-Sn-X and asymmetric X-Sn—X in which linearity of X-Sn-X chain is lost. This transition has a crucial role in changing of conductivity, as several experiments show: for example CsSnCl_3 showed a phase transition to a cubic perovskite phase at 379 K, at which point the electronic conductivity dramatically increased [35].

In this thesis, first-principles calculations of ASnX_3 crystals with $A=[\text{Cs}, \text{CH}_3\text{NH}_3$ (methylammonium), $\text{NH}_2\text{CH}=\text{NH}_2$ (formamidium)] and $X=[\text{Cl}, \text{Br}, \text{I}]$ are presented: the structural and electronic properties of these compounds are analyzed and related to the particular choice of the halogen X , and of the cation A embedded in the corner-sharing BX_6 octahedra network. Different phases of CsSnX_3 compounds are considered, focusing on the relation between the choice of the halogen, the structural deformations occurring in the low-temperature phase due to octahedra distortions, and the electronic properties variation due to the phase transition from high-temperature to low-temperature phases. Moreover, a comparison between hybrid and inorganic perovskites is made by changing the inorganic cation Cs with an organic molecule, evidencing the effects of the molecule to the structural and electronic properties of the compound. Finally, by varying the molecule, it is also stressed the possibility of tuning the volume of the cubic inorganic cage embedding the organic cation, with consequences in the electronic structure of the hybrid compound.

The thesis is organized as follows. In chapter 1, we present the main features of ab-initio calculations based on DFT, with an emphasis to the ability of modeling bulk structures as well as confined systems like surfaces, through an opportune setting of the periodic conditions imposed to the system. In chapter 2, we review the fundamental aspects concerning the physics of surfaces from a microscopic point of view. Structural reconstructions and surface energetics are discussed in detail.

An overview of some experimental techniques (and related results) used to study hybrid organic-inorganic interfaces and compounds are described in some detail in chapter 3. In chapter 4, ab-initio calculations of the silicon (001) surface functionalization through organic molecules are presented, focusing on the electron affinity variation induced by the adsorbate organic layers. In chapter 5, the attention is addressed to the hybrid perovskite compounds of the type $ASnX_3$ and the theoretical investigation, using ab-initio methods, of the electronic and optical properties of perovskite tin-halides is described. Finally, we make conclusive remarks and indicate the possible developments in the conclusive section.

Chapter 1

First-principles calculations

In this chapter we illustrate the theoretical framework for the study of the electronic and structural properties of the systems considered in this thesis. The properties of matter is governed by the behavior of almost massless electrons which move around much heavier nuclei. If we want a theoretical model describing matter we thus need to solve a system dealing with the interactions of a very large number of particles. It is evident that in order for us to manage to describe a real system some approximations and simplifications have to be made. The Born-Oppenheimer approximation allows to decouple the ionic and electronic degrees of freedom, thanks to their large mass difference; in doing so, one solves the Schrödinger equation for the electronic ground state by considering the nuclei as fixed, thus obtaining the total energy of the system $E[\mathbf{R}]$ as a function of ionic positions, which appear as parameters. $E[\mathbf{R}]$ plays the role of an effective potential for the nuclei motion. It is still not possible, however, to tackle the full many-body electronic problem directly (at least for the systems we wish to investigate), and actually it would be impossible even to store in the computer's memory the electrons many-body wavefunction. Nevertheless, it is possible to recast the intractable interacting problem in a more manageable self-consistent independent-electron one, much in the same way as in a Hartree calculation [36]. The theoretical basis for this approach, known as Density Functional Theory (DFT), has been given by Hohenberg and Kohn in the 60's [37, 38], and it is widely used in modern computational material science. According to the Hohenberg and Kohn theorem, the ground state density of a bound system

of interacting electrons in an external potential uniquely determines the potential. Therefore, all ground state information on the system is in principle inherent in the electronic density. This insight can be used to construct a method for self-consistently determining the ground state electron density and energy with much less computational cost than that involved in solving the corresponding Schrödinger equation. Knowing the exact form of the exchange-correlation of the system, the procedure would be exact; different attempts at establishing a functional form of the exchange-correlation have been done.

Other approximations are necessary to use the computational scheme in practice. In describing periodic systems, it is advantageous to use Bloch's theorem and expand the wave function in plane waves, including only the lower energy ones in the calculation. Additionally, as the valence electrons strongly dominate electrical bonding, pseudopotentials are introduced to reduce the computational task. In the following we illustrate the general DFT framework, as well as the plane-wave pseudopotential technique.

1.1 The quantum many-body problem

Most physical problems of interest consist of a number of interacting electrons and ions. For a system composed of k electrons and m positively charged nuclei (ions) we can write its many-particle nonrelativistic Hamiltonian as follows:

$$\hat{H} = \hat{T}(\mathbf{r}) + \hat{T}_n(\mathbf{R}) + \hat{V}_{e-e}(\mathbf{r}) + \hat{V}_{e-n}(\mathbf{r}, \mathbf{R}) + \hat{V}_{n-n}(\mathbf{R}) \quad (1.1)$$

where $\hat{T}(\mathbf{r})$ and $\hat{T}_n(\mathbf{R})$ are the kinetic energy operators for the electrons and the nuclei respectively, while the last three terms describe the *electron–nucleus*, the *electron–electron*, and the *nucleus–nucleus* Coulomb interaction.

The many-particle wavefunction of the system Ψ depends on both electronic coordinates $\mathbf{r} = \{r_1, r_2, \dots, r_k\}$ and nuclear coordinates $\mathbf{R} = \{R_1, R_2, \dots, R_m\}$ ¹:

$$\Psi = \Psi(\mathbf{r}, \mathbf{R}) = \Psi(r_1, r_2, \dots, r_k, R_1, R_2, \dots, R_m) \quad (1.2)$$

¹For the sake of simplicity we neglect the vector notation (e.g. r instead of \vec{r}) for the 3-dimensional position vector of both electrons and nuclei.

1.2 Born-Oppenheimer approximation

The Born-Oppenheimer approximation is one of the most important approximations in materials science. It is used in the vast majority of methods. The essence of the approximation is that the nuclei, being so much heavier than electrons, move relatively slowly, and may be treated as stationary while the electrons move relatively to them. Hence, the nuclei can be thought as being fixed, which makes it possible to solve the Schrödinger equation for the wavefunction of electrons alone. However, the electron energy depends on the nuclear positions (electrons adiabatically follow the nuclei):

$$\Psi(\mathbf{r}, \mathbf{R}) \approx \chi(\mathbf{R}) \cdot \psi_{\mathbf{R}}(\mathbf{r}) \quad (1.3)$$

where $\psi_{\mathbf{R}}$ is the electronic wavefunction for the configuration \mathbf{R} of the nuclei.

Thus, the Schrödinger equation for the electrons reads

$$\hat{H}_e \psi_{\mathbf{R}} = \left[\hat{T}(\mathbf{r}) + \hat{V}_{e-e}(\mathbf{r}) + \hat{V}_{e-n}(\mathbf{r}, \mathbf{R}) \right] \psi_{\mathbf{R}} = E_e(\mathbf{R}) \psi_{\mathbf{R}} \quad (1.4)$$

If $E_e(\mathbf{R})$ is known for a nuclear configuration \mathbf{R} , the corresponding potential energy of the nuclei is given by:

$$\Phi^{BO}(\mathbf{R}) = V_{n-n}(\mathbf{R}) + E_e(\mathbf{R}) = \sum_{\alpha \neq \beta} \frac{Z_\alpha Z_\beta}{|R_\alpha - R_\beta|} + E_e(\mathbf{R}) \quad (1.5)$$

where $\Phi^{BO}(\mathbf{R})$ is defined as the Born-Oppenheimer potential surface and Z_α is the charge of the nucleus at R_α .

In the electronic Hamiltonian \hat{H}_e only the electrons are kept as players in the many-body problem. The nuclei are deprived from this status, and reduced to a given source of positive charge, becoming “external” to the electron cloud. After having applied this approximation, we are left with a collection of k interacting negative particles, moving in the (now external or given) potential of the nuclei. Formally we write this as follows:

$$\hat{H}_e = \hat{T} + \hat{V}_{e-e} + \hat{V}_{ext} \quad (1.6)$$

It is interesting to note here that, at a fixed number of electrons, the kinetic and electron-electron terms are independent of the particular kind of many-electron system. System-specific information (which nuclei, and at which positions) is given entirely by \hat{V}_{ext} .

1.3 Density Functional Theory

The quantum many body problem obtained after the first level approximation (Born-Oppenheimer) is much simpler than the original one, but still far too difficult to solve. Several methods exist to reduce the problem to an approximate but tractable form. A historically very important one is the Hartree-Fock method (HF), described in many condensed matter textbooks. It performs very well for atoms and molecules, and is therefore used a lot in quantum chemistry. For solids it is less accurate, though. We will not treat HF, but explain a more modern and probably also more powerful method: Density Functional Theory (DFT). Although its history goes back to the early 30's of the 20th century, DFT has been formally established in 1964 by two theorems due to Hohenberg and Kohn [38].

1.3.1 The theorems of Hohenberg and Kohn

The traditional formulation of the two theorems of Hohenberg and Kohn (HK)[38] is as follows:

First theorem of Hohenberg and Kohn

There is a one-to-one correspondence between the ground-state density² $\rho(r)$ of a many-electron system (atom, molecule, solid) and the external potential V_{ext} . An immediate consequence is that the ground-state expectation value of any observable \hat{O} is a unique functional of the exact ground-state electron density:

$$\langle \psi | \hat{O} | \psi \rangle = O[\rho] \tag{1.7}$$

²The density $\rho(r)$ is obtained as the expectation value of the density operator $\hat{\rho}$, defined as $\hat{\rho} = \sum_{i=1}^k \delta(r_i - r)$. In this way, the ground-state density $\rho(r)$ becomes $\rho(r) = \langle \psi | \hat{\rho} | \psi \rangle = \sum_{i=1}^k \int \psi^*(r_1, r_2, \dots, r_i \equiv r, \dots, r_k) \psi(r_1, r_2, \dots, r_i \equiv r, \dots, r_k) dr_1 dr_2 \dots \cancel{dr_i} \dots dr_k$

Second theorem of Hohenberg and Kohn

For \hat{O} being the Hamiltonian \hat{H}_e , the ground-state total energy functional $H_e[\rho] \equiv E_{V_{ext}}[\rho]$ is of the form:

$$E_{V_{ext}}[\rho] = \langle \Psi | \hat{T} + \hat{V}_{e-e} | \Psi \rangle + \langle \Psi | \hat{V}_{ext} | \Psi \rangle = F[\rho] + \int \rho(r) V_{ext}(r) dr \quad (1.8)$$

where the Hohenberg-Kohn density functional $F[\rho]$ is universal for any many-electron system. $E_{V_{ext}}$ reaches its minimal value (equal to the ground-state total energy) for the ground-state density corresponding to V_{ext} .

We do not prove these theorems here, but consider a few implications of the three keywords **invertibility** (one-to-one correspondence $\rho \leftrightarrow V_{ext}$), **universality** and **variational access** (minimal value).

First, the one-to-one correspondence between ground-state density and external potential is intriguing. It is obvious that a given many-electron system has a unique external potential, yielding a unique ground-state many particle wavefunction. From this wavefunction, the corresponding electron density is easily found. Hence, an external potential leads to a unique ground-state density corresponding to it. Intuitively, it looks like the density contains less information than the wavefunction. If this were the case, it would not be possible to find a unique external potential if only the ground-state density is given. The first theorem of HK tells exactly that this is indeed possible! The density contains, in the ground-state, as much information as the wavefunction does (i.e. everything you could possibly know about an atom, molecule or solid). All observable quantities can be retrieved therefore in a unique way from the density only, i.e. they can be written as functionals of the density.

Second, the universality of $F[\rho]$. The contribution to the total energy from the external potential can be exactly calculated. On the other hand, an explicit expression for the HK functional $F[\rho]$ is unknown. Nonetheless, because it does not contain information on the nuclei and their position, it is a universal functional for any many-electron system. This means that in principle an expression for $F[\rho]$ exists which can be used for every atom, molecule or solid.

Third, the second theorem makes it possible to use the Rayleigh-Ritz variational principle to find the ground-state density. Out of the infinite number of possible

densities, the one which minimizes $E_{v_{ext}}[\rho]$ is the ground-state density corresponding to the external potential V_{ext} . Of course, this can be done only if (an approximation to) $F[\rho]$ is known. But having found ρ , all knowledge about the system is within reach.

1.3.2 The Kohn-Sham equations

The HK theorems allow to recast the many-electron problem into a variational problem, with the total energy functional depends only by the density ρ . Despite we are left with a function of only three variables, finding the minimum of $E[\rho]$ can be hard. In order to transform DFT in a practical tool, Kohn and Sham [37] reformulated the variational problem into a form much easier to handle. The energy functional can be written as the sum of three components (for the sake of simplicity, from now on we neglect the subscript of $E_{v_{ext}}$):

$$E[\rho] = T_0[\rho] + V[\rho] + E_{xc}[\rho] \quad (1.9)$$

The first term is the kinetic energy of electrons in a system which has the same density $\rho(r)$ as the real system but in which the electrons are assumed to be *non-interacting* with the electron-electron interactions turned off. The second term comprises the sum of the usual Hartree Coulomb energy and the electrostatic interaction energy between the electrons and the external potential due to the nuclei i.e.

$$V[\rho] = \int [v_H(r) + v_{ext}(r)] \rho(r) dr \quad (1.10)$$

with

$$v_H(r) = \int \frac{\rho(r')}{|r - r'|} dr' \quad ; \quad v_{ext}(r) = - \sum_{\alpha=1}^m \frac{Z_\alpha}{|r - R_\alpha|} \quad (1.11)$$

where Z_α is the positive charge of the nucleus in R_α . The third term is the so-called exchange-correlation energy functional, that comprises all the terms that remain to make the functional Eq. (1.9) exact.

The kinetic energy functional of the fictitious non-interacting system may be expressed as:

$$T_0[\rho] = \sum_i \left[-\frac{1}{2} \int \psi_i^*(r) \nabla^2 \psi_i(r) dr \right] \quad (1.12)$$

where $\psi_i(r)$ is an orthonormal set of single-particle wavefunctions such that

$$\rho(r) = \sum_i |\psi_i(r)|^2 \quad (1.13)$$

The sum is extended over all the occupied states. The ground state energy is found by minimizing the energy $E[\rho]$ of Eq. (1.9) with respect to all the possible variations of the electron density $\rho(r)$ under the constraint that the number of particles is conserved. Using variational calculus it may be shown [37] that the ground state energy can be written in the form

$$E[\rho] = \sum_i \epsilon_i - \frac{1}{2} \int \frac{\rho(r)\rho(r')}{|r-r'|} dr dr' - \int v_{xc}(r)\rho(r)dr + E_{xc}[\rho] \quad (1.14)$$

where

$$v_{xc} = \frac{\delta E_{xc}[\rho(r)]}{\delta \rho(r)} \quad (1.15)$$

is the functional derivative of the exchange-correlation energy functional $E_{xc}[\rho]$. The single-particle occupied energy levels ϵ_i that enter the sum in the first term of Eq. (1.14) are the eigenvalues resulting from solving a Schrödinger -like equation for non-interacting particles:

$$\left[-\frac{1}{2} \nabla^2 + v_{eff}(r) \right] \psi_i(r) = \epsilon_i \psi_i(r) \quad (1.16)$$

with

$$v_{eff}(r) = v_H(r) + v_{ext}(r) + v_{xc}(r) \quad (1.17)$$

Therefore, Kohn and Sham provided a recipe for solving the ground state energy of a many-body electron system within an effective one-electron framework provided the form of the exchange-correlation functional that enters both the Schrödinger equation (1.16) and the total energy (1.14) be known.

1.3.3 The exchange-correlation energy

The above described Kohn-Sham scheme is exact: apart from the preceding Born-Oppenheimer approximation, no other approximations were made. But we neglected so far the fact that we do not know the exact form of the exchange-correlation functional. It is here that approximations enter DFT theory.

The exchange-correlation potential v_{xc} is a functional derivative of the exchange correlation functional, with respect to the density. For a homogeneous electron gas, this will depend on the value of the electron density. For a non-homogeneous system, the value of the exchange correlation potential at the point r depends not only on the value of the density at r but also on its variation close to r , and it can therefore be written as an expansion over the gradients to arbitrary order of the density. Apart from the fact that the exact form of the energy functional is unknown, inclusion of density gradients makes the solution of the DFT equations rather difficult. The simplest way to obtain this contribution is to assume that the exchange correlation energy leads to a local exchange correlation potential depending only on the value of the density at r , with no density gradient contribution. This is the local density approximation (LDA):

$$E_{xc}^{LDA} = \int \rho(r) \varepsilon_{xc}(\rho(r)) dr \quad (1.18)$$

The term $\varepsilon_{xc}(\rho(r))$ is now a function and not a functional of the density ρ and for the homogeneous electron gas it is numerically known. This postulate is somehow reasonable: it means that the exchange-correlation energy due to a particular density $\rho(r)$ could be found by dividing the material in infinitesimally small volumes with a constant density. Every volume contributes to the total exchange correlation energy by an amount equal to the exchange correlation energy of an identical volume filled with a homogeneous electron gas, that has the same overall density as the original material in that volume. Nothing guarantees that the true E_{xc} is of this form, it is only a reasonable guess. By construction, LDA is expected to perform well for systems with a slowly varying density. But rather surprisingly, it appears to be very accurate in many other (realistic) cases too. A next logical step to improve on LDA, is to make the exchange-correlation contribution of every infinitesimal volume not only dependent on the local density in that volume, but also on the

density in the neighbouring volumes. In other words, the gradient of the density will play a role. This approximation is therefore called the Generalized Gradient Approximation (GGA). The basic idea of GGA is to express the exchange-correlation energy in the following form:

$$E_{xc}^{GGA} = \int \rho(r) \varepsilon_{xc}(\rho(r)) dr + \int f_{xc}(\rho(r), |\nabla\rho(r)|) \rho(r) dr \quad (1.19)$$

where f_{xc} is a function depending on two independent variables $\rho(r)$ and $|\nabla\rho(r)|$. It is of interest to note that there is only one LDA exchange-correlation functional, because there is a unique definition for ε_{xc} , but there is some freedom to incorporate the density gradient, and therefore several versions of GGA exist. A great number of them have appeared, but the most popular are those of Perdew, Burke, and Ernzerhof (PBE) [39] and Perdew and Wang (PW91) [40]. GGAs do not offer a consistent improvement over LDA in all types of system, but they have been shown to improve on the LDA for calculations of the atomic energies and binding energies (in particular, they yield a good description of the hydrogen bond), at a modest additional computational effort.

1.4 Periodic systems and pseudopotentials

When the system to be simulated has translational symmetry (a perfect crystal, for instance), the most natural choice is to work with a periodically repeated cell, with periodic boundary conditions. In this case the Kohn-Sham (KS) equations (1.16) are translationally invariant, due to the periodicity of the external potential $v_{ext}(r)$. Thus, using Bloch theorem [36], the KS wavefunctions have the form:

$$\psi_i(r) = \psi_{nk}(r) = e^{ik \cdot r} u_{nk}(r) \quad (1.20)$$

where $u_{nk}(r)$ is a function with the same periodicity as the external potential v_{ext} . The KS wavefunctions are labeled by the band index n and a vector k in the first Brillouin zone. As a consequence, the computation of the electronic density and then of the energy requires an integral over the Brillouin zone.

$$\rho(r) = \sum_{n,k} |\psi_{nk}|^2 \quad (1.21)$$

In principle, an infinite number of points should be included in the summation. In practice, a finite set of k -points is used.

1.4.1 Plane wave pseudopotentials

To solve numerically the KS equations it is necessary to expand the wavefunctions in a basis set, and one of the most common choices in ab-initio calculations is that of Plane-Waves (PWs):

$$\psi_{nk} = \sum_G e^{i(k+G)\cdot r} c_n(k+G) \quad (1.22)$$

so that KS equations in reciprocal space read:

$$\begin{aligned} \sum_{G'} \left[\frac{1}{2}|k+G|^2 \delta_{G,G'} + v_H(G-G') + v_{xc}(G-G') + v_{ext}(G-G') \right] c_n(k+G') \\ = \epsilon_{nk} c_n(k+G) \end{aligned} \quad (1.23)$$

where G and G' are reciprocal lattice vectors and the potentials have been Fourier-transformed³. The accuracy of the calculation is set by fixing the kinetic energy cutoff for the truncation of the basis:

$$\frac{1}{2}|k+G|^2 < E_{cut} \quad (1.24)$$

The equations (1.23) are then solved self-consistently with the potential, and represent the most time-consuming part of the calculation. The main advantages of the PW set are its translational invariance, the existence of one simple parameter to specify the accuracy and, very importantly, the availability of Fast Fourier Transform algorithms to speed up calculations. Moreover, the PW basis is not biased

³A local operator $O(r)$, periodic on the lattice ($O(r) = \sum_G b_G e^{iGr}$), in the PWs basis set writes as follows: $\langle k+G'|O(r)|k+G''\rangle = \sum_G b_G \int e^{-i(k+G')r} e^{iGr} e^{i(k+G'')r} dr \equiv O(G'-G'')$

by atomic positions and Poisson equation is trivially solved, since in this basis the Laplacian operator is diagonal:

$$v_H \propto \frac{\rho(G)}{G^2} \quad (1.25)$$

On the other hand, this basis puts the same resolution in every region of space so that it is impossible to describe, with a manageable number of PWs, the oscillations of core electrons. One possible solution for this problem is the **pseudopotentials technique**, a well established tool, which has an accuracy comparable to other, computationally more demanding methods. The idea behind pseudopotentials is to replace the generic Coulomb potential $-Z/|r-R|$ felt by all the electrons by a more complicated operator which takes into account not only the potential of the nucleus, but also the screening and repulsion by the core electrons. In this way, **the core electrons are eliminated from the problem** (the *frozen core* approximation), and we are left with an effective potential for the valence electrons. A reference calculation is carried out for the isolated atom with all of its electrons, and then an analytical pseudopotential is fitted in order to reproduce the same spectrum and wavefunctions as in the all-electron calculation. The valence electrons must be constrained to be orthogonal to the core electrons. In the all-electron case this means the valence wavefunctions have a large number of nodes near the nucleus. One of the reasons we are pseudizing is to make the wavefunction variations smoother, so these must be eliminated. A cut-off radius is chosen, and the pseudopotential bound states must reproduce the valence wavefunctions outside this radius, and be smooth inside. This approach makes it possible to perform the calculation with a manageable energy cutoff for the PW basis set. The price to be paid to achieve this goal is the use of non-local potentials \hat{v}^{ps} , different for each angular momentum l :

$$\hat{v}^{ps} = \sum_l |l\rangle v_l(r^2) \langle l| \quad (1.26)$$

where $|l\rangle$ is angular momentum projector operator. It can be shown [41] that the non-local term in the PWs basis assumes the form $v^{ps}(k+G, k+G')$ and Eq. 1.23 is replaced by

$$\sum_{G'} \left[\frac{1}{2} |k + G|^2 \delta_{G,G'} + v_H(G - G') + v_{xc}(G - G') + v^{ps}(k + G, k + G') \right] c_n(k + G')$$

$$= \epsilon_{nk} c_n(k + G) \quad (1.27)$$

In this thesis, two types of pseudopotential methods are used, namely **norm conserving** and **ultrasoft**. Norm-conserving pseudopotentials are constructed subject to a constraint which is intuitive and natural : the charge contained inside the cut-off radius for the pseudo and all-electron wavefunctions must be the same (beyond the cut-off the wavefunctions should be identical). This is known as norm-conservation. In 1990 Vanderbilt [42] introduced a formalism (ultrasoft pseudopotentials (USPP) method) which relaxes this condition. The additional degrees of freedom gained from relaxing the norm-conserving condition can be used to make much smoother pseudopotentials, requiring a smaller plane-wave basis set with no practical loss of accuracy.

1.5 Relaxation of the atomic positions

Within the Born-Oppenheimer approximation the nuclei move on a potential energy surface (PES) $\Phi^{BO}(\mathbf{R})$ defined in Eq. (1.5). The ground-state atomic geometry of a system is found by minimizing the forces acting on each atom or, in other words, finding the minimum of the PES. Starting from a self-consistent charge density for the given atomic positions, the total energy is obtained, as well as the force acting on each atom as the energy gradient with respect to the atomic positions. The determination of the forces makes use of the Hellmann-Feynman theorem [43, 44]:

Theorem of Hellman-Feynman *Let η be a parameter in the Hamiltonian \hat{H} , Ψ_η an eigenfunction of \hat{H} of energy E . Then,*

$$\frac{\partial E}{\partial \eta} = \left\langle \Psi_\eta \left| \frac{\partial \hat{H}}{\partial \eta} \right| \Psi_\eta \right\rangle \quad (1.28)$$

Using this algorithm to find the ground-state atomic geometry is known as **relaxing** the system. Practically, different techniques exist, based on the Hellman-

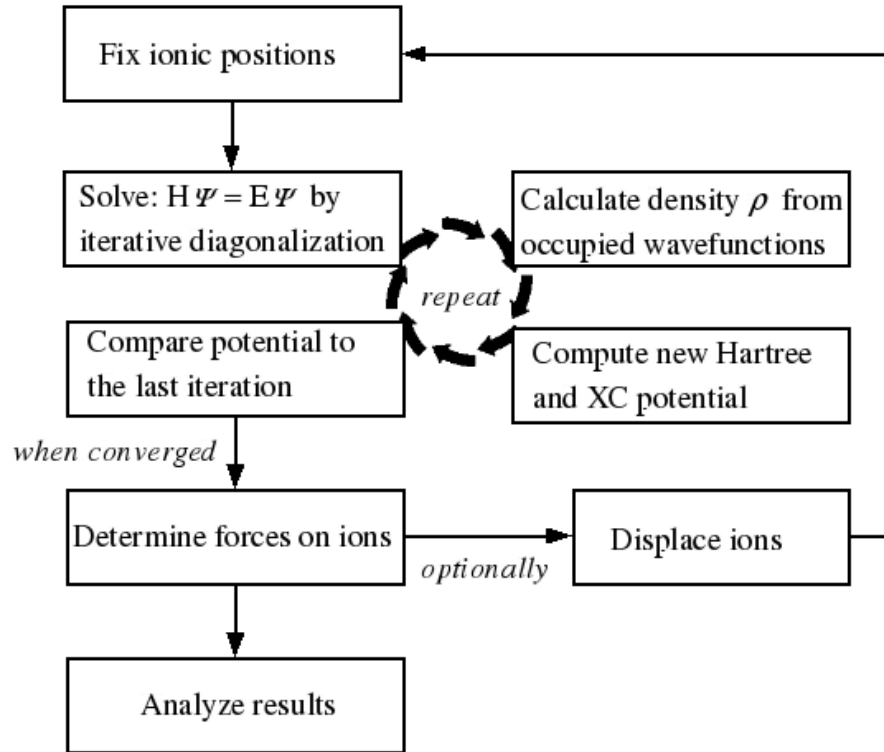


Figure 1.1: Self-consistent calculation flow chart. The potential of the crystal, including the Hartree and the exchange-correlation terms, is self-consistently iterated. When convergence is reached, forces acting on atoms are computed and, if requested, atoms are moved. In this case the calculation ends when the total force is less than the required threshold.

Feynman theorem, to find the energy minimum with respect to the atomic positions: in this thesis the Broyden-Fletcher-Goldfarb-Shanno (BFGS) method [45] was selected. To summarize, in Fig. 1.1, the flow chart of the self-consistent calculation is presented. Starting from the given atomic position in the unit cell and a charge density obtained by a superposition of atomic orbitals, the system is solved self-consistently, since the effective potential is a functional of the density. The convergence is reached when the charge density of the last iteration differs from the previous one less than the convergence threshold. Then the forces acting on atoms are obtained and, if the relaxation is requested, the atoms are moved, giving rise to

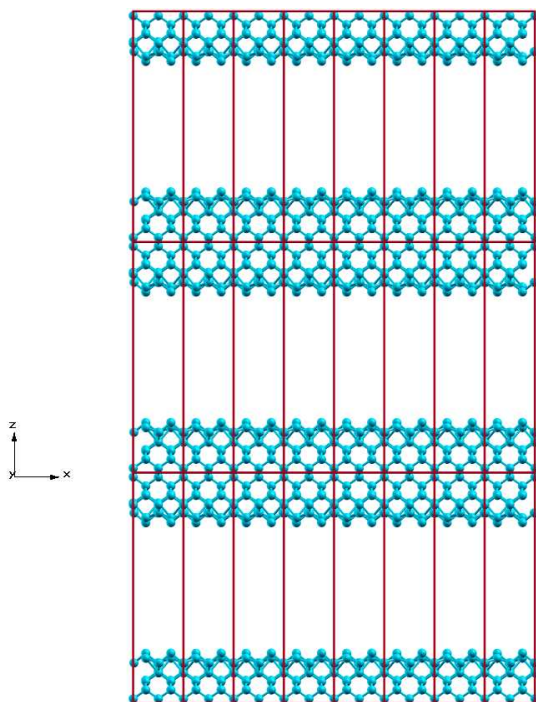


Figure 1.2: Picture of the supercell approach to model surfaces: the surface is represented by a periodic sequence of slabs separated by vacuum.

new input coordinates. In this case, the calculation ends when the total force acting on atoms is less than the required threshold.

1.6 Modelling surfaces

A finite block of crystal contains a very great number of atoms. Fortunately, crystalline solids have, by definition, periodicity, which allows important simplifications of the problem. Bloch's theorem can be applied, allowing the electronic structure problem for infinite solids to be tackled in 3D periodic simulation cells (or supercells). Surfaces, although only periodic in two dimensions, can be computed within 3D supercells by introducing a vacuum region into the unit cell. In particular, the introduction of a vacuum region along just one dimension, for example along the z axis as shown in Fig. 1.6, divides the unit cell into filled regions (slab) and vacuum.

The periodic boundary conditions ensure that the slab is infinite along the x and y directions, while along the z direction the slab and vacuum alternate infinitely. Both the slab and the vacuum regions must be thick enough to ensure that: i) the internal layers display a bulk solid behaviour; ii) no interaction is set up between surfaces either belonging to the same slab or of different slabs, facing each other.

Chapter 2

Physics of surfaces

In this chapter the main features concerning the physics of surfaces are presented from a microscopic point of view. In particular, semiconductor surfaces are described in detail. The theoretical concepts and the experimental tools (not described in this thesis) developed in the field of surface physics are the basis of the modern interface physics. Surface physics itself represents an important branch of microscopic solid state physics and physical chemistry, in particular looking at surface reactions. Moreover, surface functionalization through organic molecules represents an intriguing opportunity for the development of *micro*- and *nano*-electronics.

2.1 Surface atomic structure: effects of relaxation and reconstruction

The simplest picture of a microscopic surface structure is that of the truncated bulk (ideal surface). The most severe problem with the truncated bulk model is that it completely neglects the dramatic change in the coordination and potential due to the abrupt termination of the crystal in the direction normal to the surface. This change will for almost all surfaces lead to a new atomic configuration near the surface itself, that can be splitted into two different phenomena, typically called **relaxation** and **reconstruction**. A relaxation is a change in the distances between the first few layers with respect to the bulk values. A more severe change of structure is the

phenomenon of surface reconstruction. In a reconstruction, the periodicity parallel to the surface is changed with respect to that of the bulk. Surface reconstructions are the rule in the case of semiconductors, where the bonds are highly directional. Cleaving the crystal leaves the structure in a unfavourable state characterized by half-occupied “dangling” bonds. Reconstructions give a considerable gain in energy and reduce the number of dangling bonds. The resulting structures can be rather complicated. The phenomenon of reconstruction makes it necessary to have a nomenclature which describes the periodicity and symmetry of the surface with respect to that of the bulk. Suppose the two-dimensional lattice vectors of the bulk are \vec{a}_1 and \vec{a}_2 . By “two-dimensional lattice vectors of the bulk” we mean the lattice vectors for the bulk-truncated crystal or, equivalently, the vectors which represent the lattice of the bulk projected onto the surface. Let the lattice vectors of the surface (even including adsorbate overlayers) be \vec{b}_1 and \vec{b}_2 . A simple nomenclature of surface structures is that of Wood [46]. The surface structure is described by

$$N \left(\frac{b_1}{a_1} \times \frac{b_2}{a_2} \right) R\Theta \quad (2.1)$$

where $N = \text{“p”}$ or “c” for primitive or centred cells, respectively, and Θ is the angle by which the surface vectors have to be rotated with respect to those of the bulk (see Fig. 2.1). Often the index “p” is omitted as well as the index Θ when no rotation occurs ($\Theta = 0$).

2.2 Electronic structure of metal surfaces

The electronic structure at the surface differs from that in the bulk. The loss of the translational symmetry along the surface normal has important and interesting consequences for the electronic structure. Some of the most important understanding of surface electronic structures comes from the early studies of Lang and Kohn on metal surfaces [47, 48]. Their studies, based on the jellium model of a metal surface, prove a useful way to introduce important concepts such as the **surface dipole** and the **work function**.

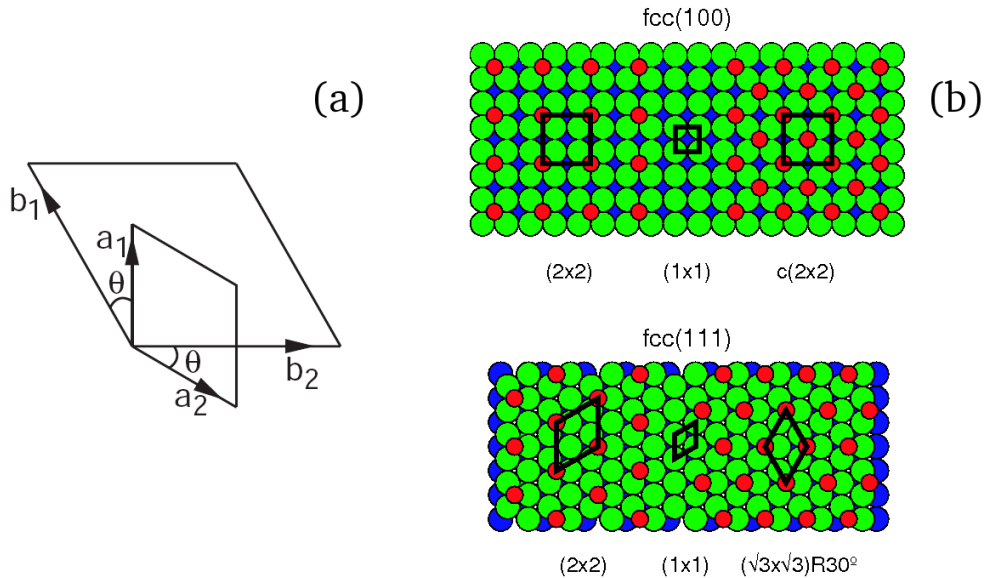


Figure 2.1: The Wood's terminology for surface lattices (a) and some examples for structures described by the Wood's nomenclature (b).

2.2.1 Jellium surfaces: Surface Dipole and Work Function

A simple model of a metal consists on a description of the electron density $n(r)$, in the presence of a uniform density n_+ of metal ions. This is the so called jellium model, where the positive charge is smeared out uniformly. The famous plot of Lang and Kohn [48], shown in Fig. 2.2a, clearly shows the intuitive passage from a bulk (infinite crystal) to a surface jellium model. The positive background (n_+) is terminated abruptly along a plane at $x = 0$, with the positive background filling the half-space $x \leq 0$, with the form:

$$\begin{cases} n_+(x) = \bar{n} & x \leq 0 \\ n_+(x) = 0 & x > 0 \end{cases}$$

where \bar{n} is the mean density of the positive charge in the ionic lattice.

As shown in Fig. 2.2a, the electron density $n(x)$ spills into the vacuum. The spread of electrons beyond the edge of the positive background causes the appearance of a dipole layer, with the dipole moment directed into the bulk, rendering the elec-

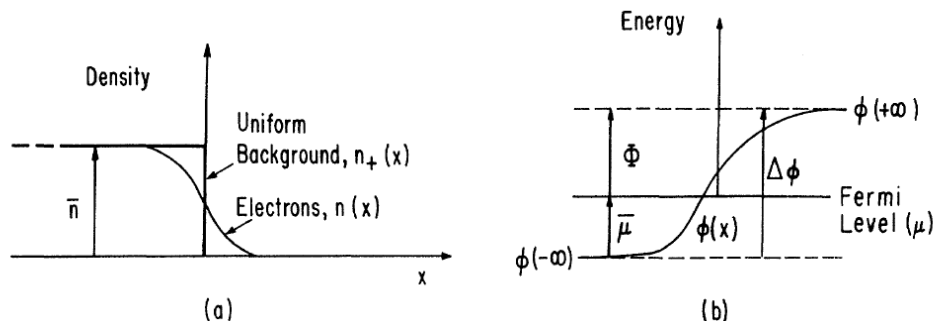


Figure 2.2: Schematic representation of (a) density distributions at a metal surface and (b) various energies relevant to a study of the work function.

electrostatic potential in the vacuum ($\phi(+\infty)$) higher than that in the bulk ($\phi(-\infty)$). Thus, an electron trying to leave the metal, encounters a surface dipole layer, with an electrostatic potential energy difference $\Delta\phi = \phi(+\infty) - \phi(-\infty)$, directly proportional to the surface dipole layer p as it can easily be derived from the Poisson's equation. In gaussian units it can be written as follows:

$$\Delta\phi = \phi(+\infty) - \phi(-\infty) = -4\pi \int_{-\infty}^{+\infty} x[n(x) - n_+(x)]dx = -4\pi p \quad (2.2)$$

It is now easy to relate the surface dipole layer with the work function. The definition of **work function** is based on a hypothetical experiment in which an electron is removed from inside the bulk crystal and transferred through the surface to a region outside. In this definition the work function is the energy difference between two states of the whole crystal. As in a photoemission experiment, the initial state is the neutral crystal containing N electrons with an energy E_N . In the final state, one electron is removed, with a gain in electrostatic energy equal to $\Delta\phi$, and the crystal remains with $N - 1$ electrons at an energy E_{N-1} . The resulting work function is $\Phi = [E_{N-1} + \Delta\phi] - E_N$. In a rigorous expression of work function, the difference $E_N - E_{N-1}$ has to be replaced by derivative of the energy with respect to the number of electrons ($\partial E/\partial N$), that is the chemical potential μ (whose value at zero temperature is equal to the Fermi Level).

The work function Φ can then be expressed as follows:

$$\Phi = \Delta\phi - \bar{\mu} \quad (2.3)$$

where $\bar{\mu}$ is the chemical potential of the electrons in the bulk metal relative to the mean electrostatic potential there (as clearly shown in Fig. 2.2)

A picture of the work function Φ at the jellium surface is shown in Fig. 2.2b. The electrostatic potential gets to a constant value in the vacuum, which represents the electrostatic energy of the electron removed from the bulk. This energy level is often called **vacuum energy level** (VL).

2.3 Electronic structure of semiconductor surfaces

As previously seen for metal surfaces, the loss of the translational symmetry along the surface normal causes the formation of a dipole layer at the surface, so that an electron trying to leave the crystal encounters an electrostatic energy difference directly proportional to that dipole layer. In semiconductors, the existence of a forbidden energy region between occupied valence bands and empty conduction bands has to be taken into account, giving rise to interesting features of surface physics.

2.3.1 Electron Affinity and Ionization Potential

At the surface of a semiconductor crystal, the energy bands of the solid get related to the vacuum energy level (VL), that is the constant value of the electrostatic potential in the vacuum far from the surface. It takes a finite amount of energy to remove electrons from the crystal to the vacuum. We have already seen that the **work function** is the energy to transfer one electron at the chemical potential from the crystal into the vacuum. On the other hand, in pure semiconductors there are no states at the chemical potential, which lies in the forbidden energy region between the respectively filled and empty valence and conduction bands. Hence, in the case of semiconductor, it is necessary to introduce the **ionization potential**, which is the energy necessary to transfer an electron from the top of the valence band E_{VBM} to the vacuum level energy VL. Similarly, the **electron affinity** is introduced as the

energy difference between the vacuum energy level and the bottom of the conduction band E_{CBM} . Looking at E_{VBM} and E_{CBM} as the **highest occupied** and the **lowest unoccupied** states respectively, it is interesting to note that, for metals, both the electron affinity and the ionization potential are equal to the work function.

2.3.2 Surface States

The periodic pattern of chemical bonds in the crystal is interrupted at the surface, resulting in unsaturated (dangling) bonds, which can rearrange themselves (surface reconstruction). This results in a change of both the surface crystal structure and the allowed energies that depend sensitively on the materials and bulk crystal structures involved. This is particularly evident in semiconductors, which are characterized by high-directional chemical bonds. Often, the electronic surface structure is very different from the bulk structure, giving rise to surface states inside the bulk forbidden energy gap. A simple motivation for formation of electronic surface states goes as follows: Bloch's theorem in principle allows the wave vector in the wave function $\psi_k(r) = u_k(r)e^{ikr}$ to be a complex number. An imaginary wave vector corresponds to an exponentially damped wave function. In a crystal this solution has no physical meaning because it would imply a localization of the wave function into the crystal, violating the translational symmetry. But the surface breaks translational symmetry, therefore allowing wave vectors with nonzero imaginary component. It can be shown that the resulting states are localized at the surface, with a wave function amplitude that decays exponentially over a few lattice constants when going from the surface into the bulk. It turns out that the energies of these states are usually located inside the band gap, forming surface states. The surface states can be probed, for example with either scanning tunneling techniques or photo-emission spectroscopy.

2.4 Surface states in the Nearly-Free Electron model

To give an idea of existence of surface states inside the band gap, we can consider as the simplest model of a bulk truncation, a semi-infinite chain of identical, periodically arranged, atoms [49]. The end of the chain thus represents the surface. In the sense of **nearly-free** electron model, we assume a sinusoidal behavior of the potential along the chain. As shown in Fig. 2.3a, an abrupt potential step V_0 comes at the surface. The Schrödinger to be solved is:

$$\left[-\frac{\hbar^2}{2m} \frac{d}{dz} + V(z) \right] \psi(z) = E\psi(z) \quad (2.4)$$

with

$$\begin{cases} V(z) = V_g \cos\left(\frac{2\pi}{a}z\right) & z \leq 0 \\ V(z) = V_0 & z > 0 \end{cases} \quad (2.5)$$

Deep inside the crystal ($z \ll 0$), the potential $V(z)$ can be considered periodic, leading to the well known bulk solutions. Away from the Brillouin zone boundaries, the electronic states behave like plane waves and their energies are those of free electrons with a parabolic dependence on the wave vector k . In fact, for small values of k , the wavelength is much larger than $2a$, so that waves will not sense the periodicity in the potential, but only the average value. On the other hand, near the boundaries ($k = \pm\pi/a$), Bragg reflection takes place. The wave function is the sum of waves of equal amplitude, behaving like a standing wave. There are two possible linear combinations leading to standing waves and hence two solutions at the zone boundary, with different energies due to $V(z)$, leading to the well known band splitting. For k values near π/a , the wave function can be taken in the following two-wave form:

$$\psi(z) = Ae^{ikz} + Be^{i(k-2\pi/a)z} \quad (2.6)$$

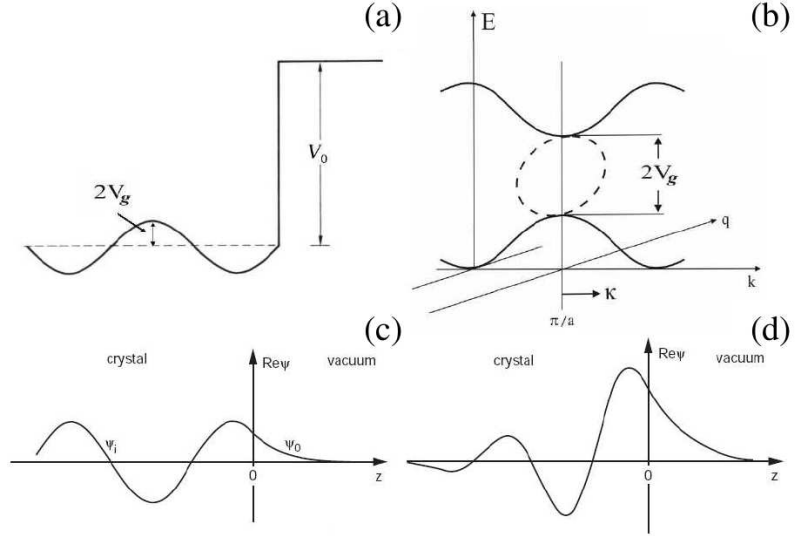


Figure 2.3: (a) A schematic representation of the potential is proposed for semi-infinite chain in the nearly-free electron model. (b) The bulk energy bands are represented by filled lines, while dotted lines represent the range of values for the solution corresponding to the surface states. This solution is obtained for complex values of the wave-vector $k = \pi/a + \kappa = \pi/a + iq$. The bulk (c) and surface (d) states are shown close the surface ($z=0$). Both are matched to an exponential decay into the vacuum. The surface state also decay exponentially into the bulk.

The substitution of Eq. 2.6 into the Schrödinger equation yields the matrix equation:

$$\begin{bmatrix} \frac{1}{2} \frac{\hbar^2}{2m} k^2 - E(k) & V_g \\ V_g & \frac{\hbar^2}{2m} \left(k - \frac{2\pi}{a}\right)^2 - E(k) \end{bmatrix} \begin{bmatrix} A \\ B \end{bmatrix} = 0 \quad (2.7)$$

Solving Eq. 2.7 for $k = \pi/a + \kappa$, where small values of κ correspond to the interesting k range, the eigenvalues are obtained:

$$E = \frac{\hbar^2}{2m} \left(\kappa + \frac{\pi}{a}\right)^2 \pm V_g \left[-\frac{\hbar^2 \pi}{ma V_g} \kappa \pm \sqrt{\left(\frac{\hbar^2 \pi}{ma V_g} \kappa\right)^2 + 1} \right] \quad (2.8)$$

This leads to the formation of allowed and forbidden energy bands, as schematically represented by filled lines in Fig. 2.3b, with an energy gap equal to $2V_g$.

Let us look at the eigenfunctions near the surface ($z=0$). The solutions are made of a part (ψ_o) compatible with a constant potential V_0 for $z > 0$, that is an exponential decay, matching the standing wave solution ψ_i for $z \leq 0$, as shown in Fig. 2.3a. The matching conditions at $z = 0$, imposed on both the wavefunctions and their derivatives, are satisfied for every possible energy eigenvalue within the bulk allowed bands. The bulk electronic band structure exists up to the very surface of the crystal with only slight alterations.

Thanks to the breaking of the translational symmetry, new surface solutions are allowed by considering complex wave vectors. Letting k to be imaginary, so that $\kappa = iq$, it can be shown [49] that the new solutions have the following form inside the crystal (that is, for $z \leq 0$):

$$\psi'_i = C e^{qz} \left\{ \exp \left[i \left(\frac{\pi}{a} z \pm \delta \right) \right] \mp \exp \left[-i \left(\frac{\pi}{a} z \pm \delta \right) \right] \right\} e^{\mp i \delta} \quad (2.9)$$

with δ defined by:

$$i \sin(2\delta) = -i \frac{\pi}{a} q \quad (2.10)$$

The corresponding eigenvalues are

$$E = \frac{\hbar^2}{2m} \left[\left(\frac{\pi}{a} \right)^2 - q^2 \right] \pm V_g \sqrt{1 - \left(\frac{\hbar^2 \pi}{ma V_g} q \right)^2} \quad (2.11)$$

The values of E are real if $0 < q < V_g / \left(\frac{\hbar^2 \pi}{2m a} \right)$ so that all the energies fall into the forbidden band, as shown by the dotted line in Fig. 2.3d.

In this case internal ($z \leq 0$) wavefunction ψ'_i is essentially a standing wave with exponentially decaying amplitude inside the crystal, matching the external solution ψ_o , exponentially decaying into the vacuum (see Fig. 2.3b):

$$\psi_o = D \exp \left[-\sqrt{\frac{2m}{\hbar} (V_0 - E)} z \right] \quad \text{with} \quad E < V_0 \quad (2.12)$$

This means that the loss of periodicity leads to a localized solution at the surface. As before, the matching conditions are imposed on both the wavefunctions and their derivatives so that:

$$\psi_o(z=0) = \psi'_i(z=0) \quad ; \quad \left. \frac{d\psi_o}{dz} \right|_{z=0} = \left. \frac{d\psi'_i}{dz} \right|_{z=0} \quad (2.13)$$

There are two matching conditions for two free parameters, that are the energy eigenvalue E and the ratio C/D of the wavefunction amplitudes. This implies that there is only one solution allowed in the forbidden bulk energy gap. The corresponding wavefunction is essentially localized at the surface, giving rise to a surface state. The semi-infinite chain in the nearly-free electron model thus yields one single electronic surface state which is localized somewhere inside the gap of the bulk states.

2.5 Surface states from a chemical point of view: dangling bonds and dimerization

Semiconductor surfaces tend to reconstruct in complicated ways rather than staying bulk terminated. For understanding the surface states on semiconductors, let us look at the bonding in these materials first. The elemental semiconductors as Si and Ge and many of the common compounds such as GaAs exhibit a tetrahedral bonding geometry. Fig. 2.4a shows a bulk termination along the (001) direction of a tetrahedrally bonded semiconductor, in other words, a (001) oriented surface without reconstruction. As shown in Fig. 2.4c, when the surface is formed, the sp^3 hybrid bonds are cut and dangle into the vacuum. In a band structure picture, considering one dangling bond per unit cell, we can describe the dangling bond state by a band. If the band is fully occupied it can accommodate two electrons. But the dangling bond state has only one electron and hence the band has to cross the Fermi level such that only one half of the surface Brillouin zone has occupied states due to the dangling bond. In this description, the semiconductor surface would have a metallic behavior. Nevertheless this does not happen very often. What really happens is that the semiconductor surfaces reconstruct in complicated ways recombining the

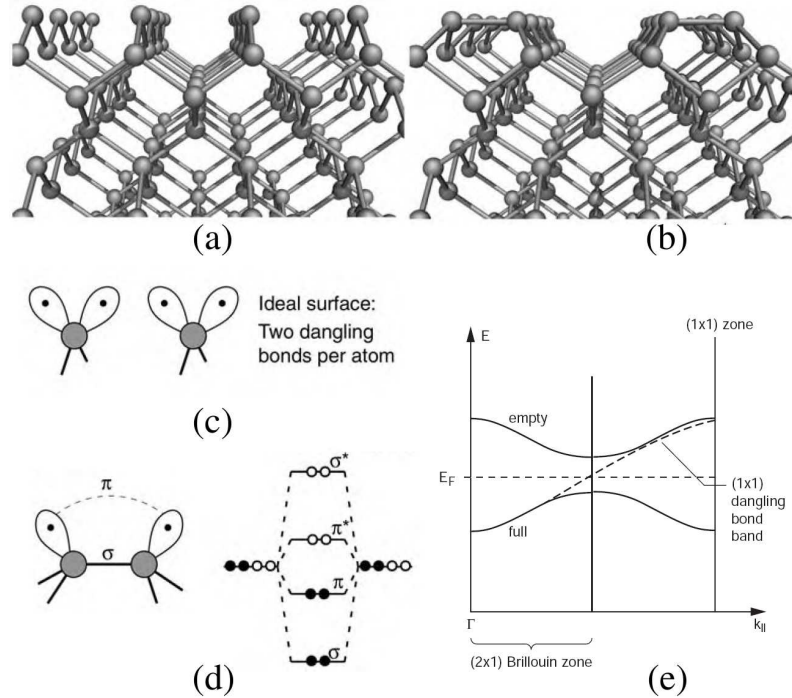


Figure 2.4: Schematics representation of (a) ideal and (b) reconstructed (001) surface of a tetrahedrally bonded semiconductor. The dangling bonds, shown in (c), recombine giving rise to dimers formation (d). (e) Dimerization dramatically changes the surface band structure of the ideal surface.

dangling bonds. This concept is nicely illustrated in Fig. 2.4. In the ideal bulk termination (Fig. 2.4a) each atom at the surface is left with a pair of dangling bonds (Fig. 2.4c) which is energetically unstable. The surface energy is lowered after the surface atoms pair up (Fig. 2.4b), reducing the number of dangling bonds. Within each pair of atoms (Fig. 2.4d), or **dimer**, each atom contributes a dangling bond to form a strong σ -bond (which significantly lowers the surface energy), while the remaining two dangling bonds (one per atom) interact weakly forming a π -bond. The dimer row formation, or **dimerization**, saturates the dangling bonds, lowering the surface energy. The main effect on the electronic band structure is to split the half-filled dangling bond band into two respectively filled and empty dimer bands (Fig. 2.4e). Dimerization is a very complex mechanism. The dimers do not stay,

in general, parallel to the surface as shown in Fig. 2.4b, but often they are tilted, giving rise to different surface reconstructions and band structures. In the following chapter, a particular reconstruction of the silicon (001) oriented surface will be analyzed in detail.

2.6 Band Bending and Fermi Level Pinning

In the case of a doped semiconductor, the existence of surface states in the gap can have a dramatic effect on the electronic structure rather far away from the surface, known as the **band bending**. To understand the meaning of this effect, let us consider a semiconductor with two surface state bands, respectively empty and occupied, with the Fermi level in between.

For an n-doped semiconductor, the bulk Fermi level would be close to the bottom of the conduction band. On the other hand, the position of the surface states in the gap is such that the surface Fermi level would lie to a much lower energy than the bulk Fermi level (see Fig. 2.5a). This configuration is unstable because it brings bulk donors above the surface Fermi level. Donor electrons will flow into the previously unoccupied surface states and partially fill them. At the same time, they will leave a layer of positively charged bulk donors behind. The former process induces energy gain, the latter energy loss needed for setting up an electric field in the surface region. The charge flux will be sustained until balancing between the two energies is achieved. At the end, the Fermi level is constant over the whole crystal and surface, as shown in Fig. 2.5b. The total effect is that energy bands bend downwards going from the surface region to deep inside the crystal, crossing the Fermi level. The ionized bulk donors represent a positive space charge, so called **space charge layer**. A similar description can be done in the case of a p-doped semiconductor, with bands bending upwards going from the surface to the bulk.

A related consequence is the so-called **Fermi level pinning** by surface states in the gap. In the bulk, the Fermi level can be changed from just below the conduction band to just above the valence band by changing the doping. One would expect that the work function, i.e. the distance between the Fermi level and the vacuum level would follow this change. But for certain surfaces with states in the gap this

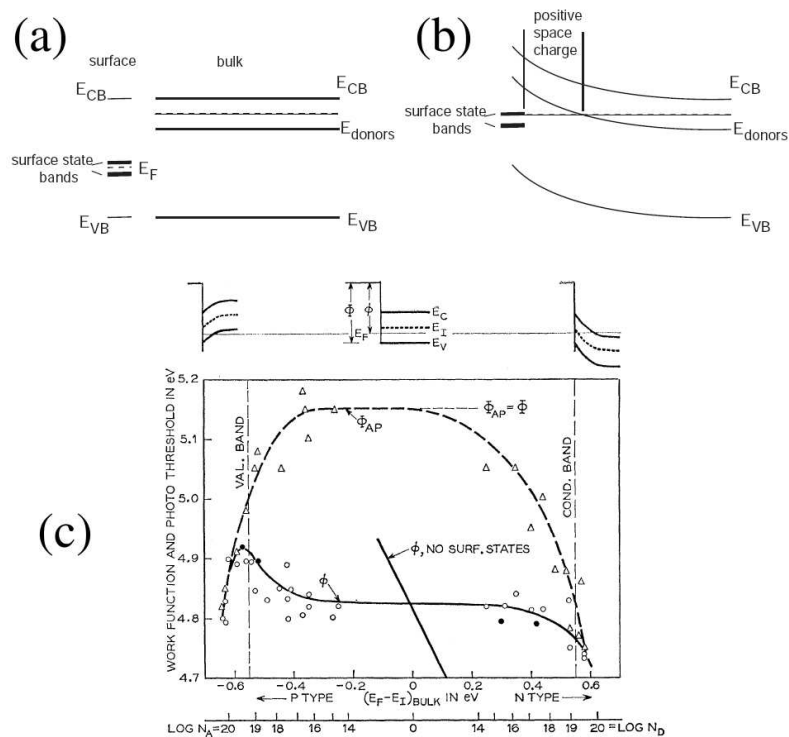


Figure 2.5: The band bending is depicted as a transition from an unstable condition (a) in which the surface Fermi level does not match the bulk one, to a stable condition (b) in which the Fermi level is constant over the whole crystal and surface. A direct consequence of the band bending is that the Fermi level is limited to move between the occupied and empty surface states, as shown by measurements [50] of work function variation (c) on the (111) silicon surface.

is not the case. In Fig. 2.5c the well known result of Allen and Gobeli [50] is shown, bringing out the Fermi level pinning of the (111) oriented silicon surface. By changing the doping, the bulk Fermi level goes from the top of the valence band to the bottom on the conduction band, separated by an energy gap of about 1.1 eV. At the same time, the measured work function variation is only of about 0.2 eV. As previously described, the Fermi level remains locked between the occupied and empty surface states while bulk bands bend downwards or upwards depending on the doping, because of the space charge layer formation.

2.7 Surface functionalization

The previous discussion concerns clean surfaces. Adsorbed atoms and molecules may have significant influence in the electronic structure of the surface. Chemical adsorption (or **chemisorption**) changes surface reconstruction as well as leads to new charge redistribution at the surface due to chemical bonds formation in the adsorption. Considering semiconductor surfaces, chemisorption can lead to a partial or total saturation of the dangling bonds, causing dramatic variations of the surface states. For example, a total saturation of the dangling bonds can lead to the disappearance of the surface states inside the band gap, removing the band bending and the related pinning of the Fermi level. Moreover, adsorbed molecules with own static dipole moment add elementary dipoles in the surface rising or lowering the total surface dipole layer, with a resulting change of the work function and all the related quantities (e.g. the electron affinity).

Therefore, the so called **surface functionalization** leads to new opportunities of tuning all the physical properties connected to surfaces and interfaces between materials. The main goal of the next chapter will be to show the interplay between surface functionalization and surface properties in the case of the Si (001) surface.

Chapter 3

An overview of some experimental techniques

Overviews of several of the many experimental techniques used to study the electronic and structural properties of functionalized surfaces and hybrid organic-inorganic compounds have been given in this chapter.

3.1 Low energy diffraction (LEED): structure determination

Low-energy electrons are for surface structure what X-rays are for the bulk. In fact, the mean free path for low energy electrons in solids is short and therefore any technique based on such electrons is rather surface sensitive; furthermore the electron de Broglie wavelength $\lambda = h/p$ fits very well with the typical distances in crystals and thus diffraction phenomena are to be expected.

As we shall see below there are two major applications for LEED. The first one concerns the pure inspection of the surface diffraction pattern. One short LEED experiment gives immediate and direct information about the surface order and quality. When the surface is reconstructed or covered with adsorbates, the LEED images can quickly give some information about the surface symmetry and periodicities. The second application of LEED is the quantitative structure determination.

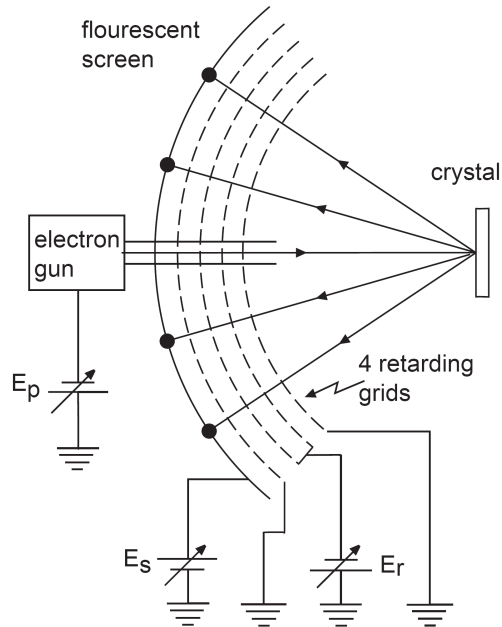


Figure 3.1: A LEED system.

One has to measure the diffraction intensities as a function of the incidence electron energy and compare them to sophisticated multiple-scattering calculations for a model system. This model system has to be changed until good agreement between calculations and experimental intensities is achieved. Fig. 3.1 shows a typical LEED apparatus which can be found in almost every surface science vacuum chamber. The LEED system has two major components: an electron gun producing monochromatic electrons and a detector system which detects only the elastically scattered electrons. The detector consists of four metal grids at different voltages and a fluorescent screen. The first grid (counted from the sample) is on ground potential to ensure a field free region around the sample. The next two grids are set to the so-called retarding voltage. This voltage is slightly lower than the kinetic energy of the electrons produced by the gun. It repels almost all the inelastically scattered electrons. The elastically scattered electrons pass the next grid which is set to ground voltage again and are then accelerated towards the fluorescent screen

which is set to a high positive voltage. Behind the screen there is a window in the vacuum system so that the LEED pattern can be observed directly or recorded with a video camera. This technique has been extensively used to perform the initial investigations of ethylene vibrational spectra [51] and acetylene [52].

Ethylene (C_2H_4) was the first organic molecular adsorbate on Si (001) for which a structure was determined: the initial investigations by means of electron energy loss spectroscopy (EELS) determined that the molecule attains a di- σ bonded arrangement. Subsequently, the thermal desorption of ethylene was studied and a barrier to desorption of 1.65 ± 0.07 eV was extracted. It was shown that essentially all ethylene molecules desorbed intact. Acetylene was first studied by Nishijima et al [52], who used EELS, LEED and thermal desorption techniques and observed a di- σ bonded model of the adsorption geometry, a structure analogous to that assigned to adsorbed ethylene. It was shown that acetylene remains intact below room temperature, but at elevated temperatures Si-H stretching was visible, indicating that molecule decompose. It was also shown that preadsorption of atomic hydrogen on Si (001) saturates the silicon dangling bonds and blocks acetylene adsorption. The adsorption and decomposition of acetylene on Si(001) has been studied also in Ref. [53], where it was argued that the affected Si-dimer bond was cleaved on formation of the complex. In 1992 EELS was again applied to acetylene-Si(001) [54]. A key feature, not observed in previous works, was that the C-C stretch at 1450 cm^{-1} ; it was determined that a C-C double bond existed and that therefore the C-atoms were sp^2 hybridized. This analysis also pointed out that the $\sim 3000\text{ cm}^{-1}$ C-H stretch was as expected for an sp^2 C-atom bound to silicon. Even if these results shed light in the understanding of such structures, further investigation was required. The development of scanning tunnelling microscopy was fundamental for the complete characterization of such systems.

3.2 Scanning tunnelling microscopy

It is clearly desirable to have a real-space microscopic technique which can image the structure of surfaces on a truly atomic scale. Field emission microscopy is a possibility with a rather limited range of possible applications. First the advent

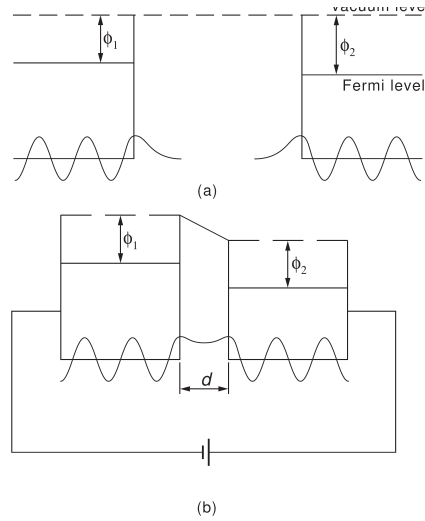


Figure 3.2: (a) Exponential leakage of the wavefunctions from a conductor into the vacuum. (b) Application of a voltage and tunnelling between two conductors because of the overlap of the wavefunction tails. Φ is the workfunction.

of scanning tunnelling microscopy (STM) has made a real space atomic scale view on most surfaces possible, but it is worth to notice that STM does not measure the structure of surfaces but, as we shall see below, the electronic structure. It is essential to keep this in mind, in particular when working with semiconductors and insulators.

Scanning tunnelling microscopy is based on the quantum mechanical effect of tunnelling illustrated in Fig. 3.2. The wavefunctions at the Fermi level exponentially leak out of the metal with an inverse decay length of $\kappa = \hbar^{-1}(2m\phi)^{1/2}$ where m is the mass and ϕ is the work function. If now two metals are brought in close contact and a small voltage is applied between them, a tunnelling current $I_t \propto \exp(-2\kappa d)$ can be measured, where d is the distance between the conductors. The important message here, and the reason why STM works, is the exponential dependence of the tunnelling current on the distance between the conductors. Fig. 3.3 shows the schematic setup for an STM. It consists of a sharp tip, very close to the sample, which can be moved with high precision using three mutually orthogonal piezoelectric transducers (PET). A small voltage is applied between the tip and the sample, and

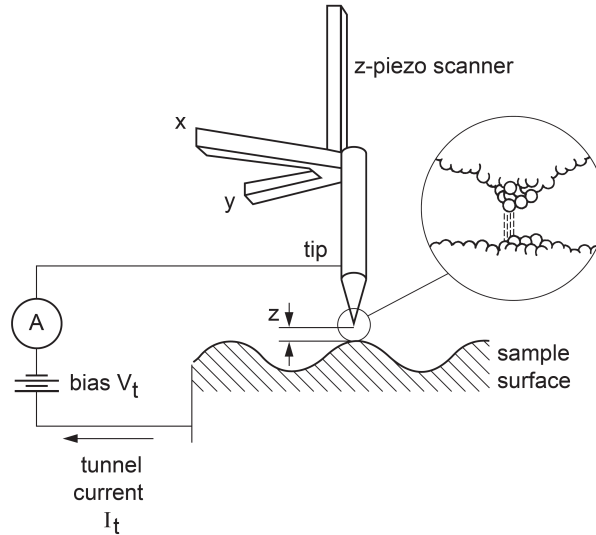


Figure 3.3: Schematic construction principle of an STM.

the current is measured. Typical values for the tunnelling voltage are from a few mV to several V or so and for the current from 0.5 to 5 nA. The tip-sample distance is a few Angstrom. The tunnelling current depends very strongly on this distance. A change of 1 \AA causes a change in the tunnelling current by a factor of ten. While the principle of STM operation is simple, its practical realization faces some difficulties. The first is that the tip has to be brought at a distance of a few Angstrom from the surface and has to be stabilized there with sub-Angstrom stability. This process has to be performed in the presence of mechanical vibrations and thermal drift. The vibrational problem is solved by vibrational insulation, like suspensions by springs or the use of a support frame which has a resonance frequency very different from the usual noise frequencies of the environment. The only way to get completely rid of the thermal drift problem is to stabilize the whole microscope and sample at the same (low) temperature. The most stable STMs today are working in a UHV vessel which is placed inside a dewar filled with liquid Helium. The next practical problem is to make an atomically sharp tip. Different techniques are used like cutting and etching and most tips are made with either Tungsten (W) or Iridium (Ir). Also in this case, the exponential decay of the tunnelling current helps: one

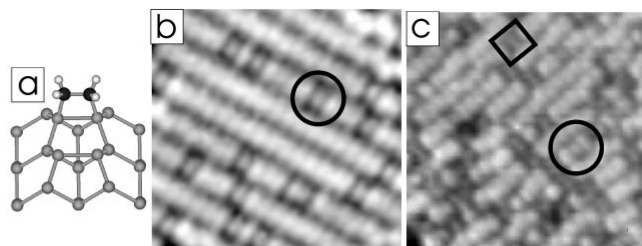


Figure 3.4: (a) Model of adsorbed ethylene on Si(001) in the di-s configuration. (b) Occupied-state STM image of ethylene on Si(001) (93A). (Open circle) One adsorbate. (c) Occupied-state image of acetylene on Si(001) (from Reference 47). (Open square) A bridge-bound molecule; (circle) a one-dimer bound molecule. [2]

can hope that there is one single atom sticking out a little further than all the others on an otherwise rather blunt tip. Then most of the tunnelling will happen through this atom and it will be possible to obtain images with atomic resolution. Unfortunately, it is not possible to prepare a tip in a controlled and reproducible way. In particular, one has no control about the chemical nature of the outermost atom of the tip but the images depend a lot on this. Atomic resolution is much easier to get on semiconductor than on metal surfaces. The reason is the higher corrugation of the latter. STM can also be helpful to get some starting ideas about the complex structures in semiconductor reconstructions which can then be refined by a “real” structural analysis like LEED or surface X-ray diffraction. On the other hand, the more directional bonding in semiconductors should make the interpretation of STM images as pure atomic structure even more problematic than on metal surfaces. In 1992, STM was used to examine ethylene-Si(001) [55]. An STM image is shown in figure 3.4b. Uniquely, the STM results indicated that adsorbates prefer to avoid nearest-neighbours positions. Figure 3.4a shows the symmetric structure of the adsorbate for ethylene-Si(001). The C-C bond adds across, and becomes parallel to, a Si dimer. Only this adsorption geometry is observed; the molecule is not observed to bridge dimers in a row or in adjacent rows. The Si-Si dimer bond increases from 2.26 Å to 2.33 Å, the dimer clearly remains intact [56]. The C-C double bond, originally 1.34 Å in length, is reduced to a single bond of 1.52 Å. The C-atoms rehybridize from sp^2 to sp^3 as they become four-coordinate, forming σ -bonds

with the Si dimer dangling bonds. The Si-C bonds are calculated to be 1.93 Å, in correspondence with the 1.89 Å bond length known for SiC. Fisher and coworkers have shown that a simple STM simulation well describe ethylene-Si(001) [57, 58]. Constant-charge density contours predict the molecule to appear slightly higher than do clean dimers. In simulations including the effects of the electric field, the dimers appear a little higher than the adsorbate, in accordance with experiment. It emerged that the electron density associated with the clean dimer dangling bonds is more polarizable than that in the vicinity of the molecule. This detailed understanding of image contrast may prove useful in the future. As a practical point, it is worth to notice that an adsorbate about 2 Å above the Si(001) surface appears about as high in STM contours as the clean dimers.

3.3 Kelvin probe method

To measure the work function at the surface of materials, different techniques have been developed. Work function can be measured directly by means of techniques based on termoionic or photoelectric effects, or through differential methods as the Kelvin Probe technique, that provides a measure of the difference of the work function of two materials. In the following, the Kelvin Probe technique is described in detail.

The Kelvin probe technique takes its name from William Thomson, also known as Lord Kelvin, who first introduced it in 1898 [60] to explain the formation of built-in contact potential differences in metals, previously observed by Alessandro Volta at the beginning of the 19th century. This phenomenon can be explained as follows. When two plates of a capacitor composed of different materials are electrically wired together (Fig.3.5b), electrons will flow from the material with the lower work function (weak electron binding, ϕ_2 in the figure) to the one with the higher work function (strong electron binding, ϕ_1 in Fig.3.5), generating opposite charges on the capacitor plates and a contact potential difference (CPD) between the two materials. To detect the electrical field in the capacitor, an external potential V_c can be applied to cancel this field. At equilibrium, the field is zero, and the externally applied potential equals the contact potential difference, which corresponds to the

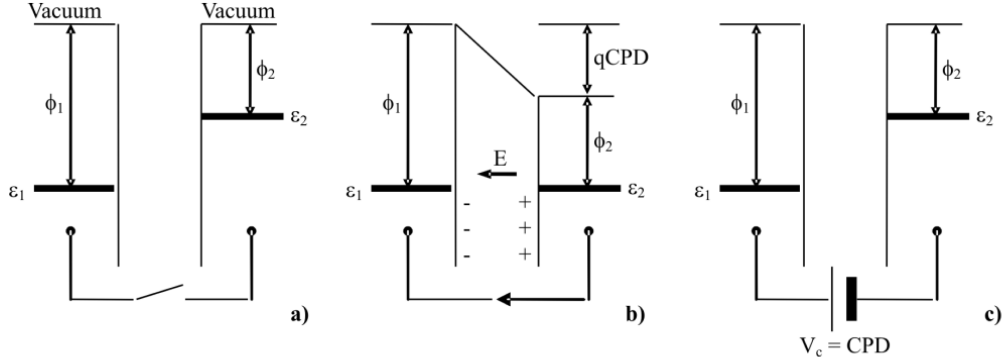


Figure 3.5: Schematic diagram of Kelvin Probe physics. a) Two materials 1 and 2 with different work functions ϕ_1 and ϕ_2 , corresponding to the energy difference between the Fermi level e and the vacuum level. b) When the two materials are electrically contacted, electrons flow from 2 to 1 until the Fermi levels are aligned, leading to a contact potential V_b . The charges present in the two materials causes an electric field E . q : electron charge; CPD: contact potential difference. c) The electric field is removed by applying an external potential V_c which equals the contact potential. [59]

difference between the two work functions (Fig. 3.5c). Once the work function of the reference plate (ϕ_1) is known, we can measure the work function of the material under study $\phi_2 = \phi_1 - qV_c$, where q is the elementary charge. In 1932, Zisman improved the method by using a vibrating reference surface [61]. The mechanical oscillation at frequency ω induces changes in the system capacitance and thus in the reference plate voltage. The variations of capacitance generate a small alternating current. In fact, a periodic vibration of the distance between the two plates at ω results in a current $i(t)$ given by [62] $i(t) = V_c \omega \Delta C \cos(\omega t)$ where V_c is the contact potential difference and ΔC is the capacitance variation. For the actual measurement of the CPD, an additional voltage is applied between the two plates until the field cancels out and the current $i(t)$ goes to zero. The Kelvin probe technique has been used for macroscopic measurements of many materials by tracking shifts in the contact potential due to changes in the work function of the sample surface and to surface photovoltage effects [63, 64]. The resolution was even down to ~ 1 mV. Nevertheless this technique gives no information on the local ϕ variation on sample surface, measuring an average of the local work functions over the whole

sample surface. Wickramasinghe and co-workers [62] developed Kelvin probe force microscopy (KPFM). In this setup, the reference capacitor plate is a sharp conductive scanning force microscopy (SFM) tip attached to a very flexible cantilever. The tip-sample interaction is highly localized, and potential differences between tip and sample can be detected by measuring the deflection of the cantilever due to electrostatic interactions, allowing measurement of ϕ with high spatial and electrical resolution. The principle is similar to the Kelvin method, but forces instead of currents are measured. The application of an oscillating potential V_{ac} at frequency ω lead to an oscillation mode at the same frequency of the cantilever, detected by SFM photodiode. The oscillation amplitude at frequency ω is proportional to the surface-potential difference between tip and surface. Nevertheless, this interaction could not be exactly quantified due to the complexity of the system dynamics and tip shape. Alternatively, qualitative two-dimensional (2D) maps of the surface potential can be obtained with the electrostatic force microscopy (EFM) technique. In order to obtain an exact measurement of the work function of the sample, an additional feedback loop is added. This loop applies a given direct current (DC) offset potential voltage (V_{dc}) to the cantilever tip to minimize the electrostatic interaction between the tip and the surface (Fig.3.6). Both an alternating current (AC) and a DC voltage bias signal are then applied between the tip and the sample. In this case, the voltage between the tip and the sample can be expressed by $\Delta V = \Delta\phi - V_{dc} + V_{ac}\sin(\omega t)$ where $\Delta\phi$ is the contact potential (difference in work function between the tip and the sample), V_{dc} is the DC offset potential applied to the tip, and V_{ac} and ω are the amplitude and frequency of the applied AC voltage signal, respectively.

Kelvin probe microscopy provides insight into band bending, even with materials with poor electrical properties [65], such as organic semiconductors. For such materials the conventional techniques applied for band-bending measurements, such as ultraviolet photoelectron spectroscopy or X-ray photoelectron spectroscopy, cannot be used: the high resistance of the organic materials causes the sample charging during the measurement. In fact, in organic materials applied as active components in electronic devices, the highest occupied molecular orbital–lowest unoccupied molecular orbital (HOMO–LUMO) gap is typically 2–3 eV. The concentration of thermally excited carriers is extremely small, like that of an insulator. Consequently, the

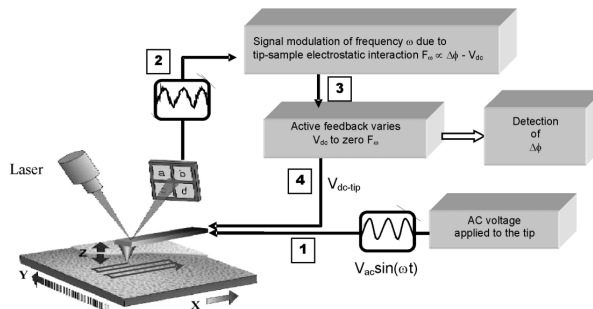


Figure 3.6: KPFM apparatus. 1) An alternating voltage V_{ac} is applied to the tip with a frequency ω . 2) The electrostatic tip–sample interaction induces a mechanical oscillation of the cantilever at a frequency ω . 3) The cantilever oscillation at ω is isolated using a lock-in amplifier and sent to a feedback circuit. 4) The feedback tries to minimize F_{ω} (which is proportional to the tip-sample interaction) by adding a V_{dc} voltage onto the tip. A different setup is in some cases exploited where the external potential bias is applied directly to the sample. [59]

formation of valence and conduction bands, thermal equilibrium, and thus Fermi-level alignment and band bending at the interfaces cannot be assumed a priori since the HOMO–LUMO separation is usually much larger than the thermal energy.

In inorganic semiconductors, the surface states typically lie in the forbidden gap and can pin the Fermi level at the surface, hindering band bending. For organic semiconductors, the surface states are usually outside the optical gap, and thus surface-states pinning is less common [65]. Furthermore, even surface states associated with dangling bonds present at cleaved surfaces of inorganic semiconductors typically pin the Fermi level and hinder any electrostatic measurement of the band structure in the bulk. These surface charges are generally absent in van der Waals'-bonded organic materials, making KPFM particularly suitable for organic compounds [66]. Interesting measurements have been performed by Cahen and coworkers [85], furnishing the values of work function and related quantities in different semiconductor surfaces covered by benzoic acids.

3.4 Bulk analysis of perovskites: X-ray and adsorption measurements

The relevant interactions giving rise to crystalline assembly within the hybrid perovskites include covalent/ionic bonding (which favors the formation of sheets of corner-sharing metal halide octahedra), hydrogen/ionic bonding between the organic cations and the halogens in the inorganic sheets, and various weaker interactions (e.g. van der Waals) between the organic R-groups. Given the good solubility of many metal halides in polar organic and aqueous solvents, as well as the strong tendency to self-assemble, single crystals of the organic-inorganic perovskites can generally be grown from near-ambient-temperature saturated solutions containing the relevant metal halide and organic salts [14, 67]. While single crystals are generally the most useful medium for examining structural and physical properties of the hybrids, many electronic and optical applications require the ability to deposit thin films. One of the important advantages of organic-inorganic perovskites and related hybrid materials is the possibility of processing the materials using a number of simple solution-based or evaporative thin-film techniques [14].

3.4.1 X-ray analysis

X-ray diffraction analysis allows to determine the crystal structure, the crystalline degree, or the distribution of the grain orientations [36]. The oriented structure of a crystal behaves like a diffraction reticulum for X-ray radiation and the interference spectrum that is generated contains a large amount of information on the crystal itself. In particular the Bragg law holds reticular spacing information: $2d \sin \theta = n\lambda$, where λ is the X-ray radiation wavelength, n is an integer number, θ is the reflection angle set equal to the incidence angle, d is the distance between two reticular planes and depends on the particular set of planes considered, as classified according to the Miller scheme [36]. Using the relation written above, it is possible to measure the crystal lattice parameters. In the $\omega - 2\theta$ (or $\theta - 2\theta$) scan diffraction measurements, incidence and reflection angle ω and θ are changed simultaneously so that the condition $\omega = 2\theta/2$ is always satisfied (symmetrical configuration: here 2θ is the angle between the incident source ray and emerging ray, while is the

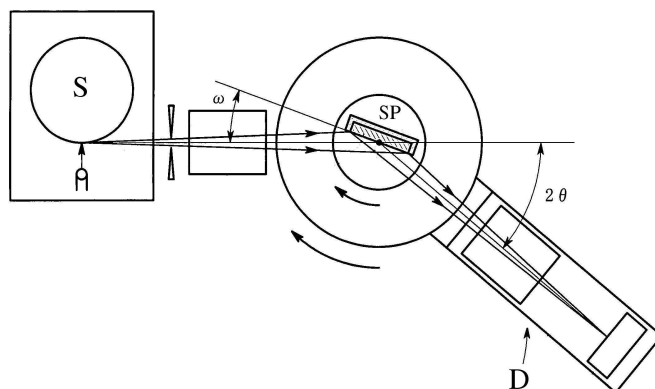


Figure 3.7: Schematic representation of an automatic diffractometer Bragg-Brentan geometry type. S is the X-ray source, D the detector of diffracted ray, SP the sample holder.

angle between the sample surface and the incident ray). In Fig.3.7 the apparatus is schematically represented. When the reflection angle catches up the value for which the relation of constructive interference, given by the Bragg law, holds, a strong signal is observed at the detector corresponding to a peak in the intensity vs. 2θ spectrum. When the measurement is carried out on a randomly oriented powder, the peak intensity depends on the intrinsic details of the crystal structure. If the measurement is carried out on films, by comparing the results with the corresponding powder spectrum, it is possible to get information also on the possible preferential orientation of the film grains. As an example, the presence in the spectrum of intense peaks corresponding to the Miller indices (0 0 l), indicates that film has grown orienting crystallographic axis c in the direction normal to the substrate plane. In this case from the width of the diffraction peak it is possible estimate the degree of preferential orientation. Room temperature diffraction analysis of polycrystalline powders of the organic-inorganic compound $\text{CH}_3\text{NH}_3\text{SnCl}_3$ (Fig.3.8(c)) has revealed that the powders do not result cubic, but distorted in a monoclinic or triclinic phase. As reported by Yamada [35] these two distorted cubic structures show only minor differences. The differences of the cell parameters (α and γ angles [68] change from 90 degrees to 90.37 and 90.05 degrees respectively) do not result appreciable by our analysis, however monoclinic refinement was carried out. From the analysis of the

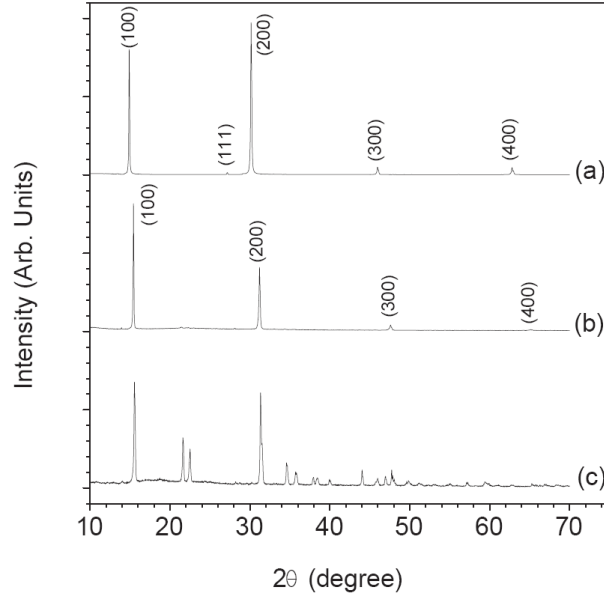


Figure 3.8: X-ray diffraction patterns of (a) $\text{CH}_3\text{NH}_3\text{SnBr}_3$ and (b) $\text{CH}_3\text{NH}_3\text{SnCl}_3$ films. The diffraction pattern of the powders of $\text{CH}_3\text{NH}_3\text{SnCl}_3$ compound are labeled as (c) [70].

diffraction patterns of the films of both compounds reported in Figs. 3.8 (a) and (b), the films result to be single phase. $\text{CH}_3\text{NH}_3\text{SnBr}_3$ diffraction pattern is compatible with a cubic perovskite structure [69]. The presence of the $(l\ 0\ 0)$ set of reflections in the films of both compounds gives an indication about the good crystallization and the occurrence of a dominant crystallographic orientation.

3.4.2 Absorption measurements

Analysis of the absorption data was carried out to test the optical quality of SSTA deposited films as well as to determine the predominant optical transition and electronic configuration (presence of excitonic states transition) of the $\text{CH}_3\text{NH}_3\text{SnX}_3$ series. The optical transmittance of the films was recorded using the unpolarized light generated by a set of lamps, by a JASCO V-530 dual beam scanning spectrophotometer in the energy range 1.1–6.5 eV. The surrounding medium was air and all

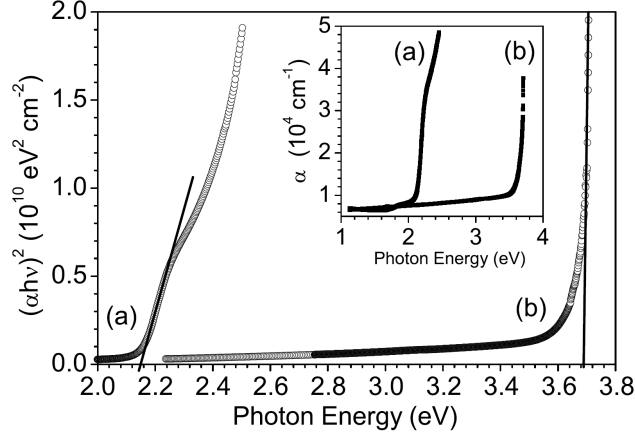


Figure 3.9: Fitting to the $(\alpha h\nu)^2 \propto (h\nu - E_g)$ equation, describing direct band-gap allowed transitions for (a) $\text{CH}_3\text{NH}_3\text{SnBr}_3$ and (b) $\text{CH}_3\text{NH}_3\text{SnCl}_3$ films on quartz. The inset shows the absorption coefficient spectra of the films of both compounds [70].

the measurements were performed at room temperature. Transmittance is related to the absorption coefficient α by the relation:

$$T = \frac{(1 - R)^2}{1 - R^2} \exp(-\alpha d) \quad (3.1)$$

where T is the transmittance, and R is the reflectance and d is the thickness of the sample.

The absorption coefficient α can be estimated in low reflection approximation $R \simeq 0$, as $\alpha = \ln(1/T)/d$, where the quantity $\ln(1/T)$ is usually referred to as “absorbance”. The absorption coefficient of a crystalline solid obeys the following relationship [71]:

$$(\alpha h\nu) \propto (h\nu - E_g)^r \quad (3.2)$$

where E_g is the optical energy gap, and r is an exponent that characterizes the optical absorption process. The temperature dependence of the absorption coefficient can be measured installing a cool finger onto the spectrophotometer.

Absorbance of 500 nm thick films were measured in air at room temperature. The absorption coefficient α , shown in the inset of Fig. 3.9, was obtained by including corrections for multiple reflections. It can be seen that the absorption edge rapidly

raises to values typical for direct band-gap crystals ($\alpha \sim 10^4 - 10^5 \text{ cm}^{-1}$). As such, it can be described [72] by the relation $(\alpha h\nu)^2 / (h\nu - E_g)$, as shown by the linear slope in Fig. 3.9. In the case of $\text{CH}_3\text{NH}_3\text{SnBr}_3$, the presence of a bump is related to an overlap of multiple direct gap contributions to the absorption. Multiple direct band gaps are evident from the calculated band structure (see chapter V). The obtained gap and resistivity values together with previously reported metallic reflectivity and resistivity [119] observed for $\text{CH}_3\text{NH}_3\text{SnI}_3$ compounds show a decrease upon changing the halogen atoms along the $\text{CH}_3\text{NH}_3\text{SnX}_3$ series $\text{Cl} \rightarrow \text{Br} \rightarrow \text{I}$. This can be correlated with the decrease of the Pauling electronegativity of the halogen atom (X) (3.16, 2.96, 2.66 for Cl, Br, I respectively), resulting in the reduction of the ionicity of the Sn-X bond. To better understand and explain this empirical consideration, we discuss in chapter V the results of ab-initio calculations.

3.5 Conclusions

In this chapter we have described experimental techniques commonly used to obtain information on organic functionalized surfaces hybrid organic-inorganic perovskites. Different methods are used to measure quantitative structural and electronic properties or to have qualitative information on surface reconstruction and on the nature of adsorbates-surface bonds. In particular we have focused our attention on LEED and STM measures, usually adopted in experiments performed to investigate surfaces. Such measurements let to know the structure of surfaces (reconstruction, superlattice periodicity, chemical bond formation with adsorbates) at atomic scale. To have information on work function a very common technique is kelvin probe microscopy, which gives interesting results in the case of functionalized semiconductor surfaces. X-ray diffraction and adsorption measurements have been used to study thin films of organic-inorganic perovskites based on tin-halides, giving interesting results. In the followings, we discuss theoretical models which complement such results and give new insight in functionalized surfaces and hybrid perovskites investigation.

Chapter 4

Organic coverage of the silicon (001) surface

Silicon (Si) surfaces have been the subject of intensive investigations [5, 7, 8, 77]. The possibility of integration of current Si-based microelectronics within new, functional devices is believed as a breakthrough of the next years. The silicon (001) surface is particularly suitable to functionalization with organic molecules containing a double C–C bond [8, 7, 3, 5]. This is due to the particular surface reconstruction whose main feature is the formation of asymmetric (tilted) Si dimers [5, 77]. Indeed, the bonding nature of a Si dimer, though still debated, can at least formally be described in terms of a double Si–Si bond (in analogy with the double C–C bond found in alkenes). Nonetheless, at variance with the double C–C bond, the charge density associated to the π component of the bond is thought to be asymmetrically distributed over the two atoms. This results in tilted Si–Si dimers [5], in which the “second” (π) bond is much weaker than in organic molecules. The consequences of that are rather significant: the adsorption of organic molecules containing a double C–C bond can occur through a mechanism known as a [2+2] cycloaddition in organic chemistry [8, 7, 9]. The π bond in both the surface dimer and the organic molecule breaks, with the formation of two C–Si σ bonds. This reaction is known to occur even at room temperature, with relatively small activation barriers. The dimer buckling does play a relevant role in the adsorption process, as the same reaction is forbidden (with a huge activation barrier) between two double bonded C–C groups.

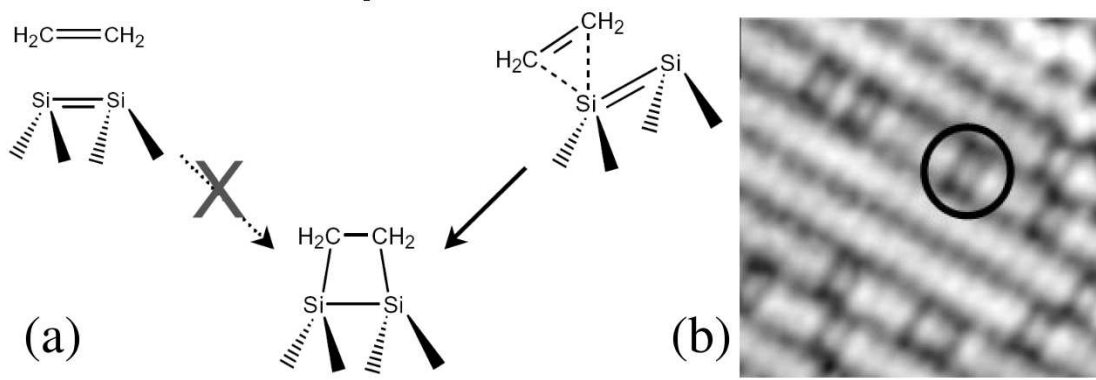


Figure 4.1: (a) A schematic of [2+2] cycloaddition is proposed. The tilted dimer configuration allows the cycloaddition reaction with the formation of Si-C σ -bonds. (b) The occupied-state STM image obtained by Wolkow et al. [2] clearly shows the ethylene adsorption (evidenced by a circle) along Si (001) dimer rows.

A schematic of the [2+2] cycloaddition reaction of ethylene on Si (001) surface is proposed in Fig. 4.1a. The occupied-state STM image obtained by Wolkow et al. [2] clearly shows the Si (001) surface reconstruction characterized by dimer rows formation. A circle evidences the ethylene adsorption through cycloaddition.

In this chapter, first-principles calculations of adsorbed organic layers on the silicon (001) surface are presented [10]. In particular we focus on the changes in the surface electron affinity induced by the coverage, by considering ethylene (C_2H_4) and a class of cyclopentene derivatives $C_5H_6-R_1R_2$ containing different functional groups, all anchoring to the surface through the same [2+2] cycloaddition mechanism. Because they all show similar bonding properties, any variation in the surface properties must be related with the functional group. The structural relaxation induced by the adsorption is discussed, elucidating the effect of both the adsorbate species and coverage. It turns out that different distortions occur in the molecular geometry, depending on both the species and the surface coverage, while molecule-to-surface bonding do show very similar features for all the considered molecules. We show that the presence of the adsorbate can modify the surface charge density, thus giving rise to an induced dipolar layer that modifies the electrostatic potential outside the surface. Such a dipole layer can in turn be related with surface **electron**

affinity and **work function** changes. A careful analysis of the dipole moment and of the electrostatic potential changes is carried out discussing the correlations with the properties of the isolated molecules. All the results indicate how the surface properties can be tuned through a suitable choice of the adsorbate. In sec. 4.1 the technical details on the performed calculations are summarized. The main concepts concerning electron energetics at semiconductor surface and semiconductor-adsorbate interface are outlined in secs. 4.1.1 and 4.1.2. These concepts are applied to the specific case of the adsorption of ethylene and a class of cyclopentene derivatives on the silicon (001) surface in sec. 4.2. Finally in sec. 4.3 some conclusions are drawn.

4.1 Details of the method

The calculations have been performed using a plane wave, pseudopotential method based on the density functional theory (DFT), as implemented in the Quantum-ESPRESSO package [78]. The Si atoms have been represented using a norm conserving pseudopotential, built within the Rabe-Rappe-Kaxiras-Joannopoulos scheme (RRKJ) [79]. In the case of C, N, H we have selected ultrasoft pseudopotentials constructed within the same RRKJ scheme. The Perdew-Burke-Ernzerhof (PBE) approximation for the exchange-correlation functional has been adopted [39]. The electronic wave functions have been expanded using plane waves corresponding to energies up to 30 Ry, while a 180 Ry cut-off energy has been used to represent the total charge density.

The $p(2\times 2)$ reconstructed clean silicon (001) surface is modelled as an extended slab, using a supercell containing 12 layers of silicon (Si), with 4 Si atoms per layer, and a vacuum region as thick as 14 Si atomic layers (19 Å). The surface in-plane crystal cell (assumed to be in the xy plane) was built using the optimized bulk Si lattice constant of 5.47 Å, that fairly matches the experimental result [80] of 5.43 Å. Full relaxation of all the atoms but those belonging to the two central Si layers was allowed. The optimized geometries are obtained using the Hellman-Feynman forces with the Broyden-Fletcher-Goldfarb-Shanno (BFGS) algorithm (mentioned in sec. 1.5) to minimize the total energy with respect to the atomic positions. The surface

Brillouin zone was sampled using a $(2 \times 2 \times 1)$ Monkhorst-Pack [81] k -point grid.

The adsorbed molecules were placed on both sides of the slab to ensure inversion symmetry, so minimizing the formation of artificial electric fields in the vacuum [82]. The same supercell as that used for the clean surface has also been used in all the calculations (with a minimum vacuum region thickness equivalent to 6 silicon atomic layers). No significant variations of the calculated properties were found on increasing the vacuum region.

The surface dipole moments induced by the molecules are investigated with a detailed analysis of both the charge density distribution and the electrostatic potential. Because we deal with a surface problem, planar averages on planes parallel to the surface are carried out for the main quantities of interest. For the evaluation of the variations of the electron affinity and ionization potential induced by surface adsorbates, the knowledge of the vacuum level is needed. The latter can be easily determined from the value of the averaged electrostatic potential far enough from the surface. However, the systematic comparison of the vacuum level in presence of different adsorbates needs an alignment procedure bringing the zero of the energy to the same value for all the considered systems. The one-dimensional planar average of the electrostatic potential shows microscopic oscillations that in our case almost perfectly reproduce a bulk-like behavior in the middle of the slab, as it will be shown in the following (the bulk potential was computed using the same surface supercell and the same number of Si atoms, after removing the vacuum region). To get rid of such oscillations, this potential can be further averaged on a “macroscopic” window, and the value of the new average at the center of the slab can be used for the alignment procedure (so as to match the bulk value). Therefore, the difference between the value of the macroscopically averaged potential at the center of the slab of a given (clean or covered) surface and that in bulk Si is computed. Finally, both the potential and the band structure of the given surface are shifted by this difference. It is worth pointing out that for the alignment procedure to be meaningful it is necessary that the center of the slab reproduces a common environment in all the cases. In the rest of the paper, the shown aligned potentials and band structures are meant to have been aligned according to what explained above.

The optimized geometry, total energy and charge density for the isolated molecules are calculated using a cubic supercell (with a side of nearly 16 Å). These quantities

allow to compute surface adsorption energies as well as induced dipole moments.

4.1.1 Electron affinity and ionization potential

The electron affinity (EA) at a semiconductor surface is the energy needed to carry an electron from the vacuum to the bottom of the conduction band (CBM). Similarly, the ionization potential (IP) is defined as the energy required to bring an electron from the maximum of the valence band (VBM) to the vacuum [83, 84, 85, 86]. The EA is calculated at DFT level as energy difference between the vacuum level (E_{vac}) and the Kohn-Sham (KS) eigenvalue relative to the bottom of the conduction band of the semiconductor bulk band structure: $\chi = E_{vac} - E_{CBM}$. In the same way, the IP is computed as $I = E_{vac} - E_{VBM}$, where E_{VBM} corresponds the top of the bulk valence band. While E_{VBM} and E_{CBM} are obtained from bulk band structure calculations, E_{vac} can be derived from a slab calculation, so that the energy references for these two systems could be in general different. This problem is nicely solved thanks to the alignment procedure previously described.

4.1.2 Vacuum level and surface dipole

The presence of adsorbates on a surface may induce, as already mentioned, changes in the vacuum level [87, 88]. Here we summarize the main concepts related with it. By symmetry, only the dipole component along the surface normal (assumed to be the z direction in the following) is responsible for the vacuum level modification. For the sake of simplicity, in the following planar averages will be given the same symbol of the corresponding functions.

Let $\rho(x, y, z) = \rho_{el}(x, y, z) + \rho_{ion}(x, y, z)$ be the total charge density of a given slab (ρ_{el} and ρ_{ion} give the electronic and ionic contribution to it, respectively). Its planar average can be defined as follows

$$\rho(z) = \frac{1}{A} \iint_A dx dy \rho(x, y, z) \quad (4.1)$$

where the integral is done on the surface unit cell and A is its area. An analogous definition can be given for the planar average $V(z)$ of the electrostatic potential $V(x, y, z)$.

The z component of the dipole moment per unit surface (in the following referred to as dipole moment density) can be related with the electrostatic potential using Eq. (4.1) and the Poisson's equation

$$p = \int_0^{c/2} dz z \rho(z) = -\frac{1}{4\pi} \cdot \int_0^{c/2} dz z \cdot \frac{1}{A} \iint_A dx dy \left[\frac{\partial^2 V}{\partial x^2} + \frac{\partial^2 V}{\partial y^2} + \frac{\partial^2 V}{\partial z^2} \right] \quad (4.2)$$

The integration extremes are $z = 0$ (center of the slab) and $z = c/2$ (at the middle of the vacuum region, see Fig. 4.3). On the right side, the terms containing the partial derivative of V with respect to x and y give a zero contribution to the integral. The remaining term can be integrated by part, giving

$$p = \frac{1}{4\pi} [V(c/2) - V(0)] \quad (4.3)$$

The vacuum level can be expressed as $E_{vac} = -eV(c/2) = -eV_{vac}$.

It will be useful to label with different apexes the quantities p and V for clean (p^{cl} , V^{cl}) and covered (p^{co} , V^{co}) surfaces respectively. By means of the alignment procedure previously depicted, at the center of the slab V^{co} and V^{cl} overlap reproducing the bulk oscillating potential, so that at the center of the slab we have $V^{co}(0) = V^{cl}(0)$. This is an important point because it shows that a variation of the surface dipole density $\Delta p = p^{co} - p^{cl}$ induced by the coverage induces in turn a proportional variation of the vacuum level energy $\Delta E = -e(V_{vac}^{co} - V_{vac}^{cl})$. Taking into account Eq. (4.3), it follows that

$$\Delta E = -4\pi e \Delta p \quad (4.4)$$

The EA and IP change by the same amount, since their variations are only due to the vacuum level changes. From now on, we will focus on EA and IP changes with respect to the clean surface. The EA and IP values, for each system, can be obtained by adding, to the corresponding variation ΔE the EA and IP of the clean surface, respectively. If we express the energy in Ry and the dipole density in a.u.⁻¹ (namely, define $\tilde{\chi} = \chi/(e^2/2a_B)$, $\tilde{p} = p \cdot a_B/e$, with a_B the Bohr radius), Eq. (4.4)

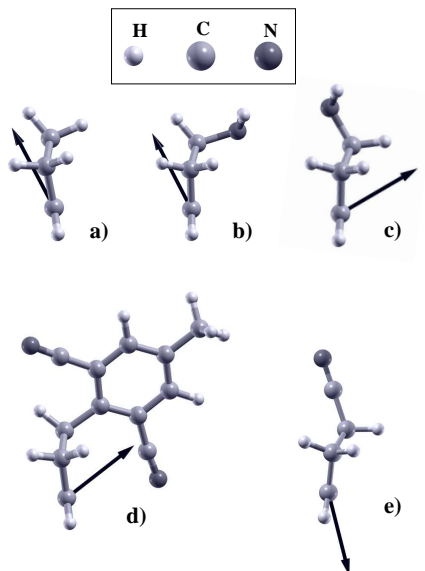


Figure 4.2: A ball-and-stick plot of the cyclic molecules $C_5H_6-R_1R_2$ investigated in this work, with $R_1=R_2=H$ (cyclopentene) (a), $R_1=H$, $R_2=NH_2$ (b), $R_1=NH_2$, $R_2=H$ (c), $R_1=C_9N_2H_5$, $R_2=H$ (d) and $R_1=H$, $R_2=CN$ (e). Black arrows indicate the direction of the dipole moment of the isolated molecule.

becomes (for the EA, the same applies to the IP)

$$\Delta\tilde{\chi} = -8\pi\Delta\tilde{p}. \quad (4.5)$$

Finally, it is worthwhile stressing that, with the conventions used here, a positive dipole is oriented outwards and causes a negative shift of the EA.

4.2 Results and Discussions

4.2.1 The isolated molecules

We consider ethylene and a class of cyclopentene derivatives $C_5H_6-R_1R_2$ shown in Fig. 4.2. For cyclopentene (Fig. 4.2a) $R_1=R_2=H$, while one of these two H atoms is replaced with a functional group in the other cases. It turns out that two nonequivalent configurations are obtained if a given functional group replaces either R_1 or

Table 4.1: The computed dipole moment of the isolated molecules.

	$ \mu $ (Debye)
C_2H_4	0.0
C_5H_8	0.270
$C_5H_6NH_2H$	1.368
$C_5H_6HNNH_2$	1.242
$C_5H_6C_9N_2H_5H$	3.316
C_5H_6HCN	4.247

R_2 . They will be referred to as the “axial” and “equatorial” configurations: for example Figs. 4.2b and 4.2c show a substitutional amino (NH_2) group in an axial and equatorial configuration, respectively. A bond to the ring atoms is termed axial or equatorial according to whether it makes a relatively large or small angle, respectively, with the plane containing or passing closest to a majority of the ring atoms. The five molecules shown in Fig. 4.2 correspond to (a) cyclopentene (C_5H_8), (b) axial-4-amino-cyclopentene ($C_5H_6NH_2H$), (c) equatorial-4-amino-cyclopentene ($C_5H_6HNNH_2$), (d) axial-4-(2,5-dicyano-toluene)-cyclopentene ($C_5H_6C_9N_2H_5H$) and (e) equatorial-4-cyano-cyclopentene (C_5H_6HCN). The total dipole moments computed for this set of molecules are reported in Table 4.1. Black arrows in Fig. 4.2 indicate the orientation of these dipole moments.

4.2.2 Silicon surfaces

(001)-(2x2) clean surface

As mentioned before, the $p(2 \times 2)$ reconstruction of the clean Si(001) surface leads to the formation of dimer rows, along which Si-Si dimers are alternately buckled (see Fig. 4.3). The calculated buckling angles [89] (about 19°) and dimer bond length (2.37 Å) are in a good agreement with the experimental results [90].

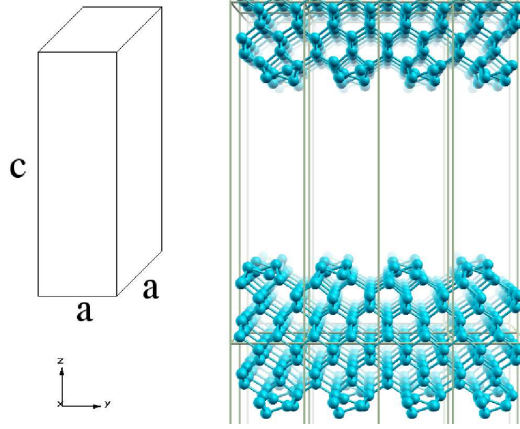


Figure 4.3: A perspective of the silicon (001) surface in the $p(2\times 2)$ reconstruction. Dimers are alternately buckled along the dimer rows. The slabs are periodically repeated by using an appropriate supercell (tetrahedral).

An interesting point coming from our calculations is that the buckling of the atomic layers is not limited to the dimers (considered as the first layer) formation. The buckling can be quantified as the difference Δz between the z coordinates of two neighbor Si atoms along the dimer direction (such atoms belong to the same layer in the unreconstructed surface). As shown in the left panel of Fig. 4.4, the dimer buckling ($\Delta z=0.76 \text{ \AA}$) is clearly the most relevant, but also the third and the fourth layers show a significant buckling ($\Delta z=0.27 \text{ \AA}$ and $\Delta z=0.20 \text{ \AA}$ respectively).

Concerning the electronic band structure, surface states lying in the bulk silicon band gap appear, associated with the dangling bonds originated by the $p(2\times 2)$ surface reconstruction. As indicated in Fig. 4.5(a), this surface states can be distinguished in π bonding (π_1, π_2) and π^* anti-bonding states (π_1^*, π_2^*). A qualitative agreement is found with other theoretical calculations of the silicon surface band structure [89].

The EA and IP which we compute for the clean surface are $\chi = 4.31 \text{ eV}$ and $I = 4.96 \text{ eV}$ respectively (at the GGA level of approximation). It is also possible to evaluate a range of variability for the work function $\phi = E_{vac} - E_{FL}$ defined as the energy difference between the vacuum and the Fermi level (FL). At variance with metals, the work function (WF) of a semiconducting material is not an intrinsic property [86] simply because the position of the Fermi energy in the forbidden

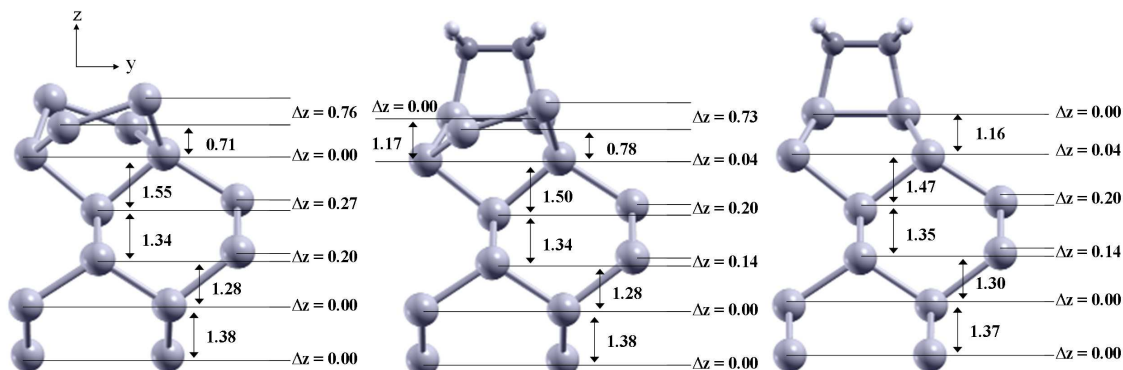


Figure 4.4: Optimized geometries for the clean silicon (001) surface, and the half and fully covered Si (001):C₂H₄. Both the buckling Δz and the inter-layer distances are given in Å.

energy gap depends on the experimental conditions (e.g. the doping). However, the presence of surface states in the band-gap region, as in the case of silicon, causes the well known Fermi Level pinning [49, 50, 91]. Our computed WF range is 4.93–5.11 eV, in very good agreement with other theoretical works [86]. To match theoretical values to experimental results one should use quasi-particle (QP) correction (e.g. GW many-body approximation [92]) to the computed KS eigenvalues. In Ref. [86] a fair agreement with experimental results [93, 94, 95, 96] for the WF is found using the GW corrected values.

(001)-(2x2):C₂H₄

The adsorption of ethylene on the Si(001) surface occurs through the [2+2] cycloaddition reaction. The relaxed geometries are computed for both half coverage, that is one molecule per dimer pair (or 0.5 monolayer) and full coverage, that is one molecule per dimer (or 1 monolayer). As already stated above, both the π component of C=C bond and the π -like component of the Si dimer bond break leading to the formation of two C–Si σ bonds. As such, the cycloaddition leads to the unbuckling ($\Delta z=0.00$ Å) of the involved dimer (see Fig. 4.4, central and right panels) without changes on the dimer bond length (the σ component of the bond is pre-

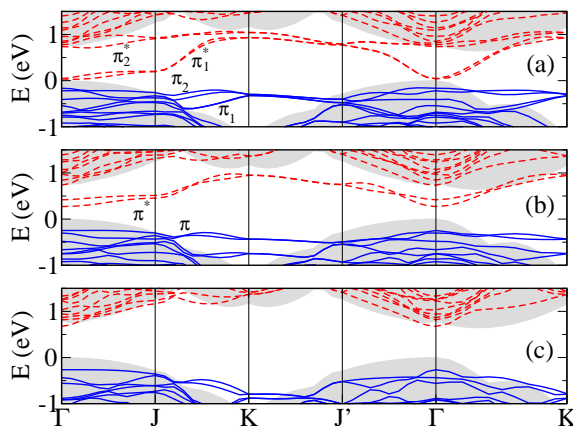


Figure 4.5: Surface band structure for the clean surface (a), half (b) and fully (c) covered Si(001):C₂H₄ surface. Filled and empty states are indicated with solid and dashed lines respectively. The shaded regions represent the projection of the bulk band structure in the two-dimensional surface Brillouin zone. The top of the bulk valence band is set to zero. The surface states π , π^* gradually disappear on increasing the coverage. The points J and J' are defined in the same way as in Ref. [89].

served [97]). The C–C bond length after adsorption is 1.56 Å, in good agreement with the experimental result [90] of 1.62 ± 0.08 Å. Moreover, the computed value is much closer to a C–C single bond than to a double one, as shown by the comparison between ethane (C₂H₆) and ethylene (C₂H₄). In the case of ethane, the C atoms are singly bonded with a bond length [98] of 1.535 Å and sp^3 hybridized with a $\angle CCH$ measured angle [98] of 111.17° in good agreement with the one (112.6°) we computed for the adsorbed ethylene. These results confirm the C–C double bond breaking and the sp^3 hybridization of the same C atoms as a consequence of the cycloaddition reaction.

With a 0.5 monolayer (ML) coverage, the layers buckling difference, with respect to the clean surface, is mainly restricted to the first layer, where the dimer involved in the cycloaddition gets unbuckled (see Fig. 4.4, central panel).

With full coverage, both dimers (per surface unit) are unbuckled. As clearly shown in Fig. 4.4 (right panel), a variation with respect to the clean surface is found on the third and the fourth layers (buckling of $\Delta z=0.20$ Å and $\Delta z=0.14$ Å respectively). A general trend towards the reduction of the buckling with the

coverage is observed and it is interesting to note that also the distance between the second and the third layers gradually decreases increasing the coverage, going from 1.55 Å (clean surface) to 1.47 Å (1 ML coverage).

Focusing on the electronic properties, the surface states (clearly related to the Si–Si dimer) are gradually removed as the coverage increases and disappear at full coverage, as shown by comparing the near-gap band structures in Fig. 4.5 (the shaded areas are projections of the bulk band structure in the two-dimensional surface Brillouin zone). The ethylene adsorption induces an EA change $\Delta\chi = -0.64$ eV for 0.5 ML and $\Delta\chi = -1.17$ eV for 1 ML coverage.

An interesting comparison with recent experimental data [99] can be done in the case of full coverage. In Ref. 34 a detailed study is reported on the adsorption of C_2H_4 on n doped Si (001) surface. From their data we can extract a value of the work function of 3.2 eV to be compared with our calculated value of 3.14 eV. Although the agreement is very good, it is necessary to detail the assumptions we have used for obtaining 3.14 eV. The first point is that at full coverage there are no surface states in the band gap, as shown in Fig. 4.5c. This means that at room temperature the Fermi level is, because of doping, just below the bottom of the conduction band. It is therefore reasonable to assume that in this particular case there is a negligible contribution from band bending so that work function and electron affinity are nearly the same. Our 3.14 eV is the difference between the vacuum level and the conduction band bottom.

There is another interesting observation to be made. The paper of Livneh et al. [100] discusses the results of measurements concerning work function variations during C_2H_4 adsorption on the Ru (001) surface. The point is that these authors have shown that the nature of C_2H_4 bonding on this metal is similar to the one discussed in this work, being the bonding due to an sp^3 hybridization. At full coverage they measure a work function variation of -1.31 eV. Now, if we take our full coverage $\Delta\chi=-1.17$ eV we see that there is some consistency between these values. If we consider that the ratio between the Si(001) surface unit cell area and that of the Ru (001) surface is roughly 1.19, our $\Delta\chi$ must be multiplied by 1.19 giving -1.39 eV which is very near to the experimental estimate of -1.31 eV. It appears from this simple estimate that provided the type of bonding on a surface does not change dramatically upon changing the material [101], the electron affinity varia-

Table 4.2: The Si–C bond length for the different adsorbates and coverages.

	Half coverage	Full coverage
C_2H_4	1.955	1.959
C_5H_8	1.960	1.976
$C_5H_6NH_2H$	1.957	1.973
$C_5H_6H_2NH$	1.962	1.970
$C_5H_6C_9N_2H_5H$	1.966	–
C_5H_6HCN	1.964	1.970

tions are, somehow, a transferable properties. However, a more clear assessment of this interesting point would require specific calculations.

(001)-(2x2): C_5H_6 - R_1R_2

A question arises on whether the bonding properties (bond lengths and angles) are the same or not for different molecular adsorbates, all anchoring to the surface through the same mechanism.

In Table 4.2 we report the computed Si–C bond length for the different adsorbates and at both half and full coverage. It is seen that a significant dependence on the adsorbate species is not found. Only a small increase of the bond length with coverage can, in fact, be observed. Similarly, dimer buckling and inter-layer distance do not show appreciable differences with respect to the ethylene case (see Fig. 4.4).

Concerning the electronic properties, no signature in the mid-gap region can be detected [102] due to the adsorption of this class of molecules (as clearly shown in Fig. 4.6 in the case of half coverage). Only low-lying electronic bands depend on the adsorbate, in agreement with some experimental results [103].

In Fig. 4.7 we show the averaged electrostatic energy for a 0.5 ML coverage of the different considered surface-adsorbate complexes. Bulk-like oscillations (independent of the adsorbate species) can be observed in the middle of the slab ($z = 0$)

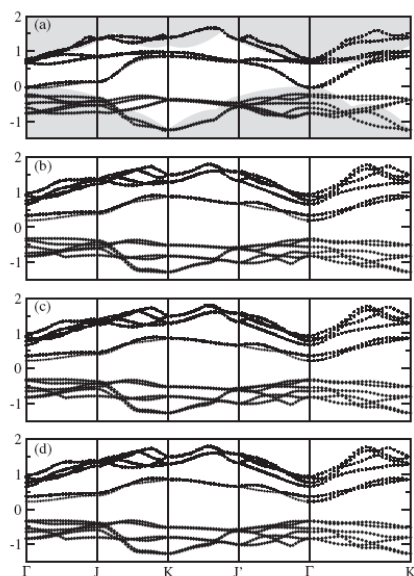


Figure 4.6: Surface band structure for (a) clean, (b) C_2H_4 , (c) C_5H_8 and (d) $\text{C}_5\text{H}_6\text{HNH}_2$ covered silicon (001) surface at 0.5 ML. The shaded area in (a) is a projection of the bulk silicon band structure within the surface Brillouin zone. The reference energy is the top valence band of bulk silicon. Bold circles and crosses correspond to occupied and unoccupied bands respectively [102].

in all the cases. More interestingly, the shift in the vacuum level position with respect to the clean surface is clearly visible. From this shift we compute $\Delta\chi$ for all the adsorbates and coverages, as summarized in the first column of Table 4.3.

From both Fig. 4.7 and the corresponding values listed in Table 4.3 it emerges very clearly the possibility of tuning the organic-semiconductor interface as far as the transfer of electrons is concerned.

Cycloaddition involving cyclic alkenes causes a complex structural deformation. In order to study these effects in a systematic way, we introduce the buckling angles φ_1 , φ_2 and φ_3 as shown in Fig. 4.8.

The C–C and Si–Si bonds involved in the cycloaddition nearly lie in the same plane (except for $\text{C}_5\text{H}_6\text{C}_9\text{N}_2\text{H}_5\text{H}$) so that the two Si–C bonds per molecule show nearly the same buckling angle φ_1 , suggesting to use the average value as a deformation parameter. For the same reason the φ_2 and φ_3 averages are considered.

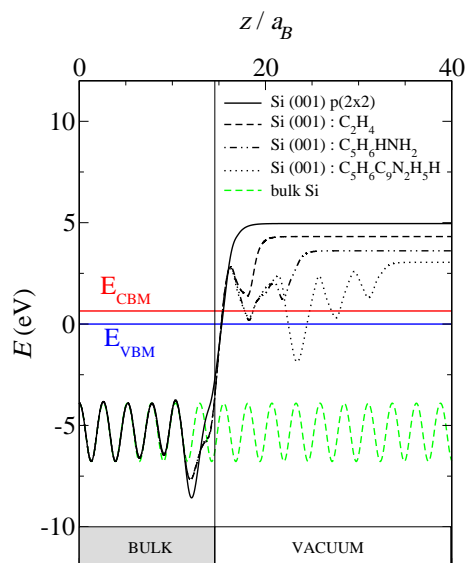


Figure 4.7: The planar average of the electrostatic potential for bulk Si, clean and (half) covered silicon (001) surface. Bulk-like oscillations, independent of the adsorbed molecule, are obtained in the middle of the slab. E_{VBM} and E_{CBM} represent the top of the bulk valence band and the bottom of the bulk conduction band respectively.

The molecule reconstruction due to the adsorption can be viewed as a two steps effect, that is, the orientation of the molecule with respect to the surface and the deformation of the cyclic alkene structure. The former is related to φ_2 , the latter to φ_3 .

In Fig. 4.9, a front (upper panels) and side (lower panels) view of the C_5H_6HCN molecule is shown in the isolated (a) and adsorbed (0.5 ML) (b) configuration. A simple scheme of the cyclic alkene structure is also represented in Fig. 4.9c, for clarity. For a more direct comparison, the isolated molecules have been oriented so as to have the C_c-C_c bond (see Fig. 4.9c) oriented along the $[1\bar{1}0]$ direction and the same φ_2 as the adsorbed molecule. Different values of φ_3 for the isolated (φ_3^{iso}) and the adsorbed (φ_3^{ads}) configuration clearly show the deformation of the cyclic alkene structure after adsorption.

In the case of 0.5 ML, because the mutual distances between neighbor molecules are large (exception made for $C_5H_6C_9N_2H_5H$), all the molecules undergo approximately the same deformation, as shown in Table 4.4. It means that the deformation

Table 4.3: Calculated EA variation $\Delta\chi$ (eV) and total surface dipole moment density variation Δp (units: $10^{-3} a_B/e$) with respect to the clean surface. The various contributions to Δp are reported (see Eq. (4.8)). The last column is the adsorption energy (in eV), defined as in Eq. (4.10). Different adsorbates and both half and full coverage are considered.

	$\Delta\chi$	Δp	p_a	Δp_b	Δp_s	E_{ads}
Half coverage						
C_2H_4	-0.642	1.878	2.113	-0.249	0.014	-1.794
C_5H_8	-0.834	2.440	2.488	-0.049	0.001	-1.534
$C_5H_6NH_2H$	-1.204	3.523	3.620	-0.104	0.008	-1.546
$C_5H_6HNH_2$	-1.344	3.930	3.941	-0.021	0.010	-1.501
C_5H_6HCN	0.114	-0.331	-0.214	-0.124	0.006	-1.534
$C_5H_6C_9N_2H_5H$	-1.912	5.592	5.736	-0.143	0.001	-1.441
Full coverage						
C_2H_4	-1.165	3.409	3.546	-0.573	0.436	-1.770
C_5H_8	-1.394	4.078	4.236	-0.593	0.435	-0.935
$C_5H_6NH_2H$	-1.706	4.991	5.150	-0.593	0.435	-0.957
$C_5H_6HNH_2$	-1.828	5.346	5.673	-0.761	0.434	-1.039
C_5H_6HCN	1.826	-5.344	-4.634	-1.149	0.440	-0.853

of the cyclic structure is only related with the cycloaddition reaction, while the role of the functional group can be ruled out in this case.

As shown by a comparison between Figs. 4.9a and 4.9b, the sp^3 hybridization of the C_c atoms leads to a new orientation of the C_c-H bonds. The C_c-C_c double bond breaking causes a significant variation of the C_c-C_c bond length and, as a consequence, a not negligible modification of the cyclic alkene structure. In fact, the variations of the H atoms mutual distances are due to the rotation of the sp^3 structure of C_b valence orbitals with respect to the isolated configuration. The

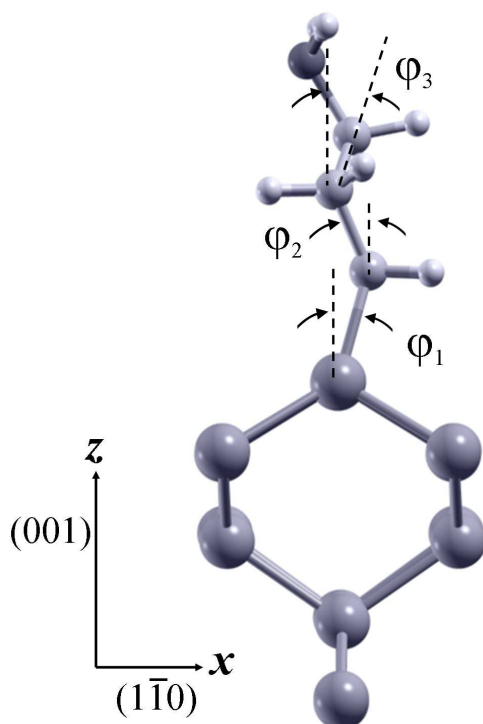


Figure 4.8: Buckling angles φ_1 , φ_2 and φ_3 , defined as angles between the projection of the corresponding bond on the $(1\bar{1}0)$ plane (the xz plane in our case) and the (001) direction (the z axis).

reorientation of the C_b-C_a bonds corresponds to a rigid rotation of the $C_a-R_1R_2$ structure, as shown by comparing Figs. 4.9a and 4.9b for C_5H_6HCN .

In the case of 1 ML coverage, the mutual repulsion between neighbor molecules results on functional groups pointing outwards with respect to the surface. For example, in the case of the amino-cyclopentene shown in Fig. 4.10, the equatorial and axial configurations show different values of φ_3^{ads} (see also table 4.4), but the functional group is found at the same distance from the surface. This means that, on increasing the coverage, the cyclic alkene deformation becomes strongly dependent on functional group position (equatorial or axial). We can conclude this analysis by observing that the structural change due to cycloaddition is not limited to the atoms directly involved in the reaction. In this sense we can speak of a non-local structural

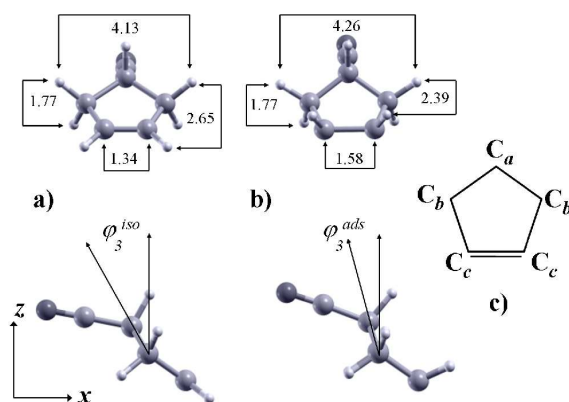


Figure 4.9: Front (upper panels) and side (lower panels) view of C_5H_6HCN in the isolated (a) and adsorbed (0.5 ML) (b) configuration. A simple scheme of the cyclic structure is also shown for clarity.

effects upon the molecule due to the cycloaddition reaction. Concerning the buckling of the silicon layers, no significant variation is obtained (at a fixed coverage) for all the adsorbates with respect to the case of C_2H_4 , so that the surface deformation due to adsorption is only connected to the type of reaction (the cycloaddition leads to the unbuckling of the Si–Si dimer) and the coverage.

4.2.3 Surface dipole analysis

We have already shown that the functionalization of the surface produces an EA variation directly proportional to the surface dipole moment density variation Δp . The numerical values of $\Delta \tilde{p}$ (as calculated from Eq. (4.2)) and $\Delta \tilde{\chi}$ (as calculated as variation of the vacuum level, see Fig. 4.7) for all the cases studied are close to a solid line with a slope of 8π as expected from Eq. (4.5) and as shown in Fig. 4.11.

A closer inspection to the dipole layer induced by the adsorbate can be achieved if the different contributions to Δp are separated. The chemisorption process induces two main effects: a structural deformation of both the surface and the adsorbing molecule as discussed above, and a charge transfer following the formation of the chemical bond. The two processes cannot be abstracted in reality, but an hypothetical two-step experiment can be simulated in the calculation. For a given surface-

Table 4.4: Buckling angles (in degrees, see Fig. 4.8 for their definition) for different adsorbed species at both 0.5 and 1 ML coverage.

	φ_1	φ_2	φ_3^{ads}	φ_3^{iso}
Half coverage				
C_5H_8	-2	52	13	31
$C_5H_6NH_2H$	-4	50	10	33
$C_5H_6HNH_2$	-2	54	16	33
C_5H_6HCN	-1	55	18	31
Full coverage				
C_5H_8	-14	27	27	6
$C_5H_6NH_2H$	-13	28	28	2
$C_5H_6HNH_2$	-15	23	-19	11
C_5H_6HCN	-14	24	-15	0

adsorbate system, we first compute the equilibrium relaxed geometry. Next, all the Si atoms are removed from the supercell and the total (ionic + electronic) charge density ρ_a of the isolated adsorbate layer is self-consistently computed. Finally, the adsorbate layer is removed from the supercell and the charge density ρ'_s of the silicon surface computed. This allows to get rid of charge density variations induced by relaxation, thus abstracting only the contribution coming from the formation of the chemical bonds [88, 104]. In fact, the difference defined as $\Delta\rho_b = \rho - (\rho_a + \rho'_s)$ is nothing else than the electron density redistribution due to the surface-molecule bond formation. The corresponding induced dipole density is:

$$\Delta p_b = \int_0^{c/2} dz z \Delta\rho_b(z). \quad (4.6)$$

By indicating with ρ_s the charge density of the clean surface, the total surface

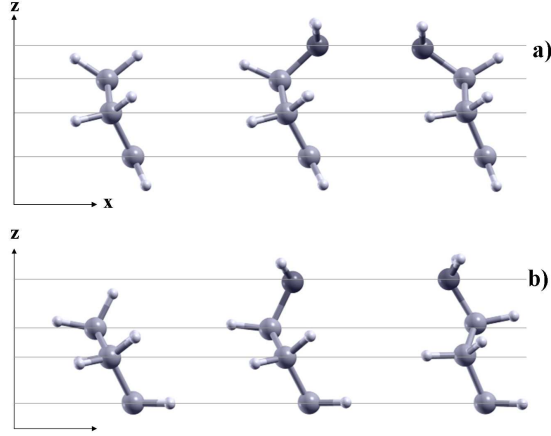


Figure 4.10: Side view of C_5H_8 (left panels), $C_5H_6NH_2H$ (central panels) and $C_5H_6HNH_2$ (right panels) in the isolated (a) and adsorbed (b) configuration at 1 ML coverage.

dipole variation (with respect to the clean surface) can be rewritten as follows

$$\begin{aligned} \Delta p &= \int_0^{c/2} dz z(\rho - \rho_s) = \int_0^{c/2} dz z(\rho - \rho_a - \rho'_s) + \\ &+ \int_0^{c/2} dz z(\rho'_s - \rho_s) + \int_0^{c/2} dz z\rho_a = \Delta p_b + \Delta p_s + p_a \end{aligned} \quad (4.7)$$

so that Eq. (4.5) becomes

$$\Delta \tilde{\chi} = -8\pi(\Delta \tilde{p}_b + \Delta \tilde{p}_s + \tilde{p}_a) \quad (4.8)$$

With this procedure the total surface dipole moment density variation Δp can be viewed as made from the sum of three different contributions: $\Delta p_s = p'_s - p_s$ which is the variation of the surface dipole moment density due to the surface structural relaxation; Δp_b , the induced dipole moment density due to the formation of the chemical bond; p_a , the projection on the z axis of the dipole moment of the molecule in the adsorbed configuration, divided by the surface unit cell area. The computed values are reported in Table 4.3 for half and full coverage. The data listed in this table may be complemented with the cumulative sum of Δp_b defined as

$$\overline{\Delta p_b}(z) = \int_0^z dz' z' \Delta \rho_b(z') \quad (4.9)$$

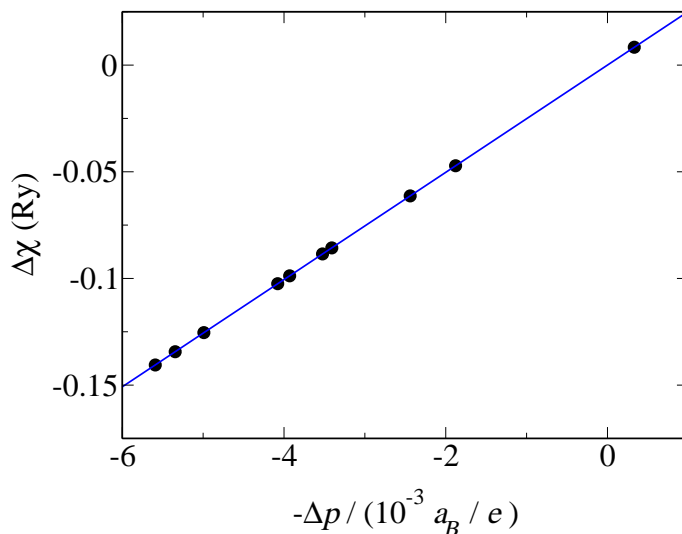


Figure 4.11: EA variation as a function of the surface dipole change due to the adsorption of the different molecules. Both coverages are represented.

and shown in Fig. 4.12 for different adsorbates at 0.5 ML coverage. It is evident that $\overline{\Delta p_b(c/2)} = \Delta p_b$.

Fig. 4.12 nicely shows that the variations of the dipole density associated with the formation of the chemical bond at and around the Si–C bonding sites are very similar for all the molecules considered. This is consistent with the very small differences in the Si–C bond length for different adsorbates shown in Table 4.2. From Table 4.3 it can be seen that the contribution of Δp_s is negligible at 0.5 ML, while it becomes comparable and opposite to Δp_b at 1 ML coverage. In any case, the main contribution to the total surface dipole variation Δp is represented by p_a .

In the last column of Table 4.3 we report the adsorption energies for the different molecules at both half and full coverage. Such energy is defined as

$$E_{ads} = [E - (E_S + E_m)]/2n \quad (4.10)$$

where E is the total energy of the surface/molecule complex, E_S is the total energy of the $p(2 \times 2)$ reconstructed Si(001) surface, E_m is total energy of the isolated molecule. Both E and E_S are referred to a 2×2 surface unit cell containing n molecules (1 or 2 for half and full coverage, respectively) and the factor 2 takes into account the fact that molecules are adsorbed on both sides of the slab. It turns out that, at a fixed

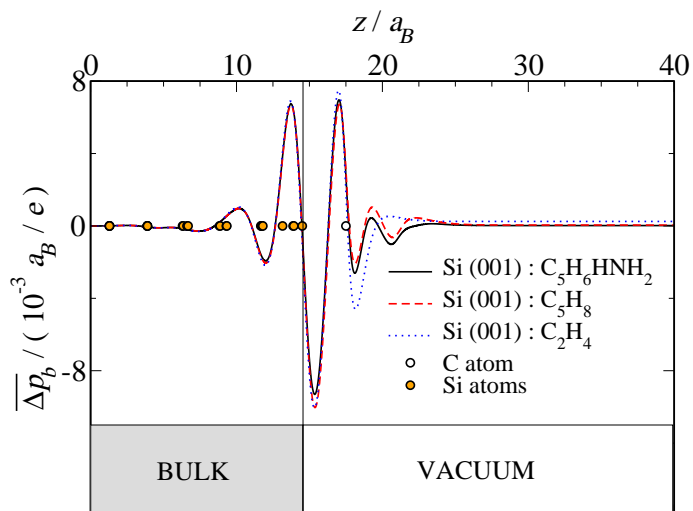


Figure 4.12: Cumulative sum of Δp_b (see Eq. (4.9)) at 0.5 ML coverage for C_2H_4 , C_5H_8 and $C_5H_6HNH_2$.

coverage, the mutual repulsion of neighbour molecules results in less stable structures for the surface/adsorbate complexes with the larger molecules. For the same reason, full coverage results in higher adsorption energies, with negligible difference only in the case of ethylene. No apparent correlation is found between adsorption energies and molecule dipole moments.

4.2.4 Can we correlate EA variation to isolated molecule dipole moment?

In the previous section we have seen that the main contribution to the surface dipole comes from p_a , defined as the z component of the dipole moment density of a molecular “layer” obtained by removing all the Si atoms from the supercell. In Fig. 4.13 we show the variations of electron affinity $\Delta\chi$ as a function of $-p_a$ for both (a) half coverage and (b) full coverage. Both the data point calculated from the electrostatic potential analysis (see table 4.3) and the theoretical straight line (calculated from Eq. (4.5)), are reported. The main finding is that Eq. (4.5) is able to fit the calculated $\Delta\chi$ even if, at variance with Fig. 4.11, the p_a component of the dipole moment density is used, rather than its total variation Δp . This confirms

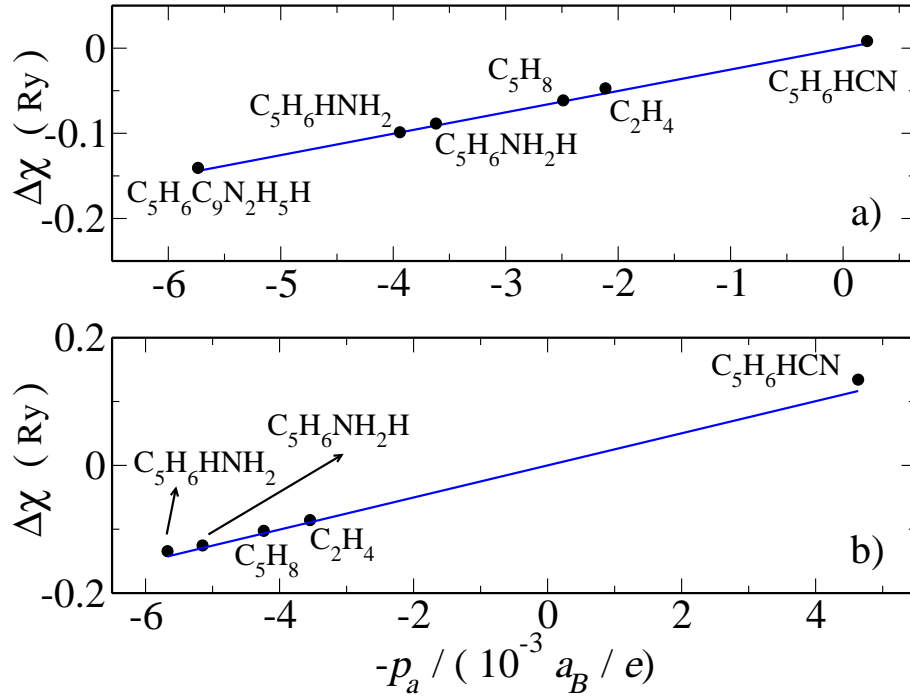


Figure 4.13: EA variation as a function of the projection of the dipole moment along the z axis (divided by the surface area) of the molecules in the adsorbed configuration at 0.5 ML (a) and at 1ML (b) coverage.

that the main contribution to $\Delta\chi$ comes from p_a .

In designing a particular interface it may be important to know in advance whether or not we can estimate the EA variations from the knowledge of the properties of the isolated molecule (dipole moment, in this case).

We can calculate P_{is} , the z -component of the dipole moment of the isolated molecule, after rotating each molecule, so as to have the same φ_2 buckling angle of the adsorbate, as previously depicted. In Fig. 4.14 we plot P_{is} versus $P_a = A \cdot p_a$, where P_a is calculated at 0.5 ML coverage (both P_{is} and P_a are dipole moments rather than dipole moment densities). The straight line is a linear regression of the plotted points. It is seen that an evident correlation between the two dipole moments cannot be found. Combined with the results of Figs. 4.11 and 4.13, this shows that the nice agreement with Eq. (4.5) is lost if one constructs a plot using the the dipole moment (or its z -component) of the isolated molecule. This supports our

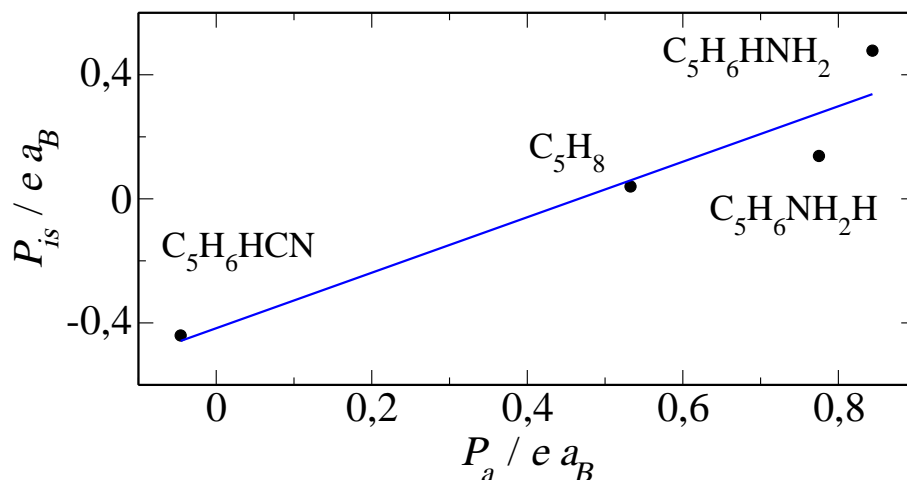


Figure 4.14: The projection of the dipole moment along the z axis for adsorbed (P_a) and isolated (P_{is}) configurations. It should be noted that in this figure P_a and P_{is} are the dipole moments rather than the dipole moment densities.

picture of “non-linear” effects induced by the surface molecule bonding, associated with a significant geometrical deformation of the molecules.

Indeed, the adsorption induces a change in the hybridization of the two C_c atoms (see Fig. 4.9) from sp^2 to sp^3 . The sp^3 orbitals show similar orientations for all the studied molecules (ethylene and cyclopentene derivatives) but this does not result in similar variations of the molecule dipole moment. As shown in Fig. 4.2, the dipole orientation strongly depends on the functional group and its position with respect to the molecule (equatorial or axial). As a result, similar changes and reorientations of the C_c sp^3 orbitals can cause different re-orientation of the functional group and, in principle, different dipole moment variations.

We conclude by observing that “non-linearity” in dipole moment variations could also be associated with depolarization effects. Simply because these are polarizable molecules, the dipole moment of the molecular layer P_a can be different from that of the isolated molecule even in absence of any geometrical reorganization. To get rid of such effects, we can related P_a with P_{is} through

$$\begin{aligned}
 P_a/n &= (P_a/n - P_a^{is}) + (P_a^{is} - P_{is}) + P_{is} \\
 &= \Delta P_a^{depol} + \Delta P_a^{relax} + P_{is}
 \end{aligned}
 \tag{4.11}$$

Table 4.5: Dipole moment per molecule of the molecular slab (P_a/n , with $n = 1$ or $n = 2$ for 0.5ML and 1ML coverage, respectively) and of the isolated molecule (P_a^{is}) calculated with the geometry of the molecular adsorbate. The difference between the second and the first column is the depolarization contribution ΔP_a^{depol} (see text). The dipole moments are in units of $e \cdot a_B$.

	P_a/n	P_a^{is}	$-\Delta P_a^{depol} / P_a^{is}$
Half coverage			
<chem>C2H4</chem>	0.452	0.492	0.08
<chem>C5H8</chem>	0.533	0.633	0.16
<chem>C5H6NH2H</chem>	0.775	0.932	0.17
<chem>C5H6HNH2</chem>	0.844	1.020	0.17
<chem>C5H6HCN</chem>	-0.046	-0.070	0.34
<chem>C5H6C9N2H5H</chem>	1.228	1.819	0.32
Full coverage			
<chem>C2H4</chem>	0.380	0.499	0.24
<chem>C5H8</chem>	0.453	0.649	0.30
<chem>C5H6NH2H</chem>	0.551	0.731	0.25
<chem>C5H6HNH2</chem>	0.607	0.793	0.23
<chem>C5H6HCN</chem>	-0.496	-0.853	0.42

where the subscript a is always referred to the geometry of the adsorbed molecule. Here, P_a^{is} is the dipole moment of an isolated molecule (so no depolarization effects are included) having this geometry, whereas $\Delta P_a^{depol} = P_a - P_a^{is}$, $\Delta P_a^{relax} = P_a^{is} - P_{is}$. Therefore, depolarization (ΔP_a^{depol}) and relaxation (ΔP_a^{relax}) effects have been separated out. If ΔP_a^{depol} is not zero, the coverage induces molecule-molecule interactions that modify its dipole moment even if no relaxation effects would take place. In table 4.5 we show the dipole moment variations associated with depolarization effects.

It turns out that depolarization effects may determine changes in the isolated

molecule dipole moment from 8% to about 40%. Such changes are larger for full coverage. Nonetheless, a plot of ΔP_a^{depol} versus P_a/n shows linear correlation between the two. Therefore, the previous conclusion that it is not possible to correlate the changes in the electron affinity with the dipole moment of the isolated molecule should be attributed to (non-linear) effects induced by distortion, namely, ΔP_a^{relax} , rather than polarization effects.

4.3 Conclusions

In this chapter we have given a detailed description of the formation of a dipole layer due to the adsorption of ethylene and of a class of organic molecules with the general formula $C_5H_6-R_1R_2$ where R_1 and R_2 are functional groups controlling the molecular dipole moments. We have seen that although these molecules adsorb on the silicon (001) surface through the same mechanism, both the silicon substrate and the molecule geometry have a reconstruction which depends on both the molecule type and the coverage. These reconstructions induce a significant variation in the surface dipole moment which results in a corresponding variation of the electron affinity. A detailed analysis of the various contributions to the surface dipole have revealed that the common practise of linking the electron affinity variations directly to the dipole moment of the isolated molecule is, as a rule, not always correct. The exception to this rule is when a molecule, after adsorption, does not change its geometry. A particular interesting case is that of the benzoic acids with different para-substituents that control the dipole moment. Measurements of the electron affinity do show a clear linear relation with the dipole of the isolated molecule and this is due to the fact the bonding to the surface does not corrupt the benzene ring [105, 106, 107]. In other words, while the cycloaddition reaction with the molecules considered in this work gives rise to a reconstruction which changes the geometry and the orientation of the molecule, it is likely that this does not occur with the benzoic acids.

Chapter 5

Hybrid organic-inorganic perovskites based on tin-halides

Hybrid organic-inorganic composites are an emerging class of new materials that hold significant promise. These complex structures, based on a molecular scale composite of organic and inorganic components, represent the possibility of combining properties of organic and inorganic elements in a unique material. Inorganic compounds, typically characterized by covalent and ionic interactions, provide a wide range of electronic properties: high electrical mobility, wide range of band gaps (designing insulators, semiconductors, metals), interesting magnetic and dielectric properties, thermal stability, mechanical hardness. Organic compounds, which typically interact through weaker interactions (van der Waals or hydrogen bonding) offer the potential of high luminescence efficiency, large polarizability, plastic mechanical properties, and in some case exhibit conducting properties. The fields of application of this branch of materials are as varied as the materials themselves. Hybrid organic-inorganic compounds are considered as innovative advanced materials, and promising applications are expected in many fields, including optics, electronics, mechanics, protective coatings, catalysis, sensors, biology, and others [11, 12, 13, 14, 15, 16, 17, 18, 19, 20, 21, 22, 23, 24, 25, 26, 27, 28]. Tuning the electronic structure of materials at nanometer length scale can lead to unique electronic and optical properties in hybrid materials that are not typical of the organic and inorganic components alone. This is the case of layered organic-inorganic het-

erostructure, that can be prepared to form modulated electronic structures like multiple quantum well (MQW) structures [20]. In particular, hybrid organic-inorganic multilayers realizing staggered [20, 25] (or type II) MQW structures are of growing interest for their potential practical applications in electronic devices such as light-emitting diodes and photovoltaics [21, 22, 23, 24, 25, 26, 27, 28]. The main working principle can be described as follows. Typically, electrons and holes are photogenerated in the organic layers, which absorb light in the visible region. The inorganic layers are selected to have: high electron mobility, larger band gap and larger electron affinity (with respect to the organic one). Electrons and holes are thus separated at the organic/inorganic interface: electrons transfer to the inorganic conduction band due to the larger electron affinity, the high electron mobility reduces the recombination probability, producing high photoconductivity gain [25]. This is just an example of the wide range of opportunities offered by hybrid materials by modulating considerably their electronic structure.

A particular class of organic-inorganic materials are the hybrid perovskite compounds based on metal-halides [14]. The basic building component of the organic-inorganic perovskites is the ABX_3 perovskite structure. This simple structure consists of a network of corner-sharing BX_6 octahedra, where the B atom is a metal cation (typically Sn^{2+} or Pb^{2+}) and X is a monovalent anion (typically Cl^- , Br^- , I^-); the A cation is selected to neutralize the total charge, and it can be even a molecule. In this case, the organic cation must fit into a rigid and relatively small cuboctahedral hole formed by the 12 nearest X atoms, thus limiting the selection on the molecule in function of its dimension. In fact, a tolerance factor t can be defined by the relation $(R_A + R_X) = t\sqrt{2}(R_B + R_X)$, where R_A , R_B and R_X are the ionic radii of the corresponding elements: by changing R_A (that is the molecule dimension) the tolerance factor t can be varied, but only in a restricted range of values around the unity ($t = 1$ corresponds to a perfectly packed perovskite structure) to have a stable, even distorted, 3D perovskite structure [32]. By a suitable choice of both the inorganic cage (that is the B and X elements forming the BX_6 octahedra) and the cation, the structural and electronic properties can be tuned as desired [33]. Perovskite based hybrids can be synthesized with simple and cheap techniques thanks to their self-assembling character [29]. Moreover, organic-inorganic superlattices can be easily obtained by altering the combination of the

organic and inorganic components in the starting solution from which the hybrids are crystallized: the electronic properties of the inorganic compound can be tuned as a function of the dimensionality, realizing inorganic layers (2D systems) or multilayers, as well as inorganic chains (1D) and dots (0D) embedded in an organic matrix [18, 30, 31]. For example, Mitzi et al. demonstrated that layered perovskites of the type $[\text{NH}_2\text{C}(\text{I})=\text{NH}_2]_2(\text{CH}_3\text{NH}_3)_m\text{Sn}_m\text{I}_{3m+2}$ can be prepared to realize 1D ($m = 1$), 2D ($m = 2$) or multilayer ($m > 2$) inorganic structures, thus tuning the conductivity of the hybrid compound [18, 31]. For all these reasons and more, the metal (in particular lead and tin) halides hybrid perovskites have been extensively studied in the last 20 years [33, 108, 109, 110, 111, 112, 113, 114, 115, 116, 117, 118, 119, 120, 121, 122, 123, 124, 35, 125, 126, 127, 128, 129, 130, 131, 132, 133, 134, 135, 136]. In this framework, ab-initio investigations can shed light on the correlations between structure, chemical composition and properties. The ability of reproducing the structural and electronic properties and understanding their correlation with each element of the compound, offers the potential for designing new functional structures, with desired characteristics.

Our attention has been addressed to ASnX_3 perovskites. Typically, the ASnX_3 compounds have distorted tin environments in the low-temperature phase due to the presence of stereochemically active lone-pair of electrons on tin [34]. In practice, it is found that, by decreasing the electronegativity of the ligand halogen X, the distortion of the octahedra is significantly reduced. In the LCAO model, the general structural observation is rationalized by the simple concept of “orbital energy matching” between the appropriate halogen group orbital and the tin bonding orbital: the latter rises from an opportune combination of 5s and 5p tin orbitals as to match the the energy of the halogen np orbital. By changing the halogen, different mixture of 5s and 5p orbitals occurs, so varying the bonds directionality or equivalently the SnX_6 octahedra distorsion [34]. Moreover, many of ASnX_3 compounds have an undistorted perovskite structure in the high-temperature phase: such a structural transition may vary significantly the electronic properties. Furthermore, the structural and electronic properties may strongly depend on the choice of the cation [33, 35]. In this chapter, first-principles calculations of ASnX_3 crystals with $\text{A}=[\text{Cs}, \text{CH}_3\text{NH}_3 \text{ (methylammonium)}, \text{NH}_2\text{CH}=\text{NH}_2 \text{ (formamidinium)}]$ and $\text{X}=[\text{Cl}, \text{I}]$ are presented: the structural and electronic properties of these com-

pounds are analyzed and related to the particular choice of the halogen X, and of the cation A embedded in the corner-sharing BX_6 octahedra network. Different phases of $CsSnX_3$ compounds are considered, focusing on the relation between the choice of the halogen, the structural deformations occurring in the low-temperature phase due to octahedra distortions, and the optical and electronic properties variation due to the phase transition from high-temperature to low-temperature phases. Moreover, a comparison between hybrid and inorganic perovskites is made by changing the inorganic cation Cs with an organic molecule, evidencing the effects of the molecule to the structural and electronic properties of the compound. Finally, by varying the molecule, it is also stressed the possibility of tuning the volume of the cubic inorganic cage embedding the organic cation, with consequences in the electronic structure of the hybrid compound.

5.1 Details of the method

We have performed ab-initio calculations in the framework of density functional theory (DFT), as implemented in the Quantum-ESPRESSO (QE) package [78], based on a plane-wave basis set for the expansion of the single-particle Kohn-Sham wave functions, and pseudopotentials to describe the computationally expensive electron interaction. Vanderbilt-type ultrasoft pseudopotentials [42] have been used to represent all atoms Iodine (I) and Cesium (Cs), for which a Troullier-Martin [137] norm-conserving pseudopotential has been selected. The generalized gradient approximation (GGA) was employed for the evaluation of the exchange-correlation energy. The electronic wave functions have been expanded using plane waves corresponding to energies up to 30 Ry, while a 180 Ry cut-off energy has been used to represent the total charge density. A $4 \times 4 \times 4$ Monkhorst-Pack grid [81] has been chosen for sampling the Brilluoin zone. Full relaxation of the atomic positions within the unit cell is allowed following the Broyden-Fletcher-Goldfarb-Shanno (BFGS) algorithm. For all the considered structures the theoretical optimal lattice parameters have been estimated.

In the case of this films of $CH_3NH_3SnX_3$ ($X=Cl, Br$), to give a better estimation of the band gap, we have calculated GW many-body corrections [92] to

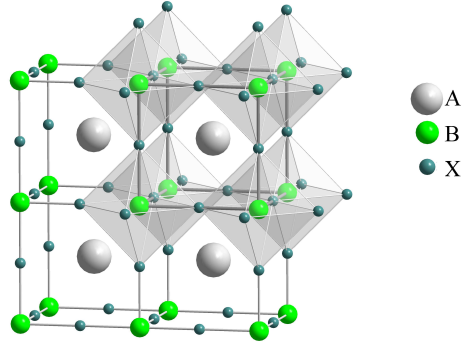


Figure 5.1: Basic ABX_3 perovskite structure. The BX_6 corner-sharing octahedra are evidenced.

the DFT-GGA energy gaps at the optimized geometries using the ABINIT code [138]. In this case, Troullier-Martin [137] norm-conserving pseudopotentials have been used to represent the atomic nuclei with the Perdew-Burke-Ernzerhof (GGA-PBE) parametrization [39] for the exchange-correlation energy with a plane-wave basis set cut-off energy of 100 Ry.

5.2 Results and Discussions

$ASnX_3$ crystals exhibit a cubic perovskite structure in the highest temperature phase. Fig. 5.1 shows the basic unit, which consists of corner-linked octahedra of X anions, with B cation at their center and A cation between them. As it has been observed in most of the inorganic perovskitic structures [139], by lowering the temperature $ASnX_3$ exhibit phase transitions characterized by: i) the deformation (typically referred to as distortion) of the octahedra, ii) the displacement of the inorganic A cation, iii) the tilting of the octahedra corner-sharing network, or iv) both of them. In the $CsSnX_3$ inorganic perovskites, the changes of electronic properties (electronic conductivity, optical absorption) resulting from phase transitions,

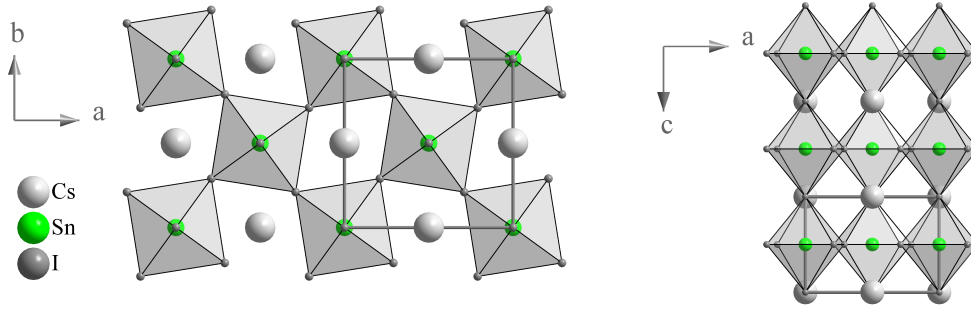


Figure 5.2: A perspective of CsSnI_3 in the tetragonal phase (II). The tilting of the octahedra is on the ab plane (left panel), while no tilt occurs along the c axis (right panel).

are mainly due to structural variations (deformation and tilt) of the octahedra and dramatically depend on the choice of the halogen X, evidencing two limit cases that are $X=\text{Cl}$ and $X=\text{I}$. In the hybrid perovskites, the replacement of the inorganic cation with an organic molecule produces changes in the structural and electronic properties respect to the corresponding inorganic compound. To give an insight on the effects due to this substitution, and on the tunable properties associated with a suitable choice of the molecule inside the octahedra inorganic network, a comparison between hybrid and related inorganic perovskites is necessary. For this reason, we first analyze the two limit cases of CsSnX_3 , and then the hybrid counterparts.

5.2.1 Phase transitions in CsSnI_3

By lowering the temperature, the CsSnI_3 compound undergoes three phase transitions [140] in the following order: *cubic* (I) $\xrightarrow{T=426\text{K}}$ *tetragonal* (II) $\xrightarrow{T=351\text{K}}$ *orthorhombic* (III). In order to obtain, for each phase, the atomic geometry inside the unit cell, we used X-ray diffraction data [140] as a starting point for total energy minimization. Ab-initio structural parameters of the fully relaxed system are reported in Table 5.1. Theoretical structural results are in a good agreement with the experimental data reported by Yamada [140] et al. The cubic phase of CsSnI_3 (or phase I) is characterized by a perfect perovskitic structure (Fig. 5.1), with regular SnI_6 octahedra aligned in the three directions of the cubic lattice. The transition

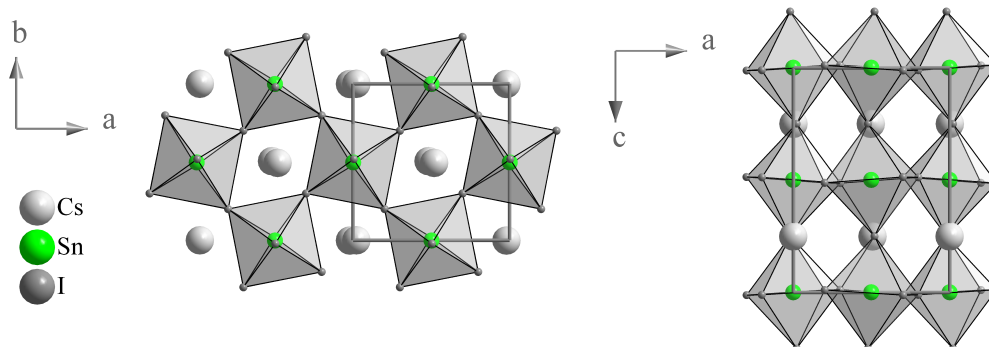


Figure 5.3: A perspective of CsSnI₃ in the orthorhombic phase (III). In the left (right) panel it is shown the tilting of the octahedra in the *ab* (*ac*) plane.

to the tetragonal phase (or phase II) is characterized by a tilt of the octahedra in the *ab* plane (Fig. 5.2), the unit cell volume is nearly doubled (in particular, the $a=b$ lattice parameter is nearly $\sqrt{2}$ times the value of the lattice constant of cubic phase) and two CsSnI₃ unit structures form the basis inside the unit cell. The six halogens I surrounding the Sn at the centre of the octahedra, are placed at nearly the same distance (with a mean value of 3.136 Å and a maximal difference of 0.01 Å between each other), while the internal angles of each octahedron are exactly 90 degrees, meaning that no deformation of the octahedra occur. The regularity of the octahedra allows to establish tilting angles just by looking at the difference between a flat angle (180 degrees) and the iodine bridging angle Sn–I–Sn in the plane *ab* (Θ_{ab}) or parallel to the *c* axis (Θ_c). Clearly, the flat angle corresponds to the case of perfectly aligned Sn–I–Sn chains, as in the case of perfect cubic perovskites, in which tilting angles are null. In the tetragonal phase, the tilting angle is null along the *c* axis, while the bridging angle Θ_{ab} is equal to 162 degrees. This corresponds to the mutual rotation of the adjacent SnI₆ octahedra by 9 degrees in the opposite directions about the *c* axis.

In the orthorhombic phase (or phase III), the unit cell increases further two times along the *c* axis, thus containing four CsSnI₃ units. The Sn–I distances in the octahedron are almost of the same length (with a mean value of 3.146 Å and a maximal difference of 0.03 Å between each other), whereas the internal angles now differ at most of 0.5 degrees from 90 degrees, thus leading us to consider also the

Table 5.1: Crystallographic parameters. The distances a , b and c are measured in \AA , angles α, β and γ in degrees, energy gap E_g in eV. N is the number of structural units in the unic cell. In parenthesis we report the experimental results.

$A\text{SnX}_3$	a	b	c	α	β	γ	N	E_g
CsSnI ₃ (I)	6.231 (6.219)	—	—	—	—	—	1	0.3479
CsSnI ₃ (II)	8.772 (8.772)	8.772 (8.772)	6.261 (6.261)	—	—	—	2	0.4808
CsSnI ₃ (III)	8.738 (8.688)	8.73 (8.643)	12.528 (12.378)	—	—	—	4	0.5610
CsSnCl ₃ (I)	5.601 (5.604)	—	—	—	—	—	1	0.9499
CsSnCl ₃ (II)	16.672 (16.10)	7.735 (7.425)	5.768 (5.748)	—	92.8 (93.2)	—	4	2.8447
MASnCl ₃ (IV)	5.888 (5.726)	8.381 (8.277)	8.013 (7.190)	90.2 (90.4)	96.1 (93.08)	90.15 (89.9)	2	1.9575
MASnI ₃ (I)	6.286 (6.242)	—	—	—	—	—	1	0.4683
FOSnI ₃ (I)	6.396 (6.316)	—	—	—	—	—	1	0.6982

orthorhombic phase as constituted by a regular octahedra network. This means that, also in this case, we can relate the tilting of the octahedra to the Sn–I–Sn bridging angles. In the ab plane there is a slight variation of Θ_{ab} respect to the tetragonal phase, while a tilt appears along the c axis as indicated by Θ_c , whose value (173 degrees) differs from a flat angle. It is interesting to note that successive phase transitions mainly do not affect the octahedron internal structure (the mean value of Sn–I lengths varies from 3.115 \AA (phase I) to 3.146 \AA (phase III)). These phases are indeed characterized by successive increasing of the tilting of the octahedra network.

The electronic band structure and the density of states of CsSnI₃ are shown in

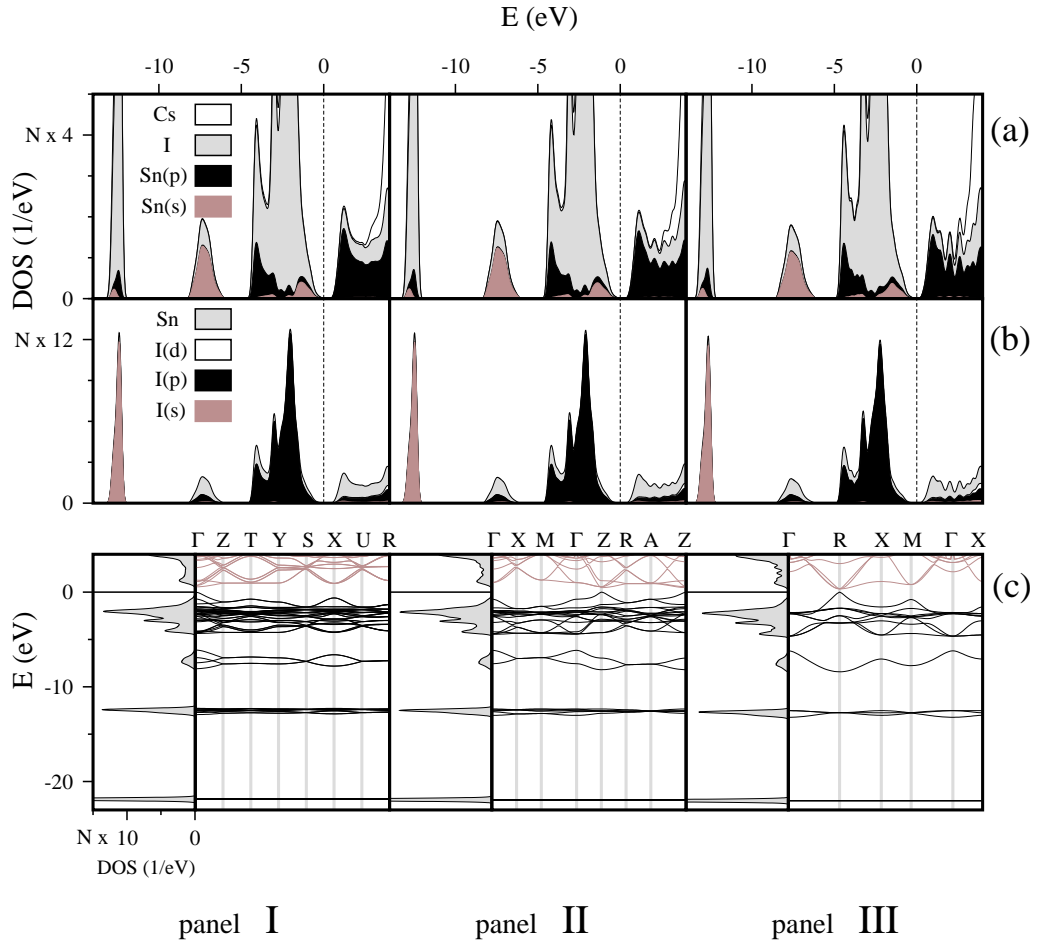


Figure 5.4: The calculated band structure, the total and the projected density of states of CsSnI_3 in the phase III (left panel), II (central panel) and I (right panel). The VBM is arbitrarily set to zero, filled (empty) states are indicated with black (brown) lines. Details of the figure are given in the text.

Fig. 5.8. The left panel is associated to the orthorhombic phase or phase III, the central panel to the phase II, and the right one to the phase I. The calculated band structure for each phase is reported in section (c) of each panel, accompanied by the total density of states (the grey shadows on the left). The energy scale is in eV and the origin of energy is arbitrarily set to be at the valence band maximum (VBM). The density of states (DOS) in the unit cell is calculated in eV^{-1} , so that its integral over all the occupied energy levels, gives the number of electrons in the unit cell. N is

the number of CsSnI₃ units inside the unit cell. The DOS and the projected density of states (PDOS) (section (a) and (b) of each panel in Fig. 5.8) are opportunely scaled by N to make a clear comparison between each phase. The projection is done onto the atomic orbitals of each atom. In section (a) the contribution of Sn s and p orbitals to the total DOS is shown, along with the total contribution of I atoms and Cs cation. Similarly, in section (b) the contribution of I s , p and d orbitals to the DOS is represented, along with the total contribution of Sn and Cs. From the band structure calculation, a direct band gap is found in all the phases of CsSnI₃. A gradual increasing of the electronic band gap is observed by following the series of phase transitions I→II→III, that is, by increasing the tilting of the octahedra network. In phase I the direct gap is at the R point of the Brillouin zone, at Z in phase II and at Γ in phase III: the values of the energy gap are reported in Table 5.1. The rapid lowering of the density of states approaching to the VBM and the shape of the band structure suggest that the VBM is in correspondence to a sharp local maximum of the valence band. An overall similarity between the PDOS of all the phases is found: the valence band is mostly dominated by I p orbital contributions, whereas, in the near band-gap energy region, the conduction band is essentially dominated by Sn p orbitals, with a slight contribution of I p orbitals. Moreover a slight superposition of Sn s and p orbitals with that of I p orbitals is found in the valence energy region, thus suggesting a partial hybridization of the Sn–I bond. The Sn p states mostly lie above the VBM, confirming the ionic character of the compound.

5.2.2 Phase transitions in CsSnCl₃

By lowering temperature, the CsSnCl₃ compound undergoes two phase transitions [35] in the following order: *cubic* (I) $\xrightarrow{T=359K}$ *monoclinic* (II). In order to obtain, for each phase, the atomic geometry inside the unit cell, we used X-ray diffraction data [141] as a starting point for total energy minimization. A good agreement between computed and measured structural parameters is found for both phases, as shown in Table 5.1. In the cubic phase, the CsSnCl₃ compound exhibits a perfect perovskitic structure (Fig. 5.1), with a regular untilted octahedra network. The transition to the monoclinic phase is characterized by a dramatic change of the structural

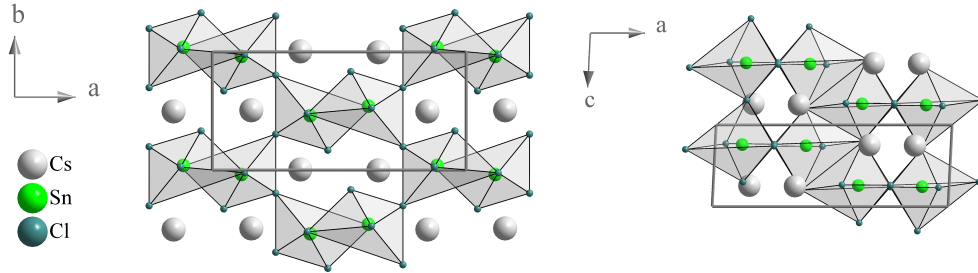


Figure 5.5: A perspective of CsSnCl_3 in the monoclinic phase (II) on the ab plane (left panel) and on the ac plane (right panel).

properties of the compound, as clearly shown in Fig. 5.5. The octahedra are strongly deformed: the Sn–Cl distances in the SnCl_6 octahedron are in agreement with the results reported by Yamada et al [35]. According to their interpretations, in this phase the octahedron is constituted by SnCl_3^- anions which form a trigonal pyramid (Sn–Cl: 2.54, 2.57 and 2.62 Å) having three long interanionic interactions (Sn–Cl: 3.15, 3.49 and 4.07 Å). The deformation effect is strongly related to the presence of the Cl halogen: in particular, the higher electronegativity of Cl (respect ot that of iodine) causes the increasing in the stereochemical activity of the lone pair of electrons on Sn, with the consequent deformation of the SnCl_6 octahedra [34]. Moreover, the octahedra are no more corner sharing (Fig. 5.5), forming edge-sharing octahedra chains along the c axis, separated from each other by Cs cations along the a and b axes. As shown in Fig. 5.5, the Cs cation is no more embedded in a pseudo-cubic cage with Sn atoms at vertex, as a consequence of the corner-sharing octahedra breaking network.

The electronic band structure and the density of states of CsSnCl_3 are shown in Fig. 5.6 (left and central panels) following the same scheme of Fig. 5.8. In the cubic phase, it is evident a direct band gap at R point, and a sharp maximum in the valence band appears, in complete analogy to the cubic phase of CsSnI_3 . The transition to the monoclinic phase dramatically changes the electronic properties of the compound. A wide band gap (at D point) is found (Table 5.1) in the monoclinic phase: the sharp maximum in the valence band disappears in this phase, as also shown by the different behavior of the DOS approaching to the VBM.

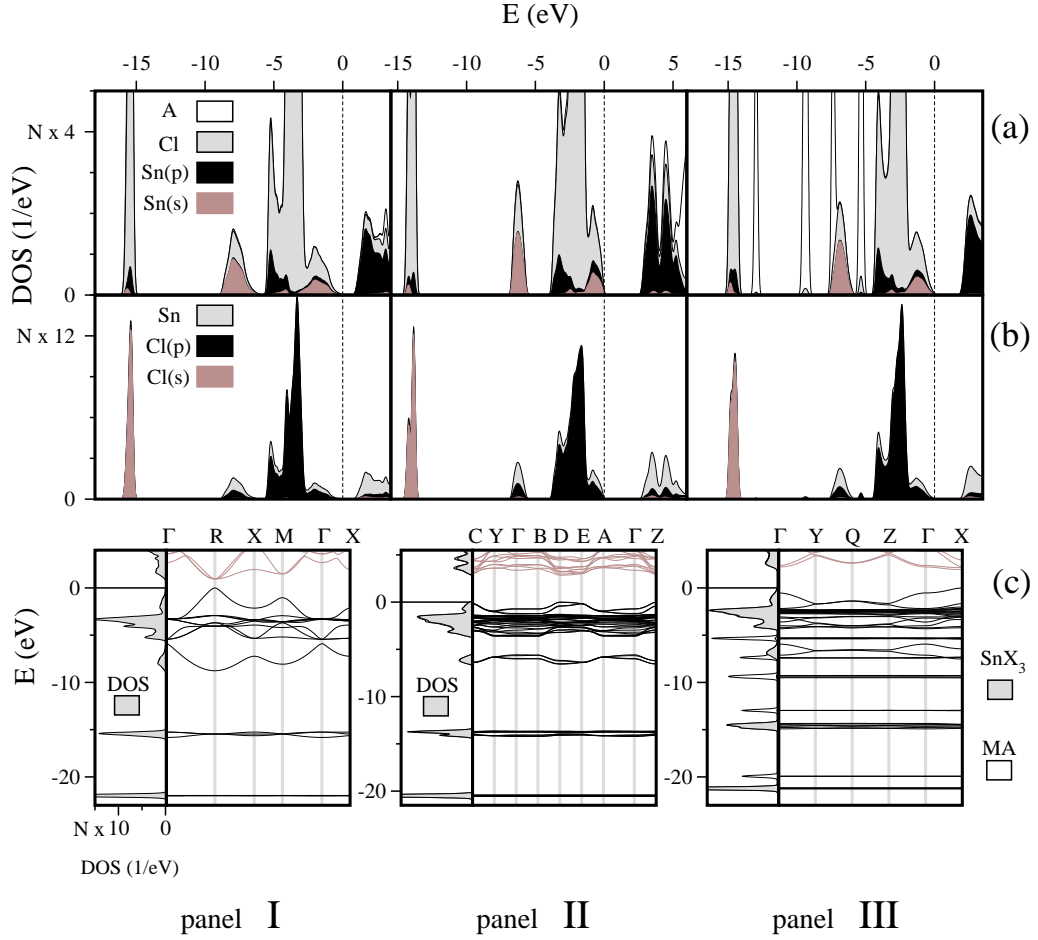


Figure 5.6: The calculated band structure, the total and the projected density of states of CsSnCl₃ in the cubic phase (left panel), and in the monoclinic phase (central panel), and of CH₃NH₃SnCl₃ in the triclinic phase (right panel). The VBM is arbitrarily set to zero, filled (empty) states are indicated with black (brown) lines. In section (c) of panel III, the total DOS (on the left of the band structure) is divided in organic (white) and inorganic (grey) contributions

Moreover, looking at the band structure of this phase (section (c) of panel II), the bands are dispersed along the z direction of the Brillouin zone, that is along $C(0, \frac{1}{2}, \frac{1}{2}) \rightarrow Y(0, \frac{1}{2}, 0)$, $B(-\frac{1}{2}, 0, 0) \rightarrow D(-\frac{1}{2}, 0, \frac{1}{2})$, $E(-\frac{1}{2}, \frac{1}{2}, \frac{1}{2}) \rightarrow Y(-\frac{1}{2}, \frac{1}{2}, 0)$ and $\Gamma(0, 0, 0) \rightarrow Z(0, 0, \frac{1}{2})$. The bands are indeed nearly flat elsewhere. This effect is due to the breaking of the corner-sharing 3D octahedra network, with the forma-

tion of isolated edge-sharing octahedra chains. As a consequence, the bands are dispersed mainly along the chain direction. In analogy with the cubic phase, the valence band is dominated by Cl p orbitals, whereas, in the near band-gap energy region, the conduction band by the Sn p orbitals, with a minor admixture from Cl p states. It is interesting to note that a similar structure of the PDOS is found in all the phases of CsSnI₃ (with the I atoms playing the role of Cl).

5.2.3 CH₃NH₃SnCl₃ in the low-temperature phase

In CH₃NH₃SnCl₃ compound, four phase transitions are found [35] by lowering the temperature, in the following order: *cubic* (I) $\xrightarrow{T=463K}$ *rhomboidal* (II) $\xrightarrow{T=331K}$ *monoclinic* (III) $\xrightarrow{T=307K}$ *triclinic* (IV). In the high-temperature phases (I and II), mostly regular perovskitic cages embed the methylammonium (MA) CH₃NH₃ cations, which are believed to be dynamically disordered (random orientation) [35]. The dynamical disorder is removed on cooling: the low-temperature phases (III and IV) are characterized by octahedra SnCl₆ distortions, creating potential wells for the NH₃⁺ polar head of the MA cations, which assume an ordered orientation. Moreover, by comparing the crystallographic data [35] of both monoclinic and triclinic phases, it is evident that the III→IV phase transition does not lead to significant changes in the structure of the compound. We focus on the triclinic phase and compare the structural and electronic properties of the low-temperature phase of MASnCl₃ with that of the inorganic counterpart.

In order to obtain the atomic geometry inside the unit cell, we used the X-ray diffraction data [35] as the starting point for the total energy minimization. The ab-initio structural parameters of the fully relaxed system are reported in Table 5.1 in a pretty good agreement with the experimental data [35]. A perspective of the phase IV of MASnCl₃ is shown in Fig. 5.7. In contrast with the inorganic counterpart, the methylammonium guarantees great stability to the inorganic cage, which preserves a corner-sharing octahedra network structure in the low-temperature phase. The octahedra are not regular. In analogy with CsSnCl₃, in this phase the octahedron is constituted by SnCl₃⁻ anions which form a trigonal pyramid (Sn–Cl: 2.57, 2.65 and 2.7 Å) having three long interanionic (Sn–Cl: 3.14, 3.22 and 3.37 Å). On the other hand, a comparison between Fig. 5.5 and Fig. 5.7 clearly shows that these

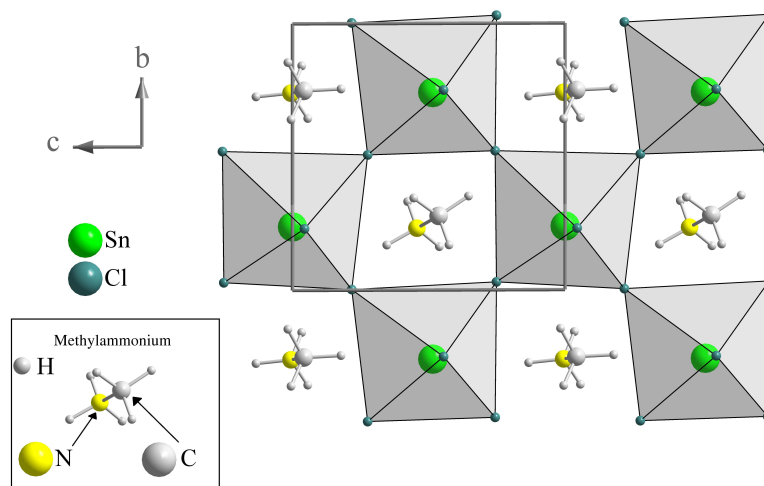


Figure 5.7: A perspective on the bc plane of $\text{CH}_3\text{NH}_3\text{SnCl}_3$ in the triclinic phase.

deformation effects are reduced with respect to the low-temperature phase of the inorganic CsSnCl_3 . The band structure of the triclinic MASnCl_3 is represented. Fig. 5.6 (section (c) of panel III). The direct band gap is at Γ point, in correspondence to a fairly sharp maximum of the valence band, as also evidenced by the behavior of the DOS approaching to the VBM. Interestingly, the value of the band gap is reduced with respect to that of the inorganic counterpart in the low-temperature phase. The organic contribution to the total DOS (the white shadow on the left of the band structure) is in correspondence of flat bands, evidencing that no cation contribution occurs in the near band-gap region.

5.2.4 ASnI_3 with $\text{A}=[\text{CH}_3\text{NH}_3, \text{NH}_2\text{CH}=\text{NH}_2]$

In analogy with the inorganic CsSnI_3 , the hybrid ASnI_3 with $\text{A}=[\text{CH}_3\text{NH}_3, \text{NH}_2\text{CH}=\text{NH}_2]$ adopt a cubic perovskite structure in the highest temperature phase (room temperature [124]). Mitzi and coworkers [124] measured the room temperature X-ray powder patterns demonstrating the isostructural relationship between the two compounds and the increase of the cubic lattice parameter when the smaller CH_3NH_3 methylammonium (MA) is replaced by the $\text{NH}_2\text{CH}=\text{NH}_2$ formamidinium (FO). Moreover, in this phase a dynamical disorder of the molecules is believed, justifying the absence

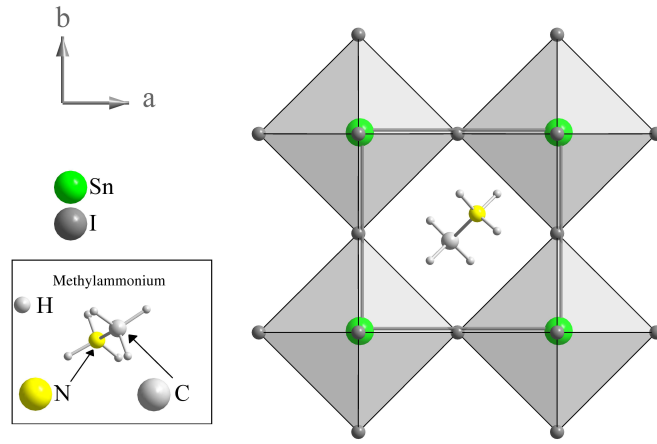


Figure 5.8: A perspective of $\text{CH}_3\text{NH}_3\text{SnI}_3$ in the cubic phase

of X-ray diffraction patterns of the organic cations [108, 110, 111, 112, 113, 116, 117, 122, 35, 126, 128]. Nevertheless, in our calculations the molecule is fixed at the configuration corresponding to the minimum of the total energy of the system. Some points should be highlighted here: i) the substitution of the inorganic cation Cs with small organic molecules (as in the case of MA and FO) leads to an increasing of the cell size, so that the organic cation must fit into a larger cuboctahedral hole formed by the nearest I atoms; ii) our results on CsSnI_3 indicate that the presence of iodine (in contrast to Cl) assures the formation of almost regular octahedra: the different phases of CsSnI_3 are characterized by tilted octahedra network with negligible deformation effects; iii) in the cubic perovskite, the tilting of corner-sharing octahedra is forbidden by the symmetry of the crystal [142] (whose space group is $Pm\bar{3}m$). All these observations suggest that, even if the molecule is fixed, the simulated hybrid ASnI_3 would exhibit a mostly regular perovskitic structure, at most affected by octahedra deformation. Moreover, these deformation effects are expected to be very slight because of the presence of iodine and of the reduced dimensions of the molecules considered. The lattice parameters of the cubic MASnI_3 and FOSnI_3 obtained from fully relaxed geometry are reported in Table 5.1 in a good agreement with the experimental results [124].

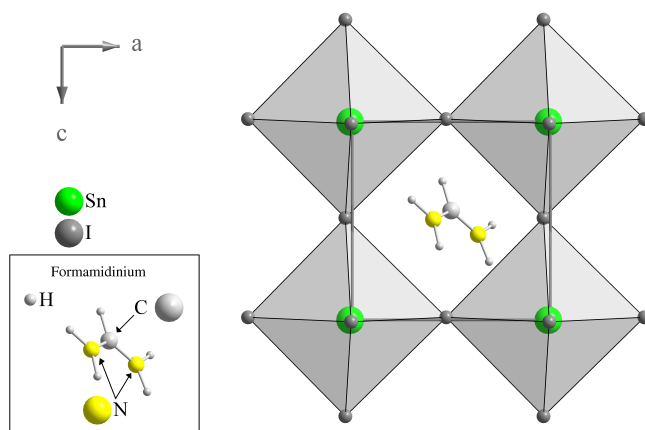


Figure 5.9: A perspective of $\text{NH}_2\text{CH}=\text{NH}_2\text{SnI}_3$ in the cubic phase

The relaxed structures are shown in Figs. 5.8 and 5.9. In both the compounds a mostly regular perovskitic cage embeds the organic molecule, with slight deformations of the Sn_6 octahedra. The octahedra deformation increases by increasing the molecule size, that is by substituting the smaller methylammonium cation with formamidinium. The band structures of MASnI_3 and FOSnI_3 are represented in Fig. 5.10 (section (c) of panel I and II respectively).

For both the compounds, the direct band gap (see Table 5.1) is at R point, in correspondence of a sharp maximum in the valence band. Moreover, the organic contribution to the total DOS (the white shadow on the left of the band structure) corresponds to flat bands (molecular orbitals) that are far from the near band-gap region. In that energy region, the valence and the conduction bands are dominated by the inorganic contribution.

An interesting result is shown in Fig 5.11. The band gap value of the organic compounds is very close to the one of a CsSnI_3 cubic perovskite of the same size. The very small difference between these values can be attributed to the slight deformation of the octahedra in the hybrid perovskites. This means that the molecule plays the role as an electron donor exactly like the inorganic cation, but also determines the size of the cell. In Fig. 5.11 the energy band gap values of the tetragonal (phase

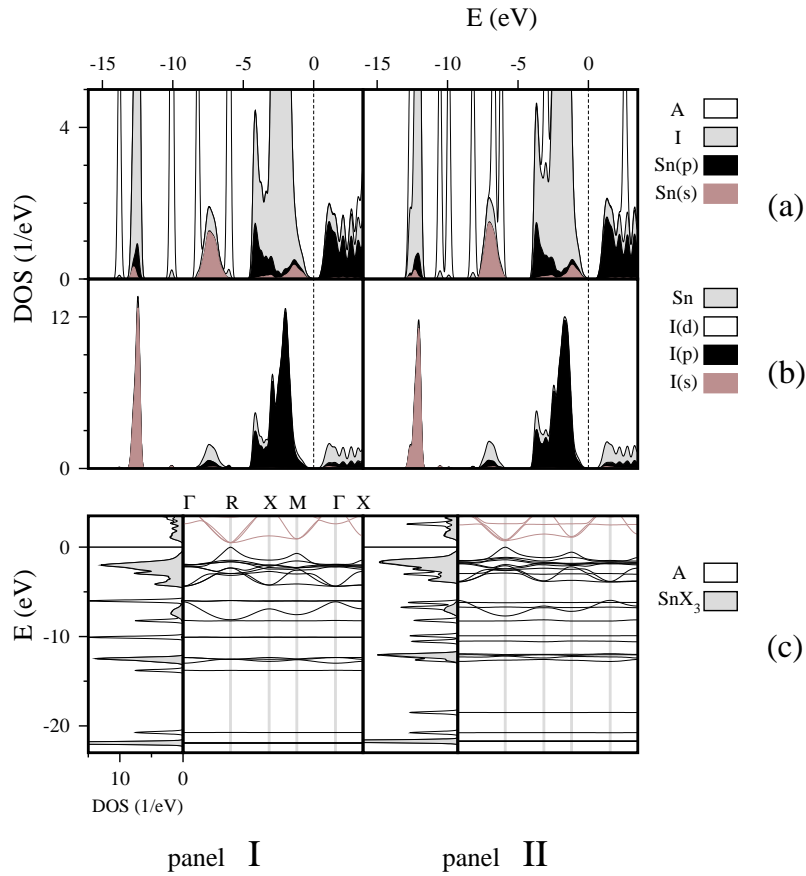


Figure 5.10: The calculated band structure, the total and the projected density of states of $\text{CH}_3\text{NH}_3\text{SnI}_3$ (left panel) and $\text{NH}_2\text{CH}=\text{NH}_2\text{SnI}_3$ (right panel) in the cubic phase. The VBM is arbitrarily set to zero, filled (empty) states are indicated with black (brown) lines. In section (c), the total DOS (on the left of the band structures) is divided in organic (white) and inorganic (grey) contributions

II) and orthorhombic (phase III) of CsSnI_3 are also reported, in correspondence to the cubic CsSnI_3 (phase I). Here some points can be highlighted: i) In ASnI_3 , the substitution of the inorganic Cs cation with small organic molecule stresses the network enlarging the perovskitic cage with a resulting increasing of the band gap; ii) the network tilting in the low temperature phases of CsSnI_3 results in an increasing of the band gap; iii) the breaking of the network in the low-temperature phase of CsSnCl_3 causes a dramatic increasing of the band gap; v) the low-temperature

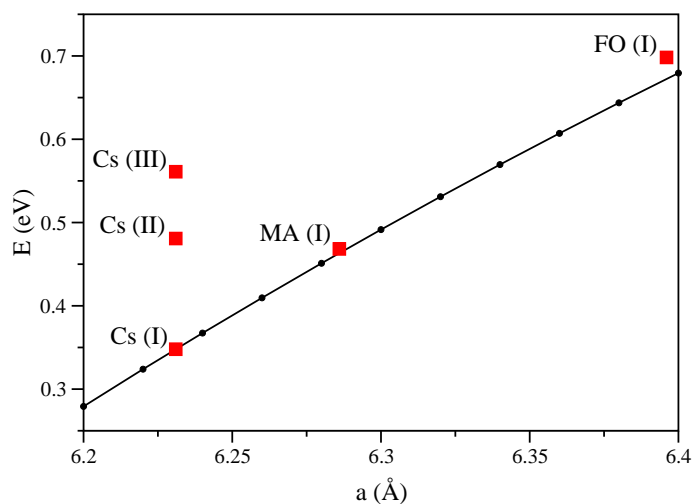


Figure 5.11: The energy band gap as a function of the a cubic lattice. The black circles represent the calculated band gap for perfect cubic perovskite CsSnI₃ with different size, the black line is intended as visual guide. The red squares represent the band gap of CsSnI₃ in the three phases and the band gap of MASnI₃ and of FOSnI₃ in the cubic phase.

phase of the hybrid MASnCl₃ preserves the octahedra network structure and, even if the network is enlarged by the molecule, the compound is characterized by a lower band gap with respect to the inorganic counterpart (in the low-temperature phase). All these considerations suggest that the electronic properties of tin-halide perovskitic compounds are strongly dependent on the structure of the inorganic cage, and in particular, on the formation of the octahedra network. The molecule thus plays a crucial role, because its presence strongly affects the network structure: the small MA cation gives stability to the octahedra network hybrid structure, and by substituting the molecule, it is possible to tune the inorganic cage volume and as consequently the band gap.

Table 5.2: Comparison between experimental and theoretically calculated parameters for room-temperature phases of $\text{CH}_3\text{NH}_3\text{SnX}_3$ ($\text{X}=\text{Cl},\text{Br}$). Lengths are expressed in Å and angles in degrees.

monoclinic $\text{CH}_3\text{NH}_3\text{SnCl}_3$			
parameters	film	powder	calculated
a	5.73(1)	5.69(1)	5.878
b	–	8.23(1)	8.381
c	–	7.94(1)	8.013
β	–	93.2(1)	96.1
cubic $\text{CH}_3\text{NH}_3\text{SnBr}_3$			
parameters	film	powder	calculated
a	5.88(1)	5.89(1)	6.001

5.3 A combined theoretical and experimental investigation of $\text{CH}_3\text{NH}_3\text{SnX}_3$ ($\text{X}=\text{Cl}, \text{Br}$) thin films

In this section, we present a combined theoretical and experimental investigation on $\text{CH}_3\text{NH}_3\text{SnX}_3$ ($\text{X}=\text{Cl}, \text{Br}$) thin films, resulting from a collaboration with Fabio Chiarella, Andrea Zappettini, and Francesca Licci (IMEM - CNR, Area delle Scienze 37/A, I-43100 Parma, Italy). They have realized thin films of both the hybrid compounds and characterized them by means of absorption analysis, room temperature resistivity and x-ray structural analysis. The experimental investigation is combined with ab-initio calculations to give an insight on the electronic properties of these compounds.

Well-oriented thin films of methyl-ammonium trihalogenostannates $\text{CH}_3\text{NH}_3\text{SnX}_3$ compounds ($\text{X} = \text{Cl}, \text{Br}$) are grown by the single source thermal ablation technique. The structural calculations well reproduce the measured lattice parameters and optical measurements reveal a direct gap absorption onset for both compounds, in agreement with the calculated band structures. Room temperature diffraction anal-

Table 5.3: Measured resistivity (ρ) and absorption gap (E_g) for the $\text{CH}_3\text{NH}_3\text{SnX}_3$ films. Computed band gaps (with and without inclusion of the GW many-body correction) are reported as well.

X	ρ ($\text{M}\Omega\cdot\text{cm}$)	measured E_g (eV)	theoretical E_g (eV)	
			DFT-GGA	with GW
Br	0.5 ± 0.1	2.15 ± 0.01	1.04	1.90
Cl	1.4 ± 0.1	3.69 ± 0.05	1.94	3.44

ysis of polycrystalline powders of the $\text{CH}_3\text{NH}_3\text{SnCl}_3$ compound (Fig.3.8 (c)) has revealed that the powders do not result cubic, but distorted in a monoclinic or triclinic phase. As reported by Yamada [35] these two distorted cubic structures show only minor differences. From the analysis of the diffraction patterns of the films of both compounds reported in Figs. 3.8 (a) and (b), the films result to be single phase. $\text{CH}_3\text{NH}_3\text{SnBr}_3$ diffraction pattern is compatible with a cubic perovskite structure [143].

The measured a -axis lattice parameters of the films, as well as the lattice parameters of the powders for both compounds, are reported in Table 5.2 and compared with the calculated ones.

The film resistivity presents a semiconducting temperature behavior and room-temperature resistivity measurements are summarized in Table 5.3.

As described in Section 3.4.2, absorbance of 500 nm thick films were measured in air at room temperature. The absorption coefficient α , shown in the inset of Fig. 3.9, was obtained by including corrections for multiple reflections. It can be seen that the absorption edge rapidly raises to values typical for direct band-gap crystals ($\alpha \sim 10^4\text{--}10^5\text{ cm}^{-1}$). As such, it can be described [72] by the relation $(\alpha h\nu)^2 \propto (h\nu - E_g)$, as shown by the linear slope in Fig. 3.9. In the case of $\text{CH}_3\text{NH}_3\text{SnBr}_3$, the presence of a bump is related to an overlap of multiple direct gap contributions to the absorption. Multiple direct band gaps are evident from the calculated band structure, as it is shown in Fig.5.12. The fitted band gaps values E_g are reported in Table 5.3.

The lattice parameter of the cubic $\text{CH}_3\text{NH}_3\text{SnBr}_3$ obtained from fully relaxed

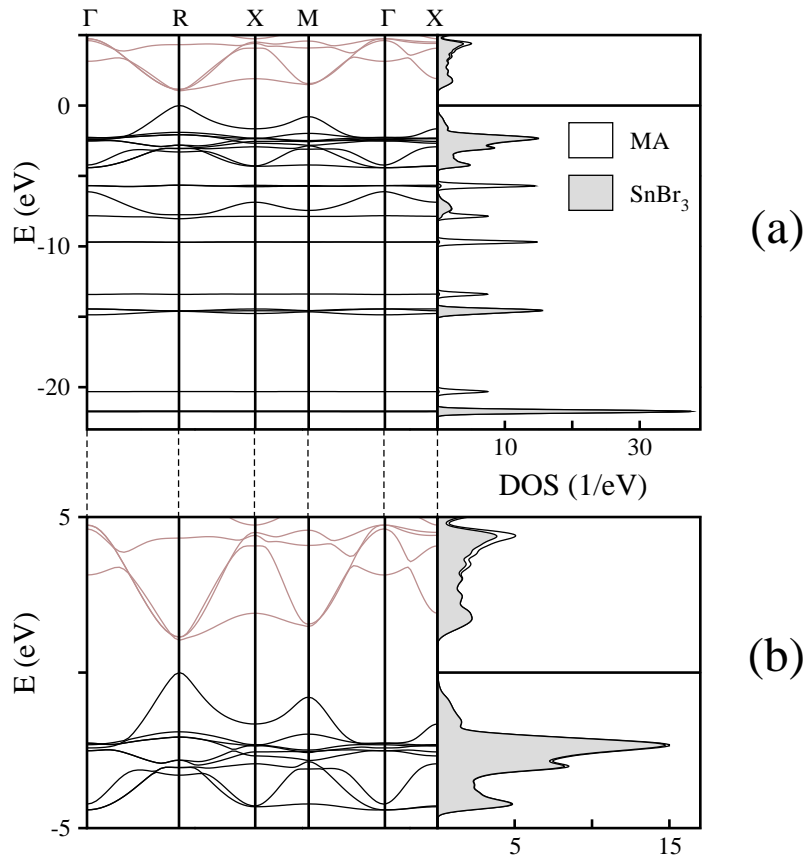


Figure 5.12: The calculated band structure, the total and the projected density of states for $\text{CH}_3\text{NH}_3\text{SnBr}_3$ in the cubic phase. In panel I the band structure is shown along the high symmetry directions in the Brillouin zone. The VBM is arbitrarily set to zero, filled (empty) states are indicated with black (brown) lines. In panel II, the total DOS (on the left of the band structures) is divided in organic (white) and inorganic (grey) contributions

(ions and electrons) geometry is $a=6.001 \text{ \AA}$, as also reported in Table 5.2, in a pretty good agreement with the experimental results. In the case of $\text{CH}_3\text{NH}_3\text{SnCl}_3$ at room temperature the monoclinic structure is chosen, with an unit cell containing two $\text{CH}_3\text{NH}_3\text{SnCl}_3$ units.

We used X-ray diffraction data [35] as a starting point for total energy minimization. Ab-initio structural parameters of the fully relaxed system are reported in Table 5.2. Theoretical structural results are in a good agreement with the experimental data obtained in this work as well as with those reported by Yamada

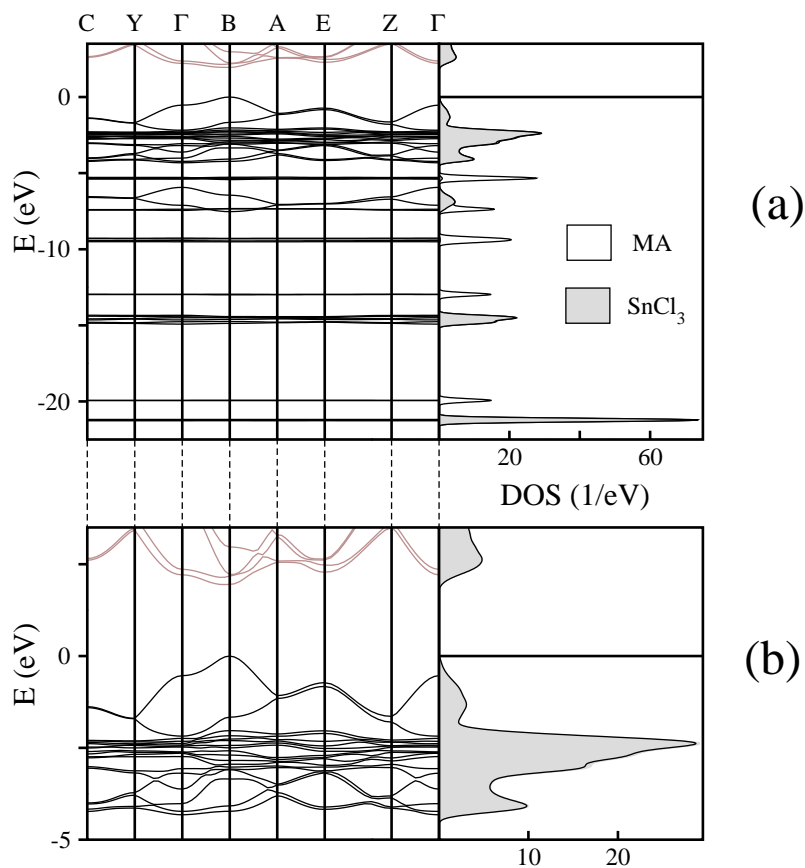


Figure 5.13: The calculated band structure, the total and the projected density of states for $\text{CH}_3\text{NH}_3\text{SnCl}_3$ in the monoclinic phase. In panel *I* the band structure is shown along the high symmetry directions in the Brillouin zone. The VBM is arbitrarily set to zero, filled (empty) states are indicated with black (brown) lines. In panel *II*, the total DOS (on the left of the band structures) is divided in organic (white) and inorganic (grey) contributions

[35]at al. Our results on Sn-Cl distances evidence SnCl_3^- anions formation with a trigonal pyramid structure, characterized by a Sn-Cl bond length of about 2.6 Å and a Cl-Sn-Cl angle slightly greater than 90 degrees. Our results well reproduce isolated SnCl_3^- anions experimentally recognized in the distorted octahedral coordination [35]. The calculated band structures for both compounds along high symmetry directions in the Brillouin zone are shown in Figs 5.12 and 5.13.

5.4 Conclusions

In this work, we have given a detailed description of the structural and electronic properties of both inorganic and hybrid perovskites based on tin halides. The comparison between hybrid perovskites and the inorganic counterparts sheds light on the effects of the molecule on the structural and electronic properties of the compound. Our results show that the electronic properties of tin-halide perovskitic compounds are strongly dependent on the structure of the inorganic cage. In particular, it is found that the structural variation (deformation, tilt and breaking) of the corner-sharing octahedra network strongly affects the band gap of these compounds. The small organic cations (methylammonium and formamidinium) play a crucial role because their presences affects the network structure. It has been shown that the methylammonium gives stability to the octahedra network. Moreover the substitution of the inorganic Cs with the methylammonium and formamidinium causes a gradual increasing of the volume of the cubic inorganic cage with a consequent increasing of the electronic band gap. It is important to stress that the size of the molecule has to be accurately chosen, since the organic molecule must fit into a rigid and relatively small cuboctahedral hole formed by the inorganic cage. A tolerance factor t is defined for hybrid perovskites [14], as a function of the ionic radii of the inorganic elements (Sn and the halogen in our case). Considering that the C–C and C–N bond lengths are of the order of 1.4 Å, it is believed that in tin-halides based perovskites, only the smallest organic molecules, those containing two or three atoms (excluding hydrogen), should fit into the structure [14]. Larger more complex monoammonium ($R-NH_3^+$) or diammonium ($^+NH_3-R-NH_3^+$) cations are indeed used to realize layered organic-inorganic structures [121, 132, 133, 135, 136]. Among the layered systems, the simplest examples include the compounds [14, 20] $(R-NH_3)_2BX_4$ and $(NH_3-R-NH_3)BX_4$, where B is a divalent metal and X is the halogen.

As far as the thin films of $CH_3NH_3SnX_3$ compounds (with $X = Br, Cl$), their structural, optical and electronic properties have been characterized combining theoretical and experimental analysis. Structural calculations on the $CH_3NH_3SnCl_3$ monoclinic phase and $CH_3NH_3SnBr_3$ cubic phase well agree with the measured lattice parameters, as determined from X-ray analysis. The comparison of the absorption measurements with the theoretical calculations allows us to assign the ab-

sorption onset for both compounds to a direct gap transition, with the relevant energy levels strongly associated with the inorganic cage.

Conclusions

In this thesis we have performed DFT calculations for two different classes of materials, obtained by combining organic molecules with inorganic compounds. The first class of systems which have been considered concerns silicon surface functionalization through organic molecules. The second one is represented by hybrid organic-inorganic perovskites based on tin halides.

Using first-principles calculations we have analyzed the properties of organic adsorbates on the silicon (001) surface. In this thesis, we have considered ethylene and a class of cyclopentene derivatives, with the general formula $C_5H_6-R_1R_2$ where R_1 and R_2 are functional groups controlling the molecular dipole moments. These molecules anchor to the surface through the same [2+2] cycloaddition mechanism. Because they all show similar bonding properties, any variation in the surface properties must be related to the functional group. In particular we have focused on the changes in the surface electron affinity induced by coverage. This variation is proportional to the surface dipole moment variation induced by the molecular layer covering the surface. Ab-initio calculations have been performed for both the clean surface and the adsorbate-covered surfaces. Our results clearly show that the chemical adsorption induces structural reconstructions on both the surface and the adsorbed molecule. The electron affinity variation induced by adsorbates have been evaluated as a function of both the molecular species and the coverage (half and full coverage have been considered). Moreover, we have analyzed the different contributions setting up the change of the surface dipole moment induced by the coverage. The total surface dipole moment variation has been decomposed into three terms: i) the surface dipole moment variation due to the surface structural modification caused by the chemical adsorption; ii) dipole moment induced by the adsorbate-

surface charge transfer, resulting from the chemical bond formation; iii) the dipole moment of the molecular layer. The first two terms are strictly connected to the type of reaction ([2+2] cycloaddition) that changes the surface reconstruction as well as leads to new charge redistribution at the surface due to the chemical bonds formation in the adsorption. Our results indicate that, for the class of molecules considered, these two terms depend only on the coverage. Moreover, they are negligible with respect to the dipole moment of the molecular layer, which is found to be the main cause of the total surface dipole moment variation. We have made an attempt to correlate the dipole moment of the molecular layer and the intrinsic dipole moment of the isolated molecules. Our results clearly indicate that they are not linearly correlated. In particular, it is found that the nonlinear effects are mainly due to the structural rearrangement of the molecules caused by the chemical adsorption on the surface. Our findings demonstrate that, for this class of molecules, it is enough the knowledge of the isolated molecule properties for predicting the properties of the surface-adsorbate complex. In particular, the detailed analysis of the various contributions to the surface dipole has revealed that the common practice of linking the electron affinity variations directly to the dipole moment of the isolated molecule is, as a rule, not always correct. Moreover, all the results indicate how the surface properties can be tuned through a suitable choice of the adsorbate.

The second class of materials that have been studied in this thesis are the hybrid organic-inorganic perovskites based on tin halides. In this thesis, we have given a detailed description of the structural and electronic properties of both inorganic and hybrid perovskites based on tin halides. In particular, we have focused on CsSnCl_3 and CsSnI_3 and the hybrid counterparts $\text{CH}_3\text{NH}_3\text{SnCl}_3$, $\text{CH}_3\text{NH}_3\text{SnI}_3$ and $\text{NH}_2\text{CH}=\text{NH}_2\text{SnI}_3$, obtained by substituting the inorganic Cs cation with methylammonium (CH_3NH_3) and formamidinium ($\text{NH}_2\text{CH}=\text{NH}_2$). The comparison between the hybrid perovskites and the inorganic counterparts sheds light on the effects of the molecule on the structural and electronic properties of the compound. We have considered firstly the inorganic compounds CsSnX_3 with $\text{X}=(\text{Cl},\text{I})$. In the highest temperature phase, both the compounds exhibit a cubic perovskite structure, which consists of corner-linked SnX_6 octahedra, with the Cs cation between them. The compounds undergo different phase transitions by lowering the temperature. The structural and electronic properties of both the compounds have been calculated for

all the phases, finding a good agreement between measured and computed crystallographic data. By focusing on the lowest temperature phase of both CsSnCl_3 and CsSnI_3 , a completely different structural rearrangement is found, due to the different behavior of the Sn lone pair of electrons by varying the halogen. In fact, in presence of I halogen, the structural variations with respect to the cubic phase are restricted to a tilt of the corner-sharing octahedra network, whereas, in the case of Cl halogen, the octahedra are deformed and the corner-sharing octahedra network is broken, with the formation of isolated edge-sharing octahedra chains and a strong widening of the band gap. Interestingly, our results on the $\text{CH}_3\text{NH}_3\text{SnCl}_3$ hybrid perovskite in the lowest temperature phase have shown that the small methylammonium gives stability to the octahedra network, that maintains the corner-sharing structure. Moreover, the band gap is reduced with respect to the inorganic counterpart. By considering the highest temperature cubic phase of $\text{CH}_3\text{NH}_3\text{SnI}_3$ and $\text{NH}_2\text{CH}=\text{NH}_2\text{SnI}_3$, it is found that the substitution of the inorganic Cs with the methylammonium and formamidinium causes a gradual increasing of the volume of the inorganic cage. Our results clearly show that the electronic properties of tin-halide perovskitic compounds are strongly dependent on the structure of the inorganic cage: i) the increasing of the volume of the cubic perovskitic cage leads to an increasing of the band gap, whereas the breaking of the octahedra network causes a strong widening of the band gap; ii) the calculations of the density of states, projected onto the atomic orbitals, indicate that for all studied compounds, the near-gap band structure is governed by the SnX_3 inorganic perovskitic cage, with no contribution of the cations (organic or inorganic). Our results indicate that the small organic cations (methylammonium and formamidinium) play a crucial role because their presences affects the network structure. These observations lead to the conclusion that the electronic properties (in particular the band gap) can be tuned by a suitable choice of the organic molecule, and, in particular, of its size. It is important to stress that the size of the molecule has to be accurately chosen, since the organic molecule must fit into a rigid and relatively small cuboctahedral hole formed by the inorganic cage. Larger and more complex monoammonium (R-NH_3^+) or diammonium ($^+\text{NH}_3\text{-R-NH}_3^+$) cations are indeed used to realize layered organic-inorganic structures.

Our investigation on both adsorbed molecules on the silicon (001) surface and

hybrid perovkites based on tin halides, performed by means of DFT calculations, indicate that electronic properties of such materials can be modulated through a suitable choice of the organic molecules.

Bibliography

- [1] R. J. Hamers, and Y. Wang, Chem. Rev. **96**, 1261 (1996).
- [2] R. A. Wolkow, Annu. Rev. Phys. Chem. **50**, 413 (1999) and references therein.
- [3] M.A. Filler, and S. F. Bent, Prog. Surf. Sci. **73**, 1 (2003) and references therein.
- [4] S. F. Bent, Surf. Sci. **500**, 879 (2002)
- [5] J. Yoshinobu, Prog. Surf. Sci. **77**, 37 (2004).
- [6] F. Patolsky, G. Zheng, and C. M. Lieber, Anal. Chem. **78**, 4260 (2006).
- [7] J.M. Buriak, Chem. Rev. **102**, 1271 (2002) and references therein.
- [8] R.J. Hamers, S.K. Coulter, M.D. Ellison, J.S. Hovis, D.F. Padovitz, M.P. Schwartz, C.M. Greenlief, and J.N. Russel Jr., Acc. Chem. Res. **33**, 617 (2003) and references therein.
- [9] G. Festa, M. Cossi, V. Barone, G. Cantele, D. Ninno, and G. Iadonisi, J. Chem. Phys. **122**, 184714 (2005).
- [10] I. Borriello, G. Cantele, D. Ninno, G. Iadonisi, M. Cossi and V. Barone, Phys. Rev. B **76**, 35430 (2007).
- [11] C. Sanchez, B. Julian, P. Belleville, and M. Popall, J. Mater. Chem. **15**, 3559 (2005) and references therein.
- [12] P. Gomez-Romero, Adv. Mater. **13**, 163 (2001) and references therein.

- [13] F. Mammeri, E. Le Bourhis, L. Rozes, and C. Sanchez, *J. Mater. Chem.* **15**, 3787 (2005) and references therein.
- [14] Mitzi, D. B. *Prog. Inorg. Chem.* **48**, 1 (1999) and references therein.
- [15] S. I. Stupp, and P. V. Braun, *Science* **277**, 1242 (1999).
- [16] C. P. Collier, R. J. Saykally, J. J. Shiang, S. E. Henrichs, and J. R. Heath, *Science* **277**, 1978 (1997).
- [17] C. R. Kagan, D. B. Mitzi, C. D. Dimitrakopoulos, *Science* **286**, 945 (1999).
- [18] D. B. Mitzi, S. Wang, C. A. Feild, C. A. Chess, and A. M. Guloy, *Science* **267**, 1473 (1995).
- [19] D. B. Mitzi, C. A. Feild, W. T. Harrison, and A. M. Guloy, *Nature* **369**, 467 (1994).
- [20] D. B. Mitzi, K. Choudroudis, and C. R. Kagan, *IBM J. Res. Dev.* **45**, 29 (2001).
- [21] J. H. Schön, Ch. Kloc, E. Bucher, and B. Batlogg, *Nature* **403**, 408 (2000).
- [22] M. Grätzel, *Nature* **414**, 338 (2001).
- [23] Y. X. Liu, M. A. Summers, C. Edder, J. M. J. Frechet, and M. D. McGehee, *Adv. Mater.* **17**, 2960 (2005).
- [24] S. E. Shaheen, C. J. Brabec, N. S. Sariciftci, F. Padinger, T. Fromherz, and J. C. Hummelen, *Appl. Phys. Lett.* **78**, 841 (2001).
- [25] J. Takada, H. Awaji, M. Koshioka, A. Nakajima, and W. A. Nevin, *Appl. Phys. Lett.* **61**, 2184 (1992).
- [26] B. Kannan, K. Castelino, and A. Majumdar, *Nano Lett.* **3**, 1729 (2003).
- [27] J. Nelson, *Curr. Opin. Solid State Mater. Sci.* **6**, 87 (2002).
- [28] R. Schoeder, and B. Ullrich, *Appl. Phys. Lett.* **81**, 556 (2002).

- [29] D. B. Mitzi, Chem. Mater. **13**, 3283 (2001).
- [30] P. B. R. Vincent, K. N. Robertson, T. S. Cameron, and O. Knop, Can. J. Chem. **65**, 1042 (1987).
- [31] S. Wang, D. B. Mitzi, C. A. Feild, and A. Guloy, J. Am. Chem. Soc. **117**, 5297 (1995).
- [32] F. S. Galasso, *Structure, Properties and Preparation of Perovskite-Type Compounds* (Pergamon, New York, 1969).
- [33] see for example (a) K. Yamada, T. Matsui, T. Tsuritani, T. Okuda, and S. Ichiba, Z. Naturforsch. **45a**, 307 (1990).(b) K. Yamada, H. Kawaguchi, T. Matsui, T. Okuda, and S. Ichiba, Bull. Chem. Soc. Jpn. **63**, 2531 (1990).
- [34] M. J. Tricker, and J. D. Donaldson, Inorg. Chim. Acta **31**, L445 (1978), and references therein.
- [35] K. Yamada, Y. Kuranaga, K. Ueda, S. Goto, T. Okuda, and Y. Furukawa, Bull. Chem. Soc. Jpn. **71**, 127 (1998).
- [36] N.W. Ashcroft and N.D. Mermin, *Solid State Physics*, Saunders Coll. Pub. (1976).
- [37] W. Kohn and L. Sham, Phys Rev. **140**, A1133 (1965).
- [38] P. Hohenberg and W. Kohn, Phys. Rev. **136**, B864 (1964).
- [39] J.P. Perdew, K. Burke, and M. Ernzerhof, Phys. Rev. Lett. **77**, 3865 (1996).
- [40] J. P. Perdew, *Electronic Structure of Solids 91*, edited by P. Ziesche and H. Eschrig (Akademie Verlag, Berlin, 1991), p. 11.
- [41] W. E. Pickett, Comput. Phys. Rep., **9** 115(1989)
- [42] D. Vanderbilt. Phys. Rev. B **41**, 7892 (1990)
- [43] S. T. Epstein, A. C. Hurley, R. E. Wyatt, and R. G. Parr, J. Chem. Phys. **47**, 1275 (1967).

- [44] R. P. Feynman, Phys. Rev. **56**, 340 (1939).
- [45] B. G. Pfrommer , B. Cot , S. G. Louie, and M. L. Cohen, J. Comput. Phys. **131** 233 (1997)
- [46] E. A. Wood, J. Appl. Phys. **35**, 1306 (1964)
- [47] N.D. Lang and W. Kohn, Phys. Rev. B **1**, 4555 (1970).
- [48] N.D. Lang and W. Kohn, Phys. Rev. B **3**, 1215 (1971).
- [49] H. Lüth, *Surfaces and Interfaces of Solid Materials* (Springer, Berlin, 1995).
- [50] F.J. Allen, G.W. Gobeli, Phys. Rev. **127**, 150 (1962).
- [51] J. Yoshinobu, H. Tsuda, M. Onchi, M. Nishijima, J. Chem. Phys. **87**, 7332 (1987).
- [52] M. Nishijima, J. Yoshinobu, H. Tsuda, M. Onchi, Surf. Sci. **192**, 383 (1987).
- [53] P.A. Taylor, R.M. Wallace, C.C. Cheng, W.H. Weinberg, M.J. Dresser, et al, J. Am. Chem. Soc. **114**, 6754 (1992).
- [54] C. Huang, W. Widdra, X.S. Wang, W.H. Weinberg, J. Vac. Sci. Technol. A **11**, 2250 (1993).
- [55] A.J. Mayne, A.R. Avery, J. Knall, T.S. Jones, G.A.D. Briggs, W.H. Weinberg, Surf. Sci. **284**, 247 (1993).
- [56] W. Pan, T. Zhu, W. Yang, J. Chem. Phys. **107**, 3981 (1997).
- [57] H. Ness, A.J. Fisher, G.A.D. Briggs, Surf. Sci. **380**, L479 (1997).
- [58] H. Ness, A.J. Fisher, Phys. Rev. B **55**, 1 (1997).
- [59] P. Palermo, M. Palma, P. Samorì, Adv. Mater. **18**, 145 (2006).
- [60] L. Kelvin, Philos. Mag. **46**, 82 (1898).
- [61] W. A. Zisman, Rev. Sci. Instrum. **3**, 367 (1932).

- [62] M. Nonnenmacher, M. P. O'Boyle, H. K. Wickramasinghe, *Appl. Phys. Lett.* **58**, 2921 (1991).
- [63] L. Kronik, Y. Shapira, *Surf. Sci. Rep.* **37**, 1 (1999).
- [64] D. K. Schroder, *Meas. Sci. Technol.* **12**, R16 (2001).
- [65] M. Pfeiffer, K. Leo, N. Karl, *J. Appl. Phys.* **80**, 6880 (1996).
- [66] L. Bürgi, H. Sirringhaus, R. H. Friend, *Appl. Phys. Lett.* **80**, 2913 (2002).
- [67] H. Arend, W. Huber, F. H. Mischgofsky, and G. K. Richter-van Leeuwen, *J. Cryst. Growth* **43**, 213 (1978).
- [68] C. Kittel, *Introduction to Solid State Physics 5th Edition* John Wiley & Sons, (1976).
- [69] F. Chiarella, P. Ferro, F. Licci, M. Barra, M. Biasiucci, A. Cassinese, and R. Vaglio, *Appl. Phys. A*, **86** 89 (2007).
- [70] F. Chiarella, I. Borriello et al submitted to *Phys. Rev. B*.
- [71] I. Watanbe, and T. Okumura, *Jpn. J. Appl. Phys.*, **25**, 1851 (1986).
- [72] J.I. Pankove, *Optical Processes in Semiconductors*, Prentice-Hall, Englewood, New Jersey, (1971).
- [73] D. Alexson, H. Chen, M. Cho, M. Dutta, Y. Li, P. Shi, A. Raichura, D. Ramadurai, S. Parikh, M.A. Stroschio, and M. Vasudev, *J. Phys: Condens. Matter* **17**, R637 (2005) and references therein.
- [74] H. Fukagawa, S. Kera, T. Kataoka, S. Hosoumi, Y. Watanabe, K. Kudo, N. Ueno, *Adv. Mater.* **19**, 665 (2007).
- [75] G. Witte, S. Lukas, P.S. Bagus, and C. Wöll, *Appl. Phys. Lett.* **87**, 263502 (2005).
- [76] V. De Renzi, R. Rousseau, D. Marchetto, R. Biagi, S. Scandolo, and U. del Pennino, *Phys. Rev. Lett.* **95**, 046804 (2005).

- [77] B. Duke, Chem, Rev. **96**, 1237 (1996).
- [78] S. Baroni, A. Dal Corso, S. de Gironcoli, P. Giannozzi, C. Cavazzoni, G. Ballabio, S. Scandolo, G. Chiarotti, P. Focher, A. Pasquarello, K. Laasonen, A. Trave, R. Car, N. Marzari, A. Kokalj, <http://www.quantum-espresso.org>.
- [79] A.M. Rappe, K.M. Rabe, E. Kaxiras, and J.D. Joannopoulos, Phys. Rev. B **41**, R1227 (1990).
- [80] Landolt-Börnstein, *Numerical Data and Functional Relationships in Science and Technology*, Vol. III/17a (Springer-Verlag, Berlin, 1982).
- [81] H. J. Monckhorst and J. D. Pack, Phys. Rev. B **13**, 5188 (1976).
- [82] E. Kaxiras, Y. Bar-Yam, J. D. Jannopoulos and K. C. Pandey, Phys. Rev. B **33**, 4406 (1986).
- [83] A. Many, Y. Goldstein, and N.B. Grover, *Semiconductor surfaces* (North-Holland, Amsterdam, 1965).
- [84] S. J. Sque, R. Jones, and P. R. Briddon, Phys. Rev. B **73**, 85313 (2006).
- [85] D. Cahen, A. Kahn, Adv. Mater. **15**, 271 (2003).
- [86] C. Sgiarovello, N. Binggeli, and A. Baldereschi, Phys. Rev. B **64**, 195305 (2001).
- [87] M. J. Rutter, and J. Robertson, Phys. Rev. B **57**, 9241 (1998).
- [88] T.C. Leung, C.L. Kao, W.S. Su, Y.J. Feng, and C.T. Chan, Phys. Rev. B **68**, 195408 (2003).
- [89] A. Ramstad, G. Brocks, and P.J. Kelly, Phys. Rev. B **51**, 14504 (1995).
- [90] M.P. Casaletto, R. Zanoni, M. Carbone, M.N. Piancastelli, L. Aballe, K. Weiss, and K. Horn, Phys. Rev. B **62**, 17128 (2000).
- [91] J. Bardeen, Phys. Rev. **71**, 717 (1947).

- [92] G. Onida, L. Reining, and A. Rubio, *Rev. Mod. Phys.* **74**, 601 (2002)
- [93] J. Günster, Th. Mayer, V. Kempster, *Surf. Sci.* **359**, 155 (1996).
- [94] Q. B. Lu, R. Souda, D. J. O'Connor, B. V. King, *Phys. Rev. B* **54**, R17347 (1996).
- [95] S. Kono, Y. Enta, T. Abukawa, T. Kinoshita, *Appl. Surf. Sci.* **41-42**, 75 (1989).
- [96] F. G. Allen, *J. Phys. Chem. Solids* **8**, 119 (1959).
- [97] A.J. Fisher, P.E. Blöchl, and G.A.D. Briggs, *Surf. Sci.* **374**, 298 (1997).
- [98] Editor-in-chief David R. Lide *Handbook of Chemistry and Physics 73rd Edition* (CRC press, 1992)
- [99] F. Matsui, H. W. Yeom, I. Matsuda, T. Ohta, *Phys. Rev. B* **62**, 5036 (2000).
- [100] T. Livneh, M. Asscher, *J. Phys. Chem. B* **104**, 3355 (2000).
- [101] M. M. Hills, J. E. Parmeter, C. B. Mullins, W. H. Weinberg, *J. Am. Chem. Soc.* **108**, 3554 (1986).
- [102] G. Cantele, F. Trani, D. Ninno, M. Cossi, and V Barone, *J. Phys.: Condens. Matter* **18** 2349 (2006).
- [103] W. Widdra, A. Fink, S. Gokhale, P. Trischberger, D. Menzel, U. Birkenheuer, U. Gutdeutsch, and N. Rösch, *Phys. Rev. Lett.* **80**, 4269 (1998).
- [104] M. Preuss, W.G. Schmidt, and F. Bechstedt, *Phys. Rev. Lett.* **94**, 236102 (2005).
- [105] A. Vilan, and D. Cahen, *TRENDS in Biotech.* **20**, 22 (2002).
- [106] J. Krüger, U. Bach, and M. Grätzel, *Adv. Mater.* **12**, 447 (2000).
- [107] S. Bastide, R. Butruille, D. Cahen, A. Dutta, J. Libman, A. Shanzer, L. Sun, and A. Vilan, *J. Phys. Chem. B* **101**, 2678 (1997).
- [108] A. Poglitsch, and D. Weber, *J. Chem. Phys.* **87**, 6373 (1987).

- [109] K. Yamada, S. Nose, T. Umehara, T. Okuda, and S. Ichiba, *Bull. Chem. Soc. Jpn.* **61**, 4265 (1988).
- [110] Y. Furukawa, and D. Nakamura, *Z. Naturforsch.* **44a**,1122 (1989).
- [111] O. Knop, R. E. Wasylshen, M. A. White, T. S. Cameron, and M. J. M. Van Oort, *Can. J. Chem.* **68**, 412 (1990).
- [112] N. Onoda-Yamamuro, T. Matsuo, and H. Suga, *J. Phys. Chem. Solids* **51**, 1383 (1990).
- [113] Q. Xu, T. Eguchi, H. Nakayama, N. Nakamura, and M. Kishita, *Z. Naturforsch.* **46a**, 240 (1991).
- [114] N. Onoda-Yamamuro, T. Matsuo, and H. Suga, *J. Chem. thermodynamics* **23**, 987 (1991).
- [115] N. Onoda-Yamamuro, O. Yamamuro, T. Matsuo, and H. Suga, *J. Phys. Chem. Solids* **53**, 277 (1992).
- [116] Q. Xu, T. Eguchi, and H. Nakayama, *Bull. Chem. Soc. Jpn.* **65**, 2264 (1992).
- [117] K. Yamada, K. Isobe, T. Okuda, and Y. Furukawa, *Z. Naturforsch* **49a**, 258 (1994).
- [118] N. Onoda-Yamamuro, O. Yamamuro, T. Matsuo, H. Suga, K. Oikawa, N. Tsuchiya, T. Kamiyama, and H. Asano, *Physica B* **213**, 411 (1995).
- [119] D. B. Mitzi, C. A. Feild, Z. Schlesinger, and R. B. Laibowitz, *J. Solid State Chem.* **114**, 159 (1995).
- [120] T. Okuda, S. Gotou, T. Takahashi, H. Terao, and K. Yamada, *Z. Naturforsch.* **51a**, 686 (1996).
- [121] I. B. Koutselas, L. Ducasse, and G. C. Papavassiliou, *J. Phys.: Condens. Matter* **8**, 1217 (1996).
- [122] A. Maalej, Y. Abid, A. Kallel, A. Daoud, A. Lautie, and F. Romain, *Solid State Commun.* **103**, 279 (1997).

- [123] H. Ishida, H. Maeda, A. Hirano, Y. Kubozono, and Y. Furukawa, *Phys. Stat. Sol. A* **159**, 277 (1997).
- [124] D. B. Mitzi, and K. Liang, *J. Sol. Stat. Chem.* **134**, 376 (1997).
- [125] A. Maalej, Y. Abid, A. kallei, A. Daoud, and A. Lutie, *Ann. Chim. Sci. Mat.* **23**, 241 (1998).
- [126] H. Yano, Y. Furukawa, Y. Kuranaga, K. Yamada, and T. Okuda, *J. Mol. Struct.* **520**, 173 (2000).
- [127] D. B. Mitzi, D. R. Medeiros, and P. R. L. Malenfant, *Inorg. Chem.* **41**, 2134 (2002).
- [128] k. Yamada, K. Mikawa, T. Okuda, and K. S. Knight, *J. Chem. Soc., Dalton Trans.*, 2112 (2002).
- [129] Y. Lee, D. B. Mitzi, P. W. Barnes, and T. Vogt, *Phys. Rev. B* **68**, 020103(R) (2003).
- [130] I. P. Swainson, R. P. Hammond, C. Soulliere, O. Knop, and W. Massa, *J. Sol. Stat. Chem.* **176**, 97 (2003).
- [131] K. Tanaka, T. Takahashi, T. Ban, T. Kondo, K. Uchida, and N. Miura, *Solid State Commun.* **127**, 619 (2003).
- [132] J. L. knutson, J. D. Martin, and D. M. Mitzi, *Inorg. Chem.* **44**, 4699 (2005).
- [133] M. C. Aragoni, M. Arca, C. Caltagirone, F. A. Devillanova, F. Demartin, A. Garau, F. Isaia and V. Lippolis, *CrystEngComm* **7**, 544 (2005).
- [134] I. P. Swainson, M. G. Tucker, D. J. Wilson, B. Winkler, and V. Milman, *Chem. Mater.* **19**, 2401 (2007).
- [135] S. Sourisseau, N. Louvain, W. Bi, N. Mercier, D. Rondeau, F. Boucher, J. Buzare, and C. Legein, *Chem. Mater.* **19**, 600 (2007).
- [136] N. Louvain, W. Bi, N. Mercier, J. Buzare, C. Legein, and G. Corbel, *Dalton Trans.*, 965 (2007).

- [137] N. Troullier and J.L. Martins, Phys. Rev. B **43**, 1993 (1991).
- [138] X. Gonze et al, Zeit. Kristallogr. 220, 558-562 (2005); <http://www.abinit.org>
- [139] A. M. Glazer, Acta Cryst. B **28**, 3384 (1972) and references therein.
- [140] K. Yamada, S. Fuanbiki, H. Horimoto, T. Matsui, T. Okuda, and S. Ichiba, Chem. Lett. **20**, 801 (1991).
- [141] F. R. Poulsen, and S. E. Rasmussen, Acta. Chem. Scand. **24** , 150 (1970).
- [142] See for example A. M. Glazer, Acta Cryst. A **31**, 756 (1975).
- [143] F. Chiarella, P. Ferro, F. Licci, M. Barra, M. Biasiucci, A. Cassinese, and R. Vaglio, Appl. Phys. A **86**, 89 (2007).